Master's thesis

NTNU
Norwegian University of Science and Technology
Faculty of Natural Sciences
Department of Materials Science and Engineering

Mikhail Kuvshinov

Synthesis and characterization of NiMo for efficient hydrogen production from water electrolysis

Master's thesis in Materials Science and Engineering
Supervisor: Ingrid Hallsteinsen
Co-supervisor: Athanasios Chatzitakis
June 2022

NTNU
Norwegian University of Science and Technology

Mikhail Kuvshinov

Synthesis and characterization of NiMo for efficient hydrogen production from water electrolysis

Master's thesis in Materials Science and Engineering
Supervisor: Ingrid Hallsteinsen
Co-supervisor: Athanasios Chatzitakis
June 2022

Norwegian University of Science and Technology
Faculty of Natural Sciences
Department of Materials Science and Engineering

NTNU
Norwegian University of
Science and Technology

Preface

This thesis is written as partial fulfilment of the requirements for "TMT4900 – Materials Technology, Master's Thesis" project at the Norwegian university of Science and Technology. The experimental work has been conducted between January – June 2022 at the Group for Electrochemistry, a part of the Centre for Materials Science and Nanotechnology (SMN), University of Oslo.

First and foremost, I would like to thank my dearest research supervisors, whose support and guidance have been paramount and invaluable for the completion of this work. Dr. Athanasios Chatzitakis, for admitting me into the Group for Electrochemistry and for providing invaluable insight into the world of electrochemistry, modern equipment for conducting the experiments and allowing me being a part of the dedicated team and a positive atmosphere of scientific research. I would like to express to you my gratefulness for providing me with the modern equipment and allowing me being a part of the dedicated team and a positive atmosphere of scientific research. I would like to express my deepest acknowledgement to Dr. Smagul Karazhanov for his persistent encouragement and support beyond what could reasonably be expected of anyone. I would like to express special gratefulness to Prof. Ingrid Hallsteinsen for her strong academic support, patience, and real kindness. Without our mutual enthusiasm and dedication this project could not be realized. My dearest supervisors, your continuous constructive critique and recommendations have induced my professional and personal development.

I extend my eternal gratitude to my family whose encouragement has brought me where I stand today.

Mikhail Kuvshinov

29.06.2022

Abstract

NiMo alloys are considered as highly active catalysts for the Hydrogen Evolution Reaction (HER) in alkaline electrolytes. In this study, the fundamental activity for the HER of NiMo alloy cathodes with comparable surface areas in alkaline electrolyte are studied in detail. Two methods for substrate preparation – the chemical etching with varying time intervals and the mechanical polishing conducted by different-size grinding papers on Ti-foils – have been employed to compare their effect on the electrocatalytic performance of the material under study (NiMo alloy cathodes) and identify the best type of pre-treatment that results in the formation of the best electrocatalyst.

The electrodeposition of NiMo alloy at -20 mA cm^{-2} and 15 min from the bath solution containing 79 g of $NiSO_4 \cdot 6H_2O$, 88 g of $Na_3C_6H_5O_7 \cdot 2H_2O$, and 44 g of Na_2MoO_4 with the adjusted pH to 10.5 by ammonia solution was applied for the synthesis of the material under the study. The electrocatalytic characterization of the synthesized NiMo alloys was performed in 1 M KOH (pH = 14.7) media by Linear Sweep Voltammetry (LSV) in a potential window of -1.35 to -0.90 V vs Hg/HgO and Electrochemical Impedance Spectroscopy (EIS) at – 1 mA cm^{-2}, – 10 mA cm^{-2}, and – 1 V. The study of morphology, composition, and structure was conducted by Scanning Electron Microscopy (SEM), Energy Dispersive X-Ray Spectroscopy (EDS), and X-Ray Diffraction (XRD).

The best pretreatment method was proved to be the mechanical polishing, and hence the group of NiMo samples with this substrate pretreatment method showed the lowest Tafel slope (80.7 mV dec^{-1}), the highest exchange current density (- 2.45 mA cm^{-2}), Volmer-Heyrovsky mechanism with Volmer step as Rate Determining Step (RDS) for HER, the composition of Ni(63.9 at%), Mo (16.3 at%), and O (19.8 at%), the atomic ratio of Ni:Mo as 3.9:1, fine agglomerated particles that form homogeneous coverage on the Ti substrate, and the lowest deposition potential. All samples demonstrated an intensity peak that corresponds to face-centered cubic NiMo(111) and the rest of the diffraction peaks were completely matched with the diffraction pattern of hexagonal Ti. The most effective HER kinetics was observed in the NiMo deposited on 4 s etched Ti substrate group by EIS characterization at -10 mA cm^{-2}, with R_{ct} of 6.61 Ω. Also, it was observed that the electrocatalytic performance increases with the increase of etching time. All these results pointed out that the substrate treatment can have a significant effect on the overall performance of the NiMo on Ti substrate electrode.

Further work may be done by the application of other pretreatment methods such as ultrasonic cleaning and heat annealing, and by applying more investigation techniques such as X-Ray Photoelectron Spectroscopy (XPS), Chronoamperometry (CA), and to collect more versatile data about electrocatalytic performance of NiMo for HER in alkaline media.

Sammendrag

NiMo-legeringer anses som svært aktive katalysatorer for Hydrogen Evolution Reaction (HER) i alkaliske elektrolytter. I denne studien blir den grunnleggende aktiviteten for HER av NiMo-legeringskatoder med sammenlignbare overflatearealer i alkalisk elektrolytt studert i detalj. To metoder for substratpreparering - den kjemiske etsingen med varierende tidsintervaller og den mekaniske poleringen utført av slipepapir i forskjellige størrelser på Ti-folier - har blitt brukt for å sammenligne deres effekt på den elektrokatalytiske ytelsen til materialet som studeres (NiMo-legeringskatoder) og identifisere den beste typen forbehandling som resulterer i dannelsen av den beste elektrokatalysatoren.

Elektrodeponering av NiMo-legering ved -20 mA cm-2 og 15 minutter fra badløsningen inneholdende 79 g NiSO4 · 6H2O, 88 g Na3C6H5O7· 2H2O, og 44 g Na2MoO4 med den justerte pH til 10,5 med ammoniakkløsning ble påført for syntese av materialet under studien. Den elektrokatalytiske karakteriseringen av de syntetiserte NiMo-legeringene ble utført i 1 M KOH (pH = 14,7) media ved Linear Sweep Voltammetry (LSV) i et potensielt vindu på -1,35 til -0,90 V vs Hg/HgO og elektrokjemisk impedansspektroskopi (EIS) kl. – 1 mA cm-2, – 10 mA cm-2 og – 1 V. Studiet av morfologi, sammensetning og struktur ble utført ved hjelp av skanningselektronmikroskopi (SEM), Energy Dispersive X-Ray Spectroscopy (EDS) og X -Strålediffraksjon (XRD).

Den beste forbehandlingsmetoden viste seg å være den mekaniske poleringen, og derfor viste gruppen av NiMo-prøver med denne substratforbehandlingsmetoden den laveste Tafel-hellingen (80,7 mV des-1), den høyeste utvekslingsstrømtettheten (- 2,45 mA cm-2), Volmer-Heyrovsky-mekanisme med Volmer-trinn som ratebestemmende trinn (RDS) for HER, sammensetningen av Ni(63,9 at%), Mo (16,3 at%) og O (19,8 at%), atomforholdet Ni:Mo som 3,9:1, fine agglomererte partikler som danner homogen dekning på Ti-substratet, og den laveste avsetningen sjonspotensial. Alle prøvene viste en intensitetstopp som tilsvarer ansiktssentrert kubisk NiMo(111) og resten av diffraksjonstoppene ble fullstendig matchet med diffraksjonsmønsteret til sekskantet Ti. Den mest effektive HER-kinetikken ble observert i NiMo avsatt på 4 s etset Ti-substratgruppe ved EIS-karakterisering ved -10 mA cm-2, med Rct på 6,61 Ω. Det ble også observert at den elektrokatalytiske ytelsen øker med økningen av etsetiden. Alle disse resultatene påpekte at substratbehandling kan ha en betydelig effekt på den generelle ytelsen til NiMo på Ti-substratelektroden.

Ytterligere arbeid kan gjøres ved å bruke andre forbehandlingsmetoder som ultralydrensing og varmegløding, og ved å bruke flere undersøkelsesteknikker som røntgenfotoelektronspektroskopi (XPS), kronoamperometri (CA), og for å samle inn mer allsidige data om elektrokatalytisk ytelsen til NiMo for HER i alkaliske medier.

Table of content

List of Abbreviations

CA	Chronoamperometry
CE	Counter electrode
CP	Chronopotentiometry
CV	Cyclic voltammetry
EDS	Energy Dispersive X-Ray Spectroscopy
EIS	Electrochemical Impedance Spectroscopy
HER	Hydrogen evolution reaction
LSV	Linear sweep voltammetry
OER	Oxygen evolution reaction
PEC cell	Photoelectrochemical cell
RDS	Rate-determining strp
RE	Reference electrode
RHE	Reversible hydrogen electrode
SEM	Scanning electron microscopy
SHE	Standard hydrogen electrode
STH	Solar-to-hydrogen
XRD	X-ray diffraction

1. Introduction

1.1. Global energy and environmental problems

Since the beginning of XIX century when industrial revolutions began around the world, different nations, especially the industrialized countries, have been more and more relying on fossil fuels as the key energy source. This resulted in heavy dependency on fossil resources that have become one of the major contemporary problems worldwide. The world is facing a major energy shortage in centuries as the global energy consumption on the planet is predicted to grow exponentially and is likely to double within the next decades (50 years) amid depletion of fossil fuels.

In the last few decades, in the pursuit of inexpensive and clean renewable energy sources researchers extensively explored wind, solar and geothermal power as alternative resources for traditional fossils. Nowadays, hydro energy is accounted for 47% of the renewable power production and is currently the largest renewable energy source[1]. Wind energy is lagging behind with 23%, and solar energy share in the total renewable energy production is rather small. However, solar energy is the fastest growing sector in production capacity that increased to 2019 (650.5 GW) from 2010 (43.6 GW), i.e., in almost 15 times. However, the lack of sustainable and reliable renewable energy sources and approaching energy and environmental crisis have led to numerous attempts in developing innovative solutions to the global energy problem. Excess electricity conversion into chemical fuels could solve this problem.

1.2. Hydrogen economy

Hydrogen gas is pursued as a promising alternative fuel that could possibly solve the global energy security problem in the future. The hydrogen economy is defined as the economy that relies on hydrogen as commercial fuel that would deliver a substantial fraction of a nation's energy and services[1]. Hydrogen is vigorously considered as the fuel of the future when produced utilizing renewable energy sources and among the key solutions to the decarbonization strategy.

Hydrogen is a sustainable future green energy carrier due to its high gravimetric energy density and environmental friendliness. Today, numerous hydrogen production methods have been researched, developed, and used. However, the major share (over 90%) of the industrial hydrogen production is obtained from fossil resources and is largely dominated by natural gas steam reformation and coal gasification methods.

Their popularity is justified by low production costs in the range of $0.50 – $1.70 per kg of H2, depending on regional gas prices[2]. But these processes are not environmentally friendly and resource sustainable, especially in the long-term perspectives, as low-purity hydrogen is generated and lots of energy is consumed with massive greenhouse gases emissions causing global warming. The exacerbating environmental problems have led to the demand in decarbonizing hydrogen production methods that can reduce the carbon footprint in the final products as well as produce the hydrogen by means of the renewable energy sources.

Alternative energy production technologies have been developed in an attempt to alleviate the environmental and energy challenges. There are four promising methods for the hydrogen production: **thermochemical** (steam- and pyro-reforming of organic compounds of renewable origin), **biological** (by metabolic processes), **photolytic** (photoelectrochemical and photobiological systems) [2,3], and **electrolytic** (by wind and by solar energy as primary electricity source, including high-temperature regime). The latter will be thoroughly discussed and applied in this thesis as sustainable hydrogen production from electrochemical water splitting has attracted growing attention as a true renewable and fully environmentally friendly approach for large-scale hydrogen production, without co-production of the green-house gas, CO2. Among major advantages of hydrogen produced by water electrolysis is no pollution, high purity (>99%), and simple operation. The wind energy and the solar energy that are used to produce electricity for the electrolysed hydrogen production cost $4.50/kg H2 and $3.0/kg H2 respectively [2]. It is explained by the higher production costs of water electrocatalysis processes compared to the conventional fossils because of high electricity costs and interfering laws.

Hydrogen production through water electrolysis has attracted considerable scientific interest because of its potential for providing energy without the emission of carbon dioxide and its relevance to renewable energy storage.[1] Among various approaches of the hydrogen production, the electrocatalytic water electrolysis is the most facile and economical one. It is expected to play a dominant role in the future renewable energy-based economy[1,2]. To accelerate the sluggish HER kinetics the development of highly active, cost-effective, and durable bifunctional–water splitting electrocatalyst is essential to reduce the kinetic HER overpotential[4,5] and it is of significant importance for clean energy applications.

Although, production of hydrogen by water electrolysis is not currently cost-competitive to natural gas reforming, the share of hydrogen produced using renewable power sources has to be substantially increased to become independent of fossil energy carriers. It is expected that the share of renewables in total electricity generation will increase to 61% in 2050 [6]. This prediction makes the solar energy very attractive for further study and

for application to electrocatalytic water splitting that, in turn, opens a door for an intensive study of photoelectrochemical (PEC) cells.

1.3. NiMo alloy cathodes

There is a strong demand for the development of abundant and inexpensive advanced materials to reduce the cost of hydrogen production technologies [7]. Therefore, searching for low-cost catalysts becomes an essential way to develop hydrogen economy. Currently, the most effective HER electrocatalysts for hydrogen production are conventional noble metal-based catalysts, mainly those of the platinum group [8-10] and platinum-based alloys such as Pt/C [11], Pt/NC [12], and PtO_x/TiO_2[13]. The noble metal platinum (Pt) and its composites play the major role in the contemporary hydrogen production technologies[14-16]. Platinum group metals are known as the best pure metal catalysts[8-10]. They are the most active and the most efficient catalysts for hydrogen evolution reaction because of their low overpotential and fast kinetics for driving HER [8-10]. Platinum itself is the benchmark HER electrocatalyst which generates large cathodic current density with almost zero HER overpotential[14-16].

Despite their outstanding performance, the scarcity and limited world-wide supply accompanied by prohibitively high costs of platinum, seriously obstruct its application in electrocatalytic HERs making Pt unattractive for viable commercial processes of global-scale industrial hydrogen production[17]. Therefore, to reduce the cost of hydrogen production technologies [7] the strong demand for the development of low-cost alternative HER catalysts with superior stability based on earth-abundant and non-precious elements[18-20] becomes of critical importance. Transition-metal (TM)-based electrocatalysts appear to be the promising alternatives owing to their natural abundance and great availability. Thanks to their great availability, low cost and natural abundance transition metal (TM)-based catalysts appear to be a promising alternative. In the past decades, various material classes have been widely investigated to understand and improve the catalytic activities of transition metals such as pure metals, metal alloys[21], borides, carbides[22], chalcogenides[23], complexes[24], hydroxides, layered double hydroxides, nitrides, oxides, phosphides, selenides, sulfides, and tellurides[25-27].

The series of promising non-noble metal-based catalysts presented by NiCo [28], amorphous MoS2 from electro-polymerization, nanoporous Mo2C nanowires, NiMoNx/C, FeP nanowire arrays, and can be considered as confident attempts in the quest for new reliable electrocatalytic materials and. However, all of them still fail to surpass platinum-based catalysts in overall performance. There are many challenges that should be overcome for complete substitution of platinum and other noble metals by new advanced

materials. And the most complex one is a synthesis of catalysts that can outperform noble metal catalysts in all aspects.

The key parameters that play an important role in the selection of an active catalytic material for efficient HER are its strong intrinsic activity, good electrical conductivity, large surface area, low overvoltage, good electrochemical stability of performance, low cost, and ease of use[29]. Despite the fact that these requirements are hard to meet simultaneously, many electrocatalytic materials for cathodes have been advanced and investigated to respond to this request [30-32].

In alkaline media, Ni is reported to be the best noble-free pristine metal catalyst for the HER. Inspired by the abundant nature of elemental Ni, numerous efforts have been devoted to the design and improvement of the intrinsic activity of various Ni-based electrocatalysts [33] For example, one versatile strategy is compositional tailoring by alloying other elements of iron group metal (Mo, P [34,35], Co, S [36,37], Fe) into the Ni backbone [39-42]. Compared to pure Ni, the binary electrocatalysts made by co-deposition or alloying attract growing attention as a reliable approach to attain superior and more durable electrocatalytic activity for the HER.

According to the research literature, among these materials, NiMo alloys are one of the best non-precious bimetallic metal electrocatalysts for hydrogen production in alkaline media, which can be a promising alternative to platinum for the hydrogen evolution reaction[43-45,28]. The reasons for this are believed to be high electrocatalytic activity, long-term stability as HER catalysts under alkaline conditions[46], high surface area and porosity[38]. At the same time, the reasons why the electrocatalytic activity of NiMo ranges from standard values of pure Ni electrode to values that are several order of magnitude higher are not understood yet[47]. In addition, the mechanism and active species of HER that take place on NiMo surface also continue to be under discussion[48]. The possible solution that may give answers to these issues is identification of the optimal synthesis conditions that result in the best performance of electrocatalyst. In case of the synthesis of electrocatalysts, the electrodeposition is preferable choice due to low cost and "easy-to-perform" character. There are many noticeable works that address to electrodeposition of NiMo alloys as electrocatlysts [49-50], but none of them focused systematically on the optimization of electrodeposition parameters in terms of variation of deposition times and deposition currents. This gives a good soil for systematic investigation of synthesis conditions and subsequent characterization of NiMo alloy for electrocatalysed water electrolysis purposes.

1.4. Aim of the thesis

The aim of this thesis is to improve the electrocatalytic activity of NiMo alloy electrodeposited on Ti foil substrates for HER in alkaline media. By applying two different pretreatment methods, i.e., mechanical polishing and chemical etching, to the Ti substrates, the key objective is to find out which of the two methods, if any, results in a greater improvement of the electrocatalytic activity.

The main objective for the thesis is to investigate the effect of the substrate treatment on the deposition and electrocatalytic activity of NiMo for HER, by means of morphological, compositional, structural, and electrochemical characterizations.

2. Theory

2.1. Electrolytic cell – core concepts

An electrolytic cell converts electrical energy into a chemical. A typical electrolytic cell consist of four main parts: two electrodes, connecting wires, voltage source, and electrolyte. Generally, a good electrolyte should meet the following criteria: it has to be a good ionic conductor and electronic insulator, thermally stable and inert to other cell components. It should have a wide electrochemical window and be based on sustainable chemistries [7]. The electrolyte contains species that are used for the electrolysis process. The wires are connected to the electrodes to complete to circuit. Hence, current can flow between the electrodes. The voltage source drives electrical energy into the cell, thus enabling the water splitting. The two electrodes act as electrical conductors that are brought in contact with the electrolyte that is liquid, or solid.

An electrolytic cell has two separate half-cells: a reduction half-cell and an oxidation half-cell and utilizes redox reactions. An external source of electricity is used in an electrolytic cell to drive electron flow from an anode to a cathode. Cathode is a negative electrode where reduction reactions occur. In other words, positive ions, i.e., cations, migrate to the cathode to be reduced to a specie with lower oxidation state. The half-reaction at the cathode is described by Equation (1), assuming aqueous electrolyte, solid product, and standard conditions:

$$R^{n+}(aq) + ne^- \rightarrow R(s) \quad E^o_{(red)} \quad (1)$$

where $R^{n+}(aq)$– positive ion of atom R, ne^- is transferred electrons, $R(s)$ – reduced substance in solid state, and $E^o_{(red)}$ – the standard potential of the reduction half-reaction, measured in volts (V).

At the same time, the oxidation occurs at the anode that is a positive electrode. Negative ions, i.e. anions, migrate to the anode to be oxidized to a specie with higher oxidation state. Assuming aqueous electrolyte, solid product, and the standard conditions of temperature and pressure, the half-reaction at the anode is described by Equation (2):

$$O^{n-}(aq) \rightarrow O(s) + ne^- \quad E^o_{(ox)} \quad (2)$$

where $O^{n-}(aq)$ – negative ion of neutral atom O, $O(s)$ – oxidized substance in solid state, and $E^o_{(ox)}$– the standard potential of oxidation half-reaction, measured in volts (V).

Generally, the standard potentials are given as reduction potentials. Therefore, the standard oxidation potential is the reverse of the standard reduction potential.

To drive electrical energy into the electrolytic cell by converting it into the chemical one the standard cell voltage (E^o) has to be obtained. The standard cell voltage (also called standard equilibrium potential or minimum voltage) is determined by the ratio of the standard Gibbs free energy for reaction to the product of the number of exchanged electrons and the Faraday constant F as shown in Equation (3):

$$\Delta E^o = -\frac{\Delta G^o}{nF} \quad (3)$$

where n – number of moles transferred in the reaction, F – the Faraday constant, 96500 C mol^{-1}.

If standard change in Gibbs free energy, kJ mol^{-1}, gives positive sign for ΔG^o it indicates non-spontaneous process. Therefore, it proves that the operation of the electrolytic cell is the process that requires an input of energy corresponding to the value of E^o, if standard conditions are maintained.

2.2. Polarization in two-and three-electrode systems

In an electrochemical cell, electrodes play a fundamental role in understanding of electrochemical processes. Special attention is paid to the reference electrode (RE) that initially just completes an electrochemical cell. Reference electrode is used to measure electrode potential of a single electrode, since it is not possible to measure separately potential of a single electrode. Therefore, all potentials of the electrodes of interest are given relative to the reference electrodes. Ideally, the incorporated in a system reference electrode should have constant potential irrespective of what kind of electrode (anode or cathode) is used[51].

To measure the electrode potential by a reference electrode, it is necessary to choose an electrode with a set standard value against which all other RE are measured. In electrochemistry, this standard electrode is called the standard hydrogen electrode (SHE). It has value of 0 V for potential. Half-reaction for this electrode is given in Equation (4):

$$2H^+(aq) + 2e^- \rightarrow H_2(g) \quad (4)$$

where electrode consists of a metal, usually platinum that is immersed in aqueous solution containing hydronium ions at activity value, a, that equals to 1, and saturated by hydrogen gas at pressure of 1 bar.

The choice of SHE was done for the thermodynamic reasons, and not for experimental ones. Hence, this electrode is not so practical to use in every experiment and this explains why other reference electrodes should be used instead of SHE. Despite the fact that other

reference electrodes are more frequently used and potential values are reported with respect to these reference electrodes, the final potential values should be given with respect to SHE. This requires conversion of potentials from reversible hydrogen electrode (RHE) to SHE as shown in Equation (5):

$$E_{SHE} = E_{m,RE} + E_{RE} \quad (5)$$

where E_{SHE} – potential measured with respect to SHE, $E_{m,RE}$ – potential measured with respect to the chosen reference electrode, and E_{RE} – potential (standard or not standard) of the reference electrode with respect to SHE.

It should be noted that this conversion is appropriate when electrodes are studied in the same electrolyte. In case of different electrolyte media, variation of reaction potentials versus SHE with solution pH makes comparison in electrode studies complicated, even if SHE conversion is applied. To rectify this inconvenience, all potentials are recommended to convert to RHE scale and report them accordingly. The conversion equation (6) is:

$$E_{RHE} = E_{SHE} + 2.303\frac{RT}{F}pH \quad (6)$$

where E_{RHE} potential measured with respect to RHE, R – universal gas constant, T is absolute temperature, $2.303\frac{RT}{F}$ is numerically equal to 0.0591 V at 25°C.

This conversion is useful in electrocatalytic studies and enables adequate comparison in the electrode studies across electrolytes of different pH. Equation (6) can be expanded for cases where RE was measured against other RE. By substituting Equation (5) into Equation (6) and adding potential of used reference electrode measured against another reference electrode, the resulting Equation (7) is:

$$E_{RHE} = E_{m,RE1} + E_{RE1,RE2} + E_{RE2} + 2.303\frac{RT}{F}pH \quad (7)$$

where RE_1 – the chosen reference electrode, RE_2 – the other reference electrode that was used to measure potential of the chosen reference electrode, $E_{m,RE1}$ – potential measured with respect to the chosen reference electrode, $E_{RE1,RE2}$ – potential of the chosen reference electrode measured with respect to another reference electrode, and E_{RE_2} is potential of the reference electrode with respect to SHE. The conversion between different electrode potentials can also be represented graphically.

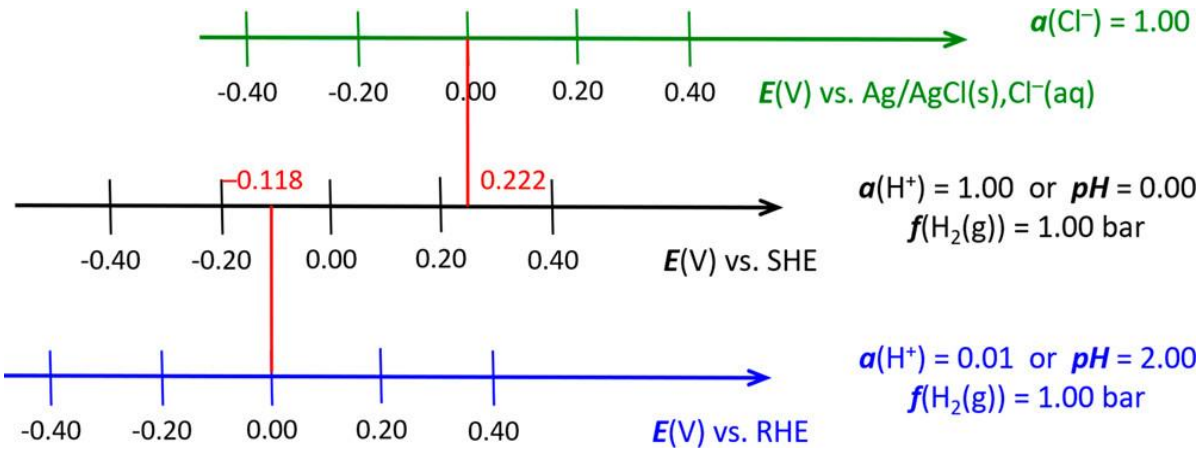

Figure 2.1: Comparison of the potential scales of the SHE, to the RHE (for a(H^+=1.00 and f(H2)=1.00 bar), for the standard silver chloride electrode (a(Cl^-)=1.00), ref.[52]

Figure 2.1 shows comparison of the potential scales of the RHE, the SHE, and the standard silver-silver chloride electrode by graphical approach. This comparison clearly demonstrates how the conversion between the electrode potentials can be easily done graphically just by adjusting the scales in correct manner relative to each other and reading the needed values. [52,53]

When electrodes in different cell arrangements are set, a main consideration for further studies that should be kept in mind, is polarization in electrochemical cell system. In fact, there are three different types of polarizations: kinetic polarization that comes from electrode interface, transport polarization, arising from transport layer that surrounds the electrodes and Ohmic polarization that originates from entire ionic electrolyte. This system suffers actually from five polarizations: kinetic polarization that comes from RE interface and kinetic polarization that comes from working electrode (WE) interface, transport polarization, arising from transport layer that surrounds the RE and transport polarization, arising from transport layer that surrounds the WE, and Ohmic polarization from the ionic electrolyte.

In two-electrode system that schematically presented in **Figure 2.2a**, RE is combined with counter electrode (CE) in one new RE. By this action, the two polarizations associated with RE disappear, since overvoltages that happen at the CE, are not measured by voltmeter and as result, there is no current passing through the RE part. Ohmic polarization can also be significantly reduced by placing WE and combined CE and RE as close as possible to each other. It is important to note that overvoltage is the difference between the actual potential and null potential (potential when value of passing current is zero), and it serves as extent of electrode polarization [51].

The drawback associated with the combination of RE and CE is that voltage source can no longer guarantee that potential at WE is constant. Therefore, additional technology is required to compensate this drawback. A potentiostat is utilized to adjust current that flows through CE to a value that makes $E_{WE} - E_{RE}$ equals to an experimentally set value of voltage. At the present moment the potentiostat incorporates both a voltmeter and an amperometer as well as the instrument for numerical and graphical processing of input and output data in tandem with modern software for additional data processing.

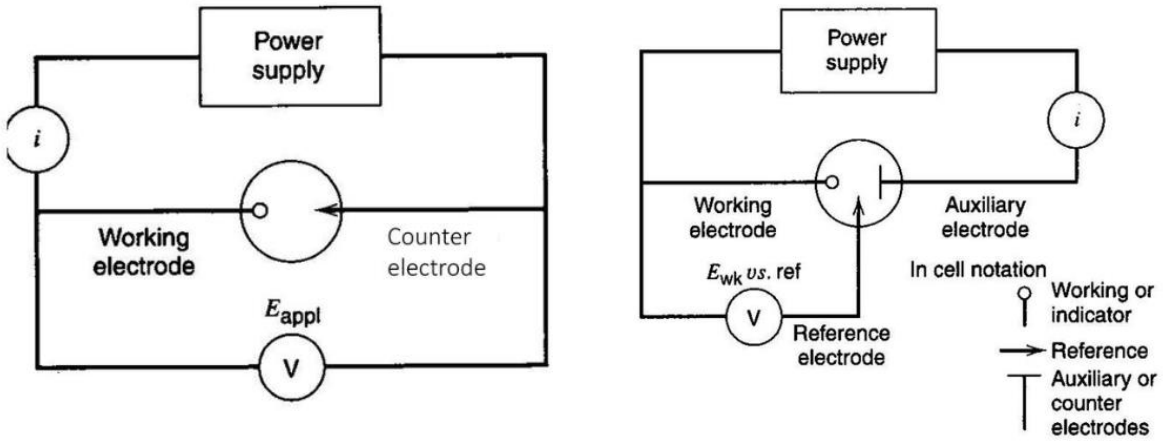

(a) (b)

Figure 2.2: a) Two-electrode cell, b) Three-electrode cell and notation for the different electrodes, ref.[54]

As beneficial consequence, the application of the potentiostat enables to use three-electrode cell. The schematic of the three-electrode system can be seen on **Figure 2.2b)** [51,54]. Thus, the transition from two- to three-electrode system leads to relief in demands that is placed on RE, and with placement of the reference electrode as close as possible to working electrode, Ohmic polarization are greatly reduced. Despite, such useful transition, there are some experiments where application of two-electrode cell is still necessary. Also the electrodes continue to be affected by kinetic and transport polarizations in three-electrode cell, but the reduced Ohmic polarization may significantly compensate these losses in some cases[51,54].

2.3. Thermodynamics

Alkaline water electrolysis is a process of splitting water by electrical energy in alkaline electrolyte. A typical water electrolysis system is given on **Figure 2.3**.

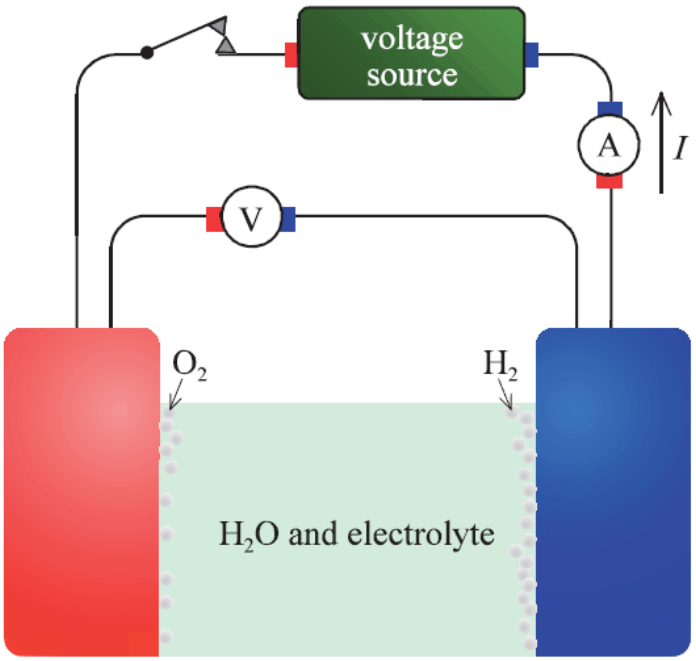

Figure 2.3: The electrolysis of water produces oxygen at the anode and hydrogen at the cathode, ref.[51]

Alkaline water electrolysis is applied to split water into hydrogen and oxygen gases applying direct electric current to water. The operating principle of the overall reaction of the electrolytic water splitting is illustrated by Equation (8). The chemical reaction shows a water molecule that reacts to hydrogen and oxygen in the ratio of 2:1.

$$2H_2O(l) \rightarrow 2H_2(g) + O_2(g) \quad (8)$$

Electrochemical water splitting is presented by two half-reactions: the water oxidation half-reaction that takes place at the anode (oxygen evolution reaction, OER) and water reduction half-reaction that occurs at the cathode (hydrogen evolution reaction, HER) in 1 M alkaline electrolyte.

The half-reaction at the anode is shown in Equation (9):

$$4OH^-(aq) \rightarrow 2H_2O(l) + O_2(g) + 4e^- \quad (9)$$

At the anode, hydroxide ions are oxidized to water molecules and oxygen gas while releasing electrons.

Equation (10) defines the half-reaction at the cathode:

$$4H_2O(l) + 4e^- \rightarrow 4OH^-(aq) + 2H_2(g) \quad (10)$$

Through this reaction, water molecules are decomposed, i.e. reduced by electrons to negatively charged hydroxide ions and hydrogen gas evolves at the cathode.

The thermodynamics determines the required cell voltage for the water electrolysis reaction. Theoretically, the minimum required voltage to split water into oxygen and hydrogen gases is defined as the thermodynamic reversible potential (E_r). It is the equilibrium potential, i.e. the theoretical voltage of electrolysis. The thermodynamic reversible potential (E_r) is determined by the ratio of the free reaction enthalpy (minimum Gibbs energy, ΔG^o) to the product of the number of exchanged electrons and the Faraday's constant F, and is given by the Nernst equation as shown in Equation (11):

$$E = E^O - \frac{RT}{nF} \ln \{ \frac{a_z^{v_z} a_y^{v_y} \dots}{a_A^{v_A} a_B^{v_B} \dots} \} \quad (11)$$

where E_0 is standard equilibrium potential, R is gas constant, T is absolute temperature, n – the number of exchanged electrons involved in the reaction, F – Faraday's constant (96,485 C mol^{-1}).

Thus, at standard conditions of an ambient pressure of 1 bar and a temperature of 25°C or 298 K, the free reaction enthalpy (ΔG^o) for the water splitting reaction is 237 kJ mol^{-1} [51] that drives to the thermodynamic reversible potential of E_r = 1.23V. This is exactly the minimum energy used to drive the electrochemical process.

However, if free reaction enthalpy is positive ($\Delta G°>0$), the reaction of the water electrolysis process is a non-spontaneous one. Thus, the electrolyzer requires an external energy input in addition to the thermodynamic (theoretical) reversible potential to drive the electrochemical reaction of water electrolysis due to the sluggish reaction kinetics of catalysts. The total energy required to promote the splitting of water is defined as the formation enthalpy and is given in Equation (12):

$$\Delta H^o = \Delta G^o + T\Delta S^o \quad (12)$$

where $T\Delta S^o$ is the loss of energy due to heat dissipation. At standard conditions, the formation enthalpy ΔH^o for water electrolysis is 286 kJ mol^{-1}.

In real-life water electrolysis, the actual cell voltage is higher than the thermodynamic reversible potential and the difference is converted into heat. Since the water decomposition reaction by electrolysis is endothermic, the heat thus caused is absorbed by the water electrolysis reaction until total cell voltage exceeds 1.48 V, which is the sum of the reversible voltage (ΔG is about 1.2 V) and heat absorption potential or irreversible thermal losses ($T\Delta S$ is about 0.28 V).

The total cell voltage required for the electrochemical water splitting is calculated according to Equation (13):

$$E_{total} = E_r + E_{ov} + E_{ohm} \quad (13)$$

where E_{total} is the required voltage for water electrolysis reaction, E_r is the thermodynamic reversible potential (theoretical minimum voltage of 1.23 V, which corresponds to a zero reaction rate), E_{ov} is overvoltage (overpotential), and E_{ohm} is ohmic loss.

Reversible potential is theoretically decided according to the reaction condition, but activity of electrodes and cell design affect the overvoltage and ohmic loss. The overpotential is the force to overcome the intrinsic activation barrier present at the anode (η_a) and at the cathode (η_c), as well as the presence of resistances, such as, solution resistance, $\eta_{sol} = jR_{sol}$, and contact resistance, $\eta_{cont} = jR_{cont}$: and is formulated in Equation (14):

$$E_{ov} = \eta + \eta a + |\eta c| \quad (14)$$

where η_a and $|\eta_c|$ denote the anodic and cathodic overpotentials at a certain current density, In water electrolysis, overvoltage is decided by the reaction rate at the electrodes. Therefore, electrodes with highly active electrocatalysts can reduce the overvoltage. Equation (15) describes Ohmic loss:

$$E_{ohm} = iR + jR_{sol} + jR_{cont} \quad (15)$$

where iR is the voltage drop in the electrochemical setup, determined by Ohm's law, $\eta_{sol} = jR_{sol}$ – solution resistance and $\eta_{cont} = jR_{cont}$ – contact resistance.

Ohmic loss is mainly caused by electric resistance of electrolyte, which can be reduced by shortening the distance between anode and cathode. Ohmic loss is also caused by electric resistance in the circuit. Both overvoltage and ohmic loss increase with the increasing current density (current per unit area of electrode), hence increase of cell voltage and, therefore, increase of electric power to make hydrogen.

At the total cell voltage, all the heat generated by irreversible thermal losses, namely ohmic loss and overvoltage, is consumed by the reaction itself and there is no heat generation or absorption to and from the outside of the system. Therefore, the total cell voltage is called thermoneutral voltage where all electric energy utilised for the electrolysis is transformed into heat content of the emitted gas. The thermoneutral potential ($E°_{tn}$), which magnitude is –1.48 V, is defined in Equation (16):

$$E_{tn}^{o} = \frac{\Delta H^{o}}{-nF} \quad (16)$$

On the basis of Faraday's laws, the quantities of the gases of oxygen and hydrogen generated from water splitting are proportional to the total current in the system. Thus, this voltage is used for the standard of 100% efficiency. The thermoneutral potential is very important in designing electrolyzers, since all electricity supplied beyond this point is converted into heat, which must be removed to maintain the temperature of cells.

Therefore, the efficiency and performance of an electrolyzer depend strongly on the electrode materials. No electrolysis is possible at cell voltage under reversible voltage, but it is possible, at least theoretically, to electrolyze water under thermoneutral voltage. High temperature steam electrolysis uses this principle and by supplying part of the energy with heat, it reduces cell voltage. However, as for alkaline water electrolysis, voltages higher than the thermoneutral potential value have to be applied to achieve the electrochemical water splitting as an electrolyzer cannot work below the thermoneutral voltage. At the present moment the water electrolyzers that are utilised in industrial production work at a cell voltage of 1.8–2.2 volts corresponding to 4.3–5.3 kWh per N m^3 hydrogen. The normal condition (N) is achieved at the volume at 0°C and 1atm pressure. As in water electrolysis the current efficiency is nearly 100%, dividing 1.48 by cell voltage provides the energy efficiency of electrolysis[55].

2.4. Hydrogen Evolution Reaction mechanism

Hydrogen evolution reaction (HER) in alkaline water electrolysis is one of the most important electrochemical reactions and should be considered during the study and evaluation of the electrocatalytic performance. The HER is the fundamental half-reaction to generate hydrogen at the cathode that comprises a two-electron transfer process. The generally accepted mechanism of the HER in alkaline media is regarded to be the combination of three primary successive reaction steps: water adsorption, water dissociation, and hydrogen generation named after Volmer, Heyrovsky, Tafel, respectively [56-61].

The Volmer step (Equation 17) is described by the water splitting of a molecule that includes the dissociation into OH^- and the formation of adsorbed hydrogen on free sites of catalyst surface. It is then followed by either Heyrovsky step (Equation 18) of hydrogen production via the electrochemical dissociation process with the breaking of O–H bonds in water molecules and creation of hydrogen atoms (H*) and/or the Tafel step (Equation 19) characterized by the chemical desorption process.

Volmer step:

$$H_2O + M + e^- \leftrightarrow M + H_{ads} + OH^- \quad (17)$$

Heyrovsky step:

$$H_2O + M + e^- + H_{ads} \leftrightarrow M + H_2 + OH^- \quad (18)$$

Tafel step:

$$2\mathrm{M} + 2\mathrm{H}_{\mathrm{ads}} \leftrightarrow 2\mathrm{M} + \mathrm{H}_2 \quad (19)$$

where M represents the active sites on the electrode, H_{ads} denotes a hydrogen atom adsorbed on the electrode (Nørskov et al., 2005; Stamenkovic et al., 2017).

In fact, all the three reactions compete with each other and the slowest reaction will dominate the reaction rate [62]. Several authors have reported that the HER reaction may proceed via two pathways: at low overpotentials it follows Volmer-Tafel mechanism, while at high overpotentials the water splitting reaction proceeds via the Volmer–Heyrovsky pathway as the Tafel step is negligible [63-66]. The two mechanisms are schematically described in **Figure 2.4**.

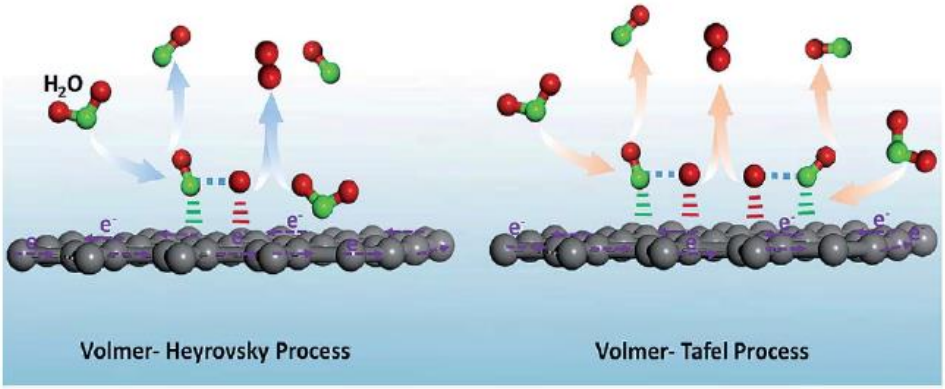

Figure 2.4: Volmer-Heyrovsky and Volmer-Tafel mechanisms for HER in alkaline solution. Adapted from ref.[27]

Generally, to evaluate the ability of an electrocatalyst to initiate the reactions three appropriate computational indicators are employed, namely the activation energy of water adsorption (E_{ads}), the water dissociation energy (E_{ac}), and the free energy of hydrogen adsorption (ΔG_{Hads}). The catalysts' values of E_{ads}, E_{ac}, and ΔG_{Hads} are the sound indicators of their respective properties of water adsorption, water dissociation, and hydrogen generation.

The electrocatalyst's activity rate towards the HER is significantly affected by the strength of the H_{ads}–M bond that can be estimated by the adsorption-free energy of hydrogen (ΔG_{Hads}) [68]. It is broadly adopted to be a characteristic for a hydrogen evolution material (Cook et al., 2010; Parsons, 1958; Seh et al., 2017). ΔG_{Hads} is the most frequently recorded parameter among the three indicators that can demonstrate the binding strength of H atoms on the surface of an electrocatalyst.

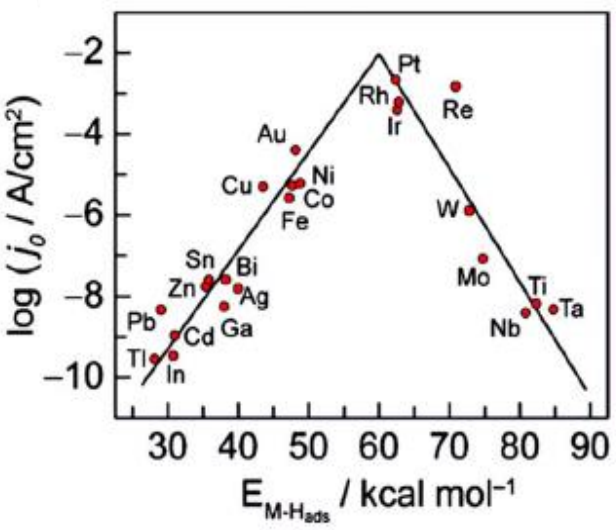

Figure 2.5: Volcano plot: exchange current density vs. the M–H bond energy for each metal surface (for acidic media). Adopted from ref.[Wang. Hydrogen production from water electrolysis: role of catalysts]

The relationship between the strength of the H_{ads}–M interaction and the HER exchange current density (j_0) that describes the intrinsic activity of the electrocatalysts and is determined by both kinetics and thermodynamics is illustrated on a 'volcano' plot. The volcano curve for HER on metal electrodes provides the comparison of different metals' activities in alkaline and acidic solutions. So far as it is known, the noble metals exhibit the highest HER performance. This can be seen on **Figure 2.5**. These metals have the H_{ads}–M binding energy that is near to the optimum, providing the thermodynamically favorable transition from reactants via intermediates to products [69]. The right slope of the experimental volcano curve conforms to the metals with large and negative hydrogen adsorption energy (ΔG_{Hads}). In this case, H_{ads} powerfully interacts with the surface that drives to the rapid discharge step. But, on the other hand, the strong H_{ads}–M interaction limits the formation of H–H bond and the subsequent recombination steps of the produced hydrogen (H_2) desorption [63]. The elements on the left side of the volcano curve exhibit weaker H_{ads}–M bonds that are attributed to metals with large and positive adsorption energy of hydrogen (ΔG_{Hads}). In this case, the weaker affinity with the catalyst surface confines the adsorption of hydrogen atoms on the electrode free catalytic site resulting in a slow discharge process that limits the overall turnover rate.

Thus, if the strength between the H_{ads}–M bond and the HER exchange current density (j_0) is too weak, the adsorption (Volmer) step will slow down the overall electrochemical reaction rate of water electrolysis, whereas the desorption (Heyrovsky/Tafel) step will restrain the overall water splitting reaction rate if the strength is too strong. Hence, the necessary and appropriate condition for an active HER catalyst when the hydrogen

generation is most feasible is the value of hydrogen adsorption energy ΔG_{Hads} near zero. In other words, any periodic element whose volcano curve is close to zero is expected to be an efficient HER catalyst owing to the optimal balance between absorption and desorption of hydrogen atoms on the free site of the electrode surface. The HER process is benefitted from a moderate value of hydrogen cohesive energy. Platinum (Pt) appears to be the best HER catalyst in alkaline media. It has the optimal adsorption energy of hydrogen exhibiting the highest value of exchange current density.

Nevertheless, the HER in alkaline media cannot be described solely by the free energy of hydrogen adsorption (ΔG_{Hads}) [70-72]. Recently, the water adsorption energy (E_{ads}) and the water dissociation energy (E_{ac}) have attracted growing attention because of their decisive roles in the Volmer step of the overall HER mechanism in alkaline solution. A smaller value of the water adsorption energy (E_{ads}) represents a better interaction between the electrocatalyst surface and the molecule of water, thus accelerating the following reactions. A lower value of E_{ac} indicates a faster process of water dissociation as less activation energy is needed. Therefore, an appropriate electrocatalyst have to possess a small absolute value of ΔG_{Hads} as well as low values of E_{ads} and E_{ac}.

It is worth observing that the energies obtained at the catalyst's surface are fundamental measures of the underlying procedures. They provide useful guidance for engineering suitable–catalysts. Extensive computational energetics are required to get a superior understanding of the HER in alkaline media. The alkaline HER activity is usually lower in the acidic solutions. It largely comes from the fact that the electrochemical reaction is impeded by the sluggish water dissociation process that–brings to the reaction rate decrease by 2–3 magnitude orders. For example, Pt catalytic activity in alkaline solutions is approximately two magnitude orders lower than that in the acidic media owing to the slow water dissociation proceedings (high E_{ac}) [70]. However, water electrolysis in alkaline solution is more preferable in industrial production. The efficient elaboration of effective catalysts with superior HER performance in alkaline media requires the electrocatalysts to have the properties of dissociating water and binding hydrogen species. Under this circumstance, the presence of a catalyst such as NiMo alloy-based materials to effectively split the O–H bonds is highly advantageous.

2.5. Parameters for evaluating catalysts performance

Electrocatalysts have played the fundamental role in overcoming the kinetic energy barriers for electrochemical reactions in water-splitting and fuel cells. For the last decades, the persistent attempts have been dedicated to developing inexpensive, efficient, and durable electrocatalysts for electrochemical water splitting in general, and HER, in

particular. Electrolysis of water is not only an upward-sloping electrochemical reaction, as represented by the positive value of Gibbs free energy (ΔG>0) but should overcome a substantial kinetic barrier as well. Although hydrogen and oxygen evolution half-reactions of water electrolysis proceed at the cathode and anode respectively and are in highly polarized conditions, the primary experimental parameters for evaluating their overall electrocatalytic activity are the same. The decisive role of a superior catalyst is to decrease the kinetic energy barrier and thereby enhance the electrocatalytic efficiency. As reported, various electrocatalytic parameters can be used to estimate and compare the overall electrochemical performance of diverse electrocatalyst materials from different aspects.

The analysis of electrocatalysts' performance for water electrolysis derives from several essential parameters for activity, stability, and efficiency[73-77]. The group of activity parameters is represented by the overpotential, Tafel slope, exchange current density and charge-transfer resistance that can be derived from the polarization curves (first two) and EIS(last one). They are the most frequently reported parameters for estimating and comparing catalytic activities of various electrocatalytic materials as well as the HER mechanisms and are subject to investigation in this work. The evaluation of electrocatalytic parameters for the synthesized electrocatalyst is the pivotal point of this thesis.

2.5.1. Activity parameters

Overpotential (η)

The overpotential (η) at a certain current density is one of the principal parameters for evaluating electrocatalysts' activity. Theoretically, the applied energy for the overall water splitting processes is equal to the thermodynamic reversible potential and only require the theoretical minimum cell voltage of 1.23 V to get over this kinetic energy barrier for the reaction. However, in a real system, due to the reaction hindrances, the applied electrode potential is larger than the thermodynamic reversible potential. Both the HER and OER require extra voltage for initiating the reactions to (i) overcome water electrolysis reaction's energy barrier and (ii) ensure that the reaction proceeds at a given rate.

The additional potential is defined as the overpotential (η). It mainly stems from the intrinsic activation barriers present on both anode (η_a) and cathode (η_c) and is calculated as the difference between the applied electrode potential under current load (E) and the thermodynamic reversible potential (E_r) as shown in Equation (20):

$$\eta = E - E_r \quad (20)$$

In principle, the measured overpotential (η) primarily originates in three parts: the activation overpotential, the concentration overpotential, and the system overpotential owing to uncompensated resistance.

The activation overpotential is predominantly contingent on each catalyst's intrinsic characteristic. The concentration overpotential takes place when there is a sudden concentration drop near the interface. It can be reduced by stirring the electrolyte or having a highly concentrated electrolyte. The resistance overpotential can be removed by ohmic drop compensation (iR-compensated or corrected overpotential) that can be done manually or by the system setting in the electrochemical workstation. Commonly, iR corrected overpotentials are reported, but an actual water electrolysis cell does not run according to iR corrected overpotentials. Hence, it is necessary to report the iR uncompensated data in addition to the iR corrected overpotential to further simulate a real water electrolysis system. Typically, the overpotentials at a fixed current density (e.g. 10, 100, 250 and 300 mA cm^{-2} geometrical surface area) are the most frequently reported quantitative parameters for evaluating the performance of different catalysts [74,75,78-82]. The lower overpotential (η) represents a superior electrocatalytic activity.

Generally, when combined with solar energy to produce hydrogen, the overpotential value that is equivalent to the current density of 10 mA cm^{-2} is viewed as a standard value to estimate the indicated catalytic efficiency and compare the performance among diverse electrocatalysts (McCrory et al., 2013, McCrory et al., 2015). It happens because the above-mentioned current density is approximately in the range of the most PV systems delivering voltage enough to split water. This current density is equivalent to a 12.3% solar-to-hydrogen efficiency under one sun illumination if there is no loss of Faradic efficiency of electrocatalysts. The overpotential (η) is an extensive parameter and its value is contingent on the amount of catalyst that used for the test.

Tafel Slope(b) and exchange current density(jo)

Another widely applied approach to compare the performance of electrocatalysts is to determine Tafel parameters. This method is beneficial to describe the kinetics of the HER in alkaline media [48]. Traditionally, the Tafel investigation drives to two fundamental physical characteristics: the Tafel slope that gives understanding of the reaction dynamics, and the exchange current density that is known as an indicator of the catalytic performance. Both indicators can be measured from the fitted parameters. Thus, for examining electrochemical activities, the Tafel analysis is associated with the Butler-Volmer equation in numerous research.

Theoretically, the electrochemical kinetics of electrochemical redox reactions are defined by the Butler-Volmer equation (21):

$$j = j_0[e^{-\alpha fn} - e^{(1-\alpha)fn}] \quad (21)$$

where j_0 – the exchange current density, α – the transfer coefficient of the anode or the cathode ($\alpha_a+\alpha_c=1$ or generally $\alpha_a= \alpha_c=0.5$), f – F/RT (F – the Faraday's constant, R – the universal gas constant, T – the absolute temperature), η – the overpotential, which is the difference between the acquired electrode and thermodynamic reversible potentials ($\eta = E - E_0$). This equation represents the total current that comes from both oxidation and reduction reactions and assumes that there is no mass-transfer effects.

The Tafel relation can be derived from the above Butler-Volmer equation assuming that the applied electrode potential is significantly larger than the equilibrium potential. It is important to take into consideration, that the Tafel equation is valid only for the sufficiently high overpotentials η, namely $e^{-\alpha fn} \gg e^{(1-\alpha)fn}$, i.e. if the extent of the electrode reaction in a reverse direction is negligible. The Butler-Volmer equation (22) is then transformed to:

$$\eta = \frac{RT}{\alpha F}\ln(j_0) - \frac{RT}{\alpha F}\ln(j) \quad (22)$$

where $\frac{RT}{\alpha F}\ln(j_0)$ corresponds to the term *'a'*, indicating that the intercept obtained from the plot of η vs. log j can be converted into the exchange current density (j_0). Empirically, this equation is known as the Tafel equation that is expressed by Equation (23):

$$\eta = a + b\log(j) \quad (23)$$

where empirical constants, a and b, have the theoretical form of

$$a = \frac{2.303RT}{\alpha F}\log(j_0), \quad b = -\frac{2.303RT}{\alpha F}\ln(j) \quad (24)$$

Equation (22) and Equation (23) represent theoretical and empirical forms of the Tafel relation, respectively.

When η = 0, the acquired current density (j) from the Tafel equation above is defined as the exchange current density (j_0). It describes the intrinsic activity of the electrocatalysts, i.e., the intrinsic charge transfer under the equilibrium conditions and is determined by both kinetics and thermodynamics[27,84]. The exchange current density provides the description of the catalytic activity in order to measure how vigorously both the forward and the backward reaction occur at the dynamic equilibrium[72].

In turn, the Tafel slope (b) gives the understanding of the HER reaction mechanism and its changes at different overvoltages as well as indicate how the electrode responds to the

applied potential. The value of the Tafel slope (b) is used as an indicator of the reaction pathway and is defined by the rate-determining step and its position in the reaction mechanism in terms of electron transfer kinetics. The Tafel slope (b) is based on the assumptions that a number of factors are constant, like the value of surface coverage, a symmetry factor, etc.

The Tafel equation values of the electrocatalytic process are generally obtained by analysing a polarization curve in the form of a plot (known as Tafel plot) of the logarithmic current density *log(j) vs iR*-compensated overpotential *η*. This plot is depicted on Figure 2.4 below.

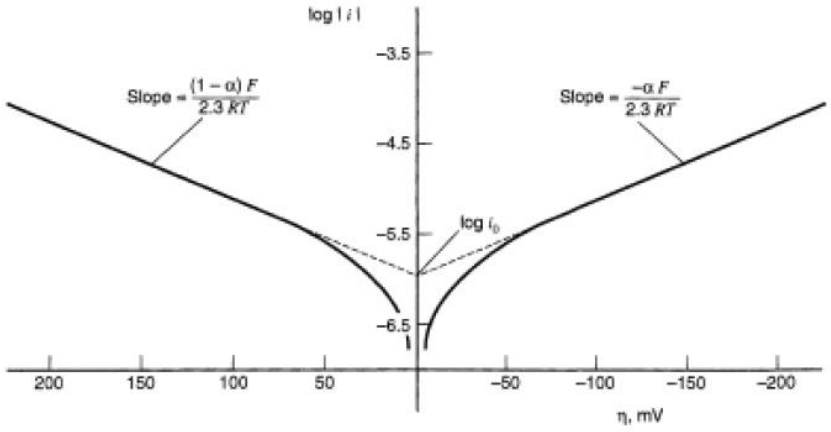

Figure 2.6: Tafel plots for anodic and cathodic branches of the current-overvoltage curve for $O + e^- \leftrightarrow R$ with α = 0.5, T = 298 K, and $j_0 = 10^{-6}$A cm^{-2},ref.[54]

The kinetic parameter *b* is extracted from the Tafel plot as the slope for the linear behaviour, where total *j* approximates to j_{ox} (left-hand branch on Figure 2.4.) and total *j* approximates to j_{rd} (right-hand branch on Figure 2.4.). It is usually measured in mV dec^{-1}. The empirical constant *a* as an intercept with log(j) can be extracted from the obtained exchange current density, j_0. It is worth noting one peculiarity about the extraction of the above-mentioned kinetic parameters in the real experimental studies. When the Tafel plots are experimentally plotted, they significantly deviate from the theoretical behaviour indicators as shown in Figure 2.4. As result, solely the stable kinetic region should be used for the extraction of kinetic parameters. This region is found in between the initial linear region where the reaction under investigation has already started and the noticeable kinetic activity that has not manifested yet and the end region where the kinetic activity has already decreased approaching to the end of the reaction. In practice, this region has to be identified from the plot on an individual basis, carefully inspecting the entire plot[51,54,84].

The Tafel analysis assesses the electrocatalyst performance from the relationship of the overpotential vs. kinetic current. The Tafel slope (b) and exchange current density (j_0) are very powerful kinetic parameters and are the primary characteristics for evaluating catalysts' activity. The exchange current density is obtained by means of extrapolations of the linear part of the Tafel plot by extracting the current at zero overpotential. Tafel slope is usually derived from the linear sweep voltammetry (LSV) results. Another method to obtain the Tafel slope is from the electrochemical impedance spectroscopy (EIS) data by plotting log(1/Rct) vs. η (where Rct is the charge transfer resistance). It is suggested that the latter method can only exhibit the charge transfer kinetics, while Tafel slopes obtained from the LSV method may comprise the contributions from the catalyst and electrode resistance[85] .

Tafel slope is an intensive value, i.e., its quantity is independent of the area of the catalyst surface. On the contrary, the exchange current density value is extensive parameter that is contingent on the extent of the catalyst surface. The selected experimental parameters (e.g., potential ranges) considerably affect the value of the Tafel slope. The same is valid for the exchange current density value that is influenced by catalysts' intrinsic properties as well as the experimental conditions (e.g., temperature and electrolyte composition).

When these two quantities are considered together, they can point out potential causes (electronic, geometric, or combined) of the improvement in the electrocatalytic performance of an electrode after the modification of the electrode or change in the synthesis conditions. In general, the calculated Tafel slope is inversely related to the charge transfer coefficient. In other words, catalysts with higher exchange current density (j_0) are expected to favour a smaller Tafel slope, indicating faster electrocatalytic reaction kinetics, namely a greater charge transfer rate and a lower reaction barrier[67]. Apparently, a desirable high-performance electrocatalyst should exhibit a low Tafel slope and a high exchange current density. However, it is not possible to obtain high exchange current densities and low Tafel slopes at the same time. Therefore, to evaluate an electrocatalyst performance, the compromise between these two parameters should be considered. [72,84]

NiMo based electrocatalysts have the following kinetic parameters: $Ni_{75}Mo_{25}$ on mild steel substrate with Tafel slope of 170 mV dec^{-1} [86], Ni_4Mo with MoO_2 on Ni-foam substrate with Tafel slope of 30 mV dec^{-1} and exchange current density of 1.24 mA cm^{-2}[87], $Ni_{70}Mo_{30}$ on mild steel substrate with Tafel slope equals to 62 mV dec^{-1}[28], Ni4No nanosheets with Tafel slope of 45 mV dec^{-1}[40], $Ni_{62}Mo_{38}$ on Cu substrate with Tafel slope equals to 212 mV dec^{-1} and exchange current density of 6.2 mA cm^{-2}[32], and NiMo-NWs on Ni-foam with Tafel slope equals to 86 mV dec^{-1} and exchange current density of 4.59 mA cm^{-2}[90].

In experimental practice, Tafel slopes, b are used to identify both RDS and reaction mechanism. Theoretically calculated value of Tafel slope for Volmer step is 118.2 mV dec^{-1}, for Heyrovsky step is 39.4 mV dec^{-1} and for Tafel step is 29.6 mV dec^{-1} [92]. Therefore, when *b* is close to 118.2 mV dec^{-1} and it is in between 118.2 mV dec^{-1} and 39.4 mV dec^{-1}, then the process follows Volmer-Heyrovsky mechanism, where Volmer step is RDS. If b is closer to 39.4 mV dec^{-1} and also found between 118.2 mV dec^{-1} and 39.4 mV dec^{-1}, then the process follows Volmer-Heyrovsky mechanism, where Heyrovsky is RDS. When b is exceed 118.2 mV dec^{-1}, it is believed that the process goes by Volmer-Heyrovsky mechanism, where Volmer step is RDS. In case of *b* is in between 39.4 mV dec^{-1} and 29.6 mV dec^{-1}, the mechanism is Volmer-Tafel with Tafel step as RDS.[27,91]

2.5.2. Stability parameters

Apart from the above-mentioned parameters that focus on the catalysts' activity, 'stability' represents another essential complementary indicator in the development of a feasible electrocatalyst in practical industrial applications. The most common method to evaluate the long-term stability of electrocatalysts is to perform the long-term chronoamperometric (CA) tests [93-95]. The information on the stability measurements has to be available for the materials that demonstrate favourable properties that could be considered as the candidates for an industrial use.

At constant current densities during a long operation (usually for more than 12 hours) the CA test measures the current variation with time under a fixed potential while recording I–t curves. The superior stability of an electrocatalyst is characterized by the duration of time the potential or tested current remain constant. For example, the overpotential increase at a constant current density or the current decline at a fixed potential can determine the catalysts' stability. The current density is usually set larger than 10 mA cm^{-2} for a test time span of at least 12 hours to compare with the different research groups of electrocatalysts. The less variation of the overpotential or the current density denote better longevity.

The small rise in overpotential at a selected current density (*e.g.,* 10 mA cm^{-2}) for more than 12 h by chronopotentiometry or an invisible change of current density for more than 12 h by chronoamperometric test is sufficient to distinguish the high efficiency of catalysts. The variation in the actual current densities and thickness a catalytic material between investigations comprises further complexities. The measurements conducted for a short period of time will not detect the deteriorations of the catalyst material if the substance is too dense for these effects to be explicit. Moreover, the estimations made at the low current density will indicate a naturally slow decomposition of the material.

2.5.3. Efficiency parameters

Turnover frequency

The turnover frequency (TOF) is a useful measure of a catalyst efficiency and an important kinetic parameter. In general, TOF is defined as the number of reactants that can be converted by the catalyst to the desired product with respect of the time unit per active catalytic site. For the hydrogen evolution reaction, turnover frequency is determined as the average number of hydrogen moles emitted per active site and time unit.

The turnover frequency is independent of the active surface area of a catalyst and can be used to compare various materials. The main drawback of the TOF parameter is the difficulty of the calculation of the precise number of active sites per electrode surface for most heterogeneous electrocatalysts. Significant errors may arise in case a material is composed of more than one element, as more types of heterogeneous active sites may appear. Despite being relatively imprecise, the calculated turnover frequency is still a beneficial tool for comparing the catalytic activities among diverse catalysts, especially under identical conditions or within homogenous systems.

Faradaic efficiency

Faradaic efficiency (FE) is a quantitative indicator that is employed to determine the electrons' efficiency in an external circuit transmitted to the electrode surface for the electrochemical reaction. The definition of faradaic efficiency in the hydrogen evolution reaction is the ratio of the experimentally produced quantity of H_2 or O_2 to the theoretically derived hydrogen amount. FE theoretical values are quantified from the integration of the CP or CA tests. The experimental product amounts can be measured by investigating gas chromatography (GC) or the water displacement method. Normally, the reported FE in the HER is close to 100%, and a higher FE represents a better selectivity for the HER process in the alkaline media.

In conclusion, the selection of the analysis techniques for the catalysts' activity, stability, and efficiency parameters are contingent on the particular focus of the research. Moreover, based on the synthesis and composition of electrocatalysts, the contemporary analysis of the activity, stability, and efficiency can be grouped into three areas with the focus of mechanistic determination, structural characterization, and performance evaluation.

While the studies of the potential- or current-time curves provides data for evaluation of electrocatalysts' durability performance that is highly valuable for the practical industrial applications, the determination of the Tafel slope, overpotential, exchange current density,

turnover frequency and faradaic efficiency provides the fundamental indicators for estimating the electrocatalytic mechanism. The combination of the electrochemical methods with the microscopic and spectroscopic techniques allows for the structural characterization that is essential for gaining insights into the development of the stable and active catalysts.

The activity parameters like Tafel slope, exchange current density and change transfer resistance will be investigated in this thesis in detail. The stability and efficiency parameters are subject to future work.

3. Literature

This chapter presents the literature review of NiMo electrocatalysts as cathodes in electrochemical cells. The features and observations related to the structure, morphology, composition, and electrocatalytic activity are presented in the first part of this review. The second part gives an overview NiMo alloys prepared by electrodeposition, which is the main synthesis employed in this work.

3.1. NiMo structure, morphology and composition

Among the reported electrodeposited alloys, NiMo is one of the best bimetallic alloys among all nonprecious electrocatalysts. It is considered an excellent comprehensive material with outstanding physicochemical characteristics [96-98] that can be a promising alternative to Pt for the HER.[99-101]

NiMo alloy is a bimetallic alloy that can possess varied final structures depending on the synthesis methods, conditions, and substrates. In general, NiMo alloys are presented in the form of nanoparticles or planar porous morphology. According to the XRD investigation performed by Q. Zhang et al.[40], the ultrathin NiMo alloy nanosheet with Ni:Mo ratio of 4:1 appears to have a body-centered tetragonal phase with lattice planes (220) and (310) located at 44.1° and 50.9°, respectively. At the same time, the study of nanocrystalline NiMo alloy on the steel coupon conducted by Halim et al.[89] has revealed that all the obtained samples have diffraction peaks around 43-44° indicating the presence of a one-phase solid solution of NiMo with a face-centered cubic structure. Another work[38] has shown that all the compositions from the series of NiMo, Ni2Mo, Ni3Mo, Ni4Mo, and Ni6Mo alloys produced by arc melting have fcc structure with the slight tetragonal distortion. The distortion increases with increasing Mo content as the larger Mo atoms tend to expand the matrix lattice of fcc Ni. Furthermore, it has been shown that phases Ni3Mo, Ni4Mo, and Ni6Mo are most likely the pure ones. Back in 1989, Raj and Vasu[86] already reported that the active phase of NiMo alloy deposited on mild steel foil had a tetragonal structure.

NiMo alloys can also have the amorphous structure as it has been presented in the research works of Pehlivan et al.[28] and L.Zhang et al.[102], where XRD has shown no significant diffraction peaks for NiMo films prepared on Ni-foam substrate. The investigation of nanocrystal and amorphous NiMo alloys demonstrates that their reactivity and stability for HER are closely associated with the microstructure and phase composition. As hydrogen evolution cathodes, NiMo alloys show excellent electrochemical characteristics because of the internal amorphous structure of the species [103–107]. The NiMo alloys microstructure determines the macroscopic qualities of the electrode. The principal characteristic of the amorphous state is metastable state that directly regulates the lifespan of the electrode in practical implementation. The crystallization conduct of the amorphous state defines

the structural phase of the NiMo alloy, influencing the original structure and performances of the crucial materials.

Therefore, the researchers obtained similar results where NiMo alloys have cubic cell structures with different degree of hexagonal distortions. However, the amorphous or microcrystalline NiMo alloys can be formed as well.

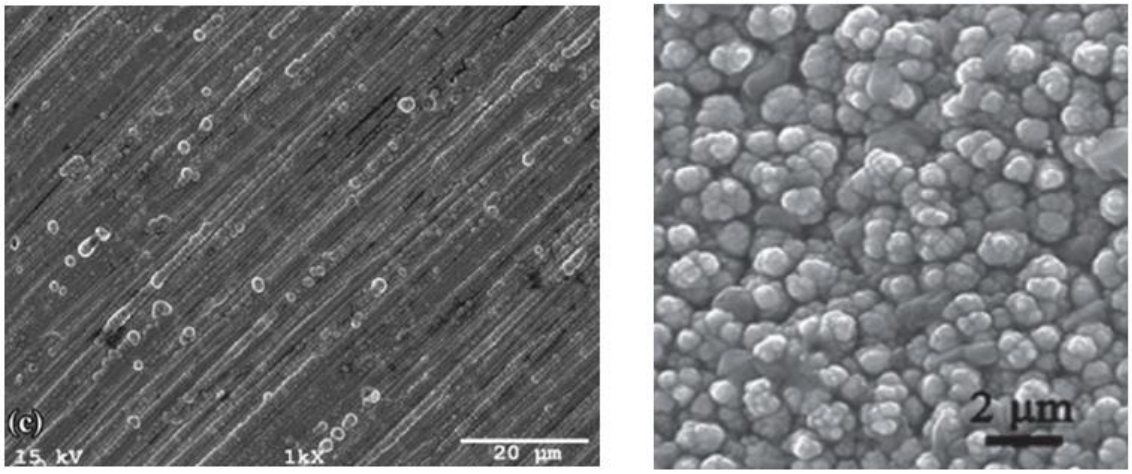

Figure 3.1: Typical morphologies of NiMo alloy. The 3D structures with oriented grown columnar shapes[9] (left) and with a coarse surface with composite nanoparticles embedded in matrix phase[7] (right)

Ni–Mo alloy is regarded to be the benchmark of non-precious catalysts due to its similar surface electronic state to platinum[40]. Morphology engineering is a popular and efficient strategy to obtain excellent catalytic activities. The improvement in NiMo alloys' electrocatalytic performance can be attained via design of the dimensional architectures (0 – 3D), porous structuring, facet engineering, phase engineering, interface engineering, component regulation[27,88,108], active sites exposure like, for example, enriching active sites through nanosizing, and optimizing channel structures for mass transport.[109-112]

In general, the morphology of NiMo alloys is presented by 3D structures that are uniform[28,33] and have coarse areas with nanoparticle-like composites ranging from 10 nm to 100 nm or oriented grown columnar structures[32,33,113]. Such type of morphologies are shown in Figure 3.1. The diverse 3D structures include not only the films and the uniform deposits with the embedded particles on their surface but also nanorods (up to 500 nm in length)[102] and nanosheets (~ 10 nm thickness)[114].

Numerous research have been dedicated to the optimization of NiMo alloy's characteristics such as composition, microstructures design, surface area, and the morphology of the particle size and deposit. To improve the deposition performanceHong Xu et al.[96] have designed the mixed-structured NiMo alloys by adding a modifier to the amorphous NiMo

alloy coating. Considering the amorphous and nano-crystalline cluster structure and their activity, the composition and phase structure of different mixed-structured NiMo alloys have been investigated using X-ray powder diffraction, whereas their electrochemical activity have been determined by electrochemical analysis. The experimental results demonstrate better structural stability and higher electrochemical activity of the mixed-structured NiMo alloy than that of the amorphous alloy that results from the enhanced contact surface and the greater number of active centers in this material structure.

L.Zhang et al.[102] have reported about a novel fabrication of NiMo alloy well-aligned nanorods HER catalyst deposited on Ni foam substrate that have exhibited the advantageous vertical nanorods architecture and have shown the most efficient activity for HER compared to the one metal film. As stated by L.Zhang et al. the greatly enhanced electrocatalytic activity is ascribed to the synergistic interaction between Ni and Mo as well as the ordered array geometry. As supported by other investigations, In comparison to the planar porous electrodes or ordinary nanoparticles, the well-aligned nanorod arrays produce greater surface area of active materials. The open space inside the nanorod arrays contributes to penetration and diffusion of ions in the electrolyte, allowing superior productivity of active elements as well as the timely release of the formed hydrogen bubbles.

Among different micro- and nanostructures, 3D NiMo bimetal aerogels showed significant potential in electrolytic water splitting owing to abundant active sites, interconnected mass transport pathways, and their conductive and self-supporting bond architecture [115-117]. In the work of B.Zhang[42] there was demonstrated excellent HER and OER performance of the optimized P-doped NiMo bimetal aerogel followed by in-situ P doping with NaH2PO4 have shown the significantly low overpotentials of 69 mV for HER and 235 mV for OER at a current density of 10 mA cm-2. The calculations have revealed a reduced energy barrier and much easier water dissociation of P-doped NiMo bimetal aerogel, that have required a low cell voltage of 1.46 V to obtain an overall water electrolysis current density of 10 mA cm-2.

In contrast to planar electrode substrates, 3D porous structures of NiMo cathodes provide more extensive surface areas for heterogeneous catalysts. These architectures enable to substantially increase the loading of the electroactive materials, contribute to the diffusion of electrolytes, and enlarge the surface area as reported by Y. Wang et al.[33].

Furthermore, ultrathin 2D NiMo bimetallic nanoarchitectures demonstrate ultrahigh surface area, unsaturated surface coordination, and powerful quantum confinement of electrons in two dimensions that exhibit promising electrocatalytic utilisation. The ultrathin 2D NiMo alloy nanosheets for HER synthesized by Q. Zhang et al.[40] in situ topotactic

reduction method has exhibited an overpotential of 35 mV at current density of 10 mA cm-2, along with a Tafel slope of 45 mV decade−1, thus displaying a comparable intrinsic activity to the commercial Pt/C catalyst.

Among other strategies to influence the composition of composition of NiMo alloys are synthesis conditions, doping, defect engineering, and enhancing conductivity with the assistance of highly conductive substrates.[27,88,108] The composition of NiMo alloys has diverse nature and strongly depends on the method and synthesis conditions. Thus, Pehlivan et al.[28] have obtained composition of 30 wt% Ni and 70 wt% Mo by reactive DC magnetron co-sputtering on Ni foam, Ni foil, carbon cloth, ITO-coated glass, and FTO-coated glass. Manazoğlu et al.[32] have researched 2.22 wt% Mo and 87.78 wt% Ni, 24.2 wt% Mo and 75.8 wt% Ni, 37.8 wt% Mo and 62.2 wt% Ni at different Ni:Mo molar ratios and pH values using electrodeposition from bath solutions. T. Wang et al.[12] have applied N-doped graphite nanotubes as support and their catalyst has contained ca. 30 wt% C, 15 wt% Ni, 35 wt% Mo, and 1 wt% N. Raj and Vasu[4] have been able to achieve a composition of 70 wt% Ni and 30 wt% Mo by electrodeposition. Also, Tang et al.[118] have found out that the uniform distribution of both Ni and Mo in NiMo alloy is present before and after the hydrogen evolution reaction (HER). The proportion of Mo itself in synthesized NiMo is believed to be dependent on the initial content of Mo in precursor solution[47] and on the deposition current density[89].

Another important feature that has been observed by many different groups of researchers[33,86,87,113,114,119] is the presence of the primary Ni4Mo phase in the total composition of NiMo alloys. Its specific synthesis procedure and surface morphology have played a major role in the catalytic activity of the material.

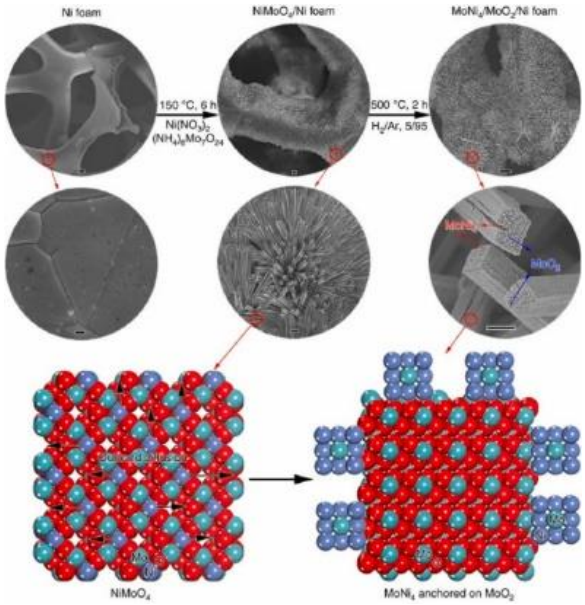

Figure 3.2 Synthesis of Ni4Mo supported by MoO_2 cuboids on Ni foam catalyst, ref. [62]

According to the available reported data, this phase has always been the most electrocatalytically active one and played the role of the main phase responsible for the overall electrocatalytic activity. Therefore, a ratio of Ni:Mo of 4:1 has increased the HER activity and can be considered for further extensive study. Introducing XPS for electrodeposited alloys can reveal new key features in the study of the electrocatalysis at NiMo surface.

3.2. Electrocatalytic performance

The key parameters for selecting of an active catalyst for efficient HER are strong intrinsic activity of a material, good electrical conductivity, large surface area, low overvoltage, good electrochemical stability of performance, low cost, and ease of use. Despite the fact that these requirements are hard to meet simultaneously, many electrocatalytic materials for cathodes have been advanced and investigated to respond to this request.

Many attempts have been made to interpret the HER overpotential characteristics of individual metals applying different electronic and/or physical parameters, including the metals' bond-strength, the atomic number, the electronegativity, the work function, and the heat of hydrogen adsorption on metals. The electrochemical performance of pure metals is described in 'volcano plots' that shows the relation between the Me–H bond strength and current density as a measure for the catalysts' activity. By merging two or more elements, researchers intend to combine the physical properties of a weakly and strongly adsorbing catalysts as well[38].

For the HER in the alkaline media, pure Ni and Ni-based alloys are one of the most investigated catalytic materials on the account of their increased electrocatalytic activity towards the HER and excellent stability in an alkaline media, among which NiMo alloy is reported to be the best one[29]. A growing number of the investigations on the fabrication of effective cathode materials for hydrogen evolution reaction has been focused on Ni alloys with iron group metals because of their superior catalytic performance under alkaline conditions, stability at rising temperatures and appropriate oxidation and corrosion resistance[120]. These properties combined with reasonable costs, simple application and good electrical conductivity are attractive characteristics for selecting NiMo compounds as a cathode for water splitting.

The reported data on the electrocatalytic performance of NiMo alloys disperse from the values that are typical for pure Ni electrodes to values that are orders of magnitudes higher [8-10]. The origin of these discrepancies in activity data and as well as the reasons behind extremely high electrocatalytic performances in some cases are not yet fully understood.

However, the key factors behind the explanation of superior electrocatalytic performance of nickel-molybdenum alloys compared to pure metals are the position on the volcano plot and the position of the d-band center of elemental nickel and molybdenum as well as the specifics of their interaction with hydrogen. In NiMo alloys, Ni is reported to strongly bind hydrogen that prevents the creation of a H–H bond and subsequent desorption of the produced hydrogen, J. Zhang et al. [87]. Thus, Ni atoms are widely acknowledged as the outstanding water dissociation centres. On the contrary, Mo atoms have excellent adsorption characteristics towards hydrogen] as the left-side Mo exhibits weaker Me–H bonds and adsorbs hydrogen too weakly [121-124]. By merging two or more elements, researchers intend to combine the physical properties of a weakly and strongly adsorbing catalysts as well. Therefore, NiMo alloy electrocatalyst (Nix-Moy) can be a promising candidate to productively diminish the energy barrier of the Volmer step and accelerate the sluggish kinetics of hydrogen evolution reaction in alkaline media.

In separate investigations[17,125-130] different researchers have demonstrated that by alloying nickel with molybdenum results in a higher intrinsic HER electrocatalytic activity compared to industrially applied pristine nickel or molybdenum cathodes. The reason for the enhanced intrinsic activity of NiMo alloys is attributed to the synergistic interaction between adjacent atoms of nickel and molybdenum when Mo is dispersed in the Ni matrix, thus expanding the electrode's real surface area. Moreover, the expansion of the Ni-15at.% Mo alloy electrocatalytic activity for the HER has been attributed to the electron density's modification in the d-shell (electron transfer between electron-rich Ni and electron-deficient Mo) upon alloying Ni with Mo that results in unsaturated d-orbits similar to Pt [17,131].

According to the Engel-Brewer intermetallic bonding model, whenever the transition metals of the left half of the transition series with empty or less-filled vacant d-bands (e.g., Mo) are alloyed with those on the right half of the transition series with more-filled d-orbitals (e.g., Ni) that have internally paired d-electrons not available for bonding in the pure metal, a synergistic effect in the electrocatalysis for the HER of these materials arises. This process leads to the greatest bond strength and the superior stability of the intermetallic alloy phases. Thus, HER activity of NiMo alloy is considerably greater than that of industrially applied nickel cathode. Moreover, the HER activity expands with growing Mo quantity because the electrocatalytic activity of NiMo alloys is qualitatively proportional to Mo quantity, according to the above-mentioned theory [32].

Jeremy A. Bau et al.[130] have put forward three major mechanisms to consider the high electrocatalytic activity of NiMo under HER, i.e., 1) the advantageous reaction energetics at NiMo alloy interfaces, 2) the enhancement of the surface area via Mo dissolution and 3)

Mo as an overflow valve to impede the inactivation of Ni hydride. All the three mechanisms emphasize on the metallic Ni role as the predominant active site.

To improve NiMo electrocatalytic performance researchers have experimented with numerous parameters like, for example, creating advanced structures in the form of ultrathin 2D nanosheets[40], 3D nanoporous Ni–Mo electrocatalysts[33], unsupported Ni−Mo nanopowders[132], nanocrystalline deposits[89], 3D porous MoNi4 networks constructed by 2D nanosheets as bifunctional electrocatalysts[114], nanofibers[133], NiMo2C nanocrystals HER catalyst supported on N-doped graphite nanotubes[12], binary alloy codeposits[119], films[28], film/nanorods[102]. Among other popular parameters that have been thoroughly investigated is the application of various substrates with different porosities and conductivities such as foil, foam[40],[28] , indium tin oxide (ITO)-coated glass, carbon cloth (Ccloth), and fluorine-doped tin oxide (FTO)-coated glass[28]. The type of the substrate is very important as it may influence both the initial growth conditions and the final charge transfer in the catalyst system as a whole. Other optimisation parameters that affect the catalytic activity is Ni:Mo mole ratio[28,32,33] in the electrolyte, current densities[33,89], electrodeposition time[32,33], pH value as well as stability of electrodeposited NiMo alloy in the alkaline solution.

The vast majority of research in the last decades have been aimed at designing an innovative and highly efficient NiMo alloys with superior activity characteristics for effective hydrogen production. Raj et al.[86] have extensively investigated electrodeposited Ni-based alloys and figured out that binary and ternary alloys that contain Mo are the most active HER materials. McCrory et al. have investigated HER catalysts based on a great number of bimetallic alloys and have revealed that the NiMo alloy have exhibited the lowest overpotential.

Moreover, their findings have been supported by other studies that have shown that Ni–Mo electrodes have exhibited greater electrocatalytic activity than other Ni-based alloys such as Ni–Fe, Ni–Co, Ni–Zn and Ni–Cr [134,29]. L.Zhang et al.[102] investigated the catalytic activity of NiMo alloy on Ni foam electrode for the HER in alkaline solution by linear sweep voltammetry (LSV) by comparing it with other substrates – Ni foam, Ni/Ni foam and Mo/Ni foam at the same condition. The obtained results clearly stipulates that NiMo alloy on Ni foam electrode has demonstrated a superior electrocatalytic activity than other three electrodes achieving the lowest onset potential of 5 mV. In addition, NiMo/Ni foam electrode has exhibited the largest current density of 277 mA cm^{-2} at the overpotential of 0.35 V, compared to the three others. Furthermore, the activity of the obtained NiMo alloy on Ni foam is superior to almost all the currently known non-precious metal catalysts for HER. The presence of molybdenum in nickel electrode has distinctly

shown to lead to a considerable improvement in its performance that can be attributed to the synergistic effect as well as the larger active surface areas.

There are numerous studies that show that the catalytic activity for hydrogen evolution is qualitatively proportional to the molybdenum content in NiMo alloys [125,127,136]. Halim et al.[89] investigation have exhibited the lowest Tafel slope for the cathodic region (79mV/dec) as well as the lowest potential (-0.9V) at a constant current of −0.04 mA cm-2 for NiMo electrodeposited alloy containing 15% molybdenum. Furthermore, according to Halim et al.[2] the Mo quantity's increase and the strengthening of roughness are the key factors for intensifying the electrochemical activity of NiMo alloys for HER. The similar explanation has been provided by Nee et al.[137], Arul Raj and Venkatesan[134], and Divisek et al. [138], who have demonstrated NiMo alloys' behaviour prepared by different synthesis methods. In their research, Y. Wang et al.[33] have designed 3D nanoporous NiMo electrocatalysts on Cu foam with optimized composition, dimensions and nanoporosity using electrodeposition technique. By optimizing NiMo ratio, electrodeposition time and current density, 3D nanoporous NiMo electrocatalysts have demonstrated the improved composition-dependent electrocatalytic activity with the lowest overpotential of 10 mV at 10 mA cm-2 obtained at 200 mAcm-2 for 3600 s and superior electrochemical stability. The researchers attribute the Ni-Mo's improved HER performance with very small overpotential and much higher current density compared to that of Pt/C, to the NiMo ratio (4:1), the large surface area, and the applied method.

Mckone et al. reported a NiMo nanopowder fabricated from the nickel-molybdate precursors with a very low overpotential of 80 mV at a current density of 20 mA cm^{-2} in 0.5 M H2SO4, but the shown stability was unsatisfactory. Pehlivan et al.[28] studied the effect of several substrates on HER of Ni−Mo electrocatalysts. They carried out the electrochemical characterization with LSV at direct current potentials between 200 and −400 mV vs the reversible hydrogen electrode (RHE) in 1M NaOH encompassing the HER and electrochemical impedance spectroscopy (EIS) in the frequency range of 0.7 Hz − 100 kHz. LSV graphs have demonstrated/shown the highest HER rate for the film coated on the Ni foam, followed by the ones coated on the Ni foil, C-cloth, FTO, and ITO. They obtained the lowest HER overpotentials for films on the Ni foam at all current densities (−157 mV vs RHE at current density of 10 mA cm^{-2}), whereas the overpotentials have grown in the order of nickel foil, carbon cloth, fluorine-doped tin oxide, and indium tin oxide glass.

4. Experimental methods

The experimental part is divided into four parts: pre-treatment of Ti foil substrates by two different methods; synthesis of electrocatalytic NiMo alloy on Ti substrate's surface by electrodeposition at the best predetermined conditions of the deposition current and time; electrochemical characterization, and morphological, compositional, and structural characterization.

The chemical etching at different time intervals and the mechanical polishing by two different size grinding papers were employed as two methods of substrate pre-treatment. The electrodeposition of NiMo alloy from a bath solution containing Ni- and Mo-ions with the adjusted pH was applied for the synthesis of the materials in this study. The electrochemical characterization of the synthesized NiMo alloys was performed by Linear Sweep Voltammetry (LSV) and Electrochemical Impedance Spectroscopy (EIS), The study of morphology, composition, and structure was conducted by Scanning Electron Microscopy (SEM), Energy Dispersive X-Ray Spectroscopy (EDS), and X-Ray Diffraction (XRD).

4.1. Chemicals

Nickel (II) sulphate hexahydrate powder ($NiSO_4 \cdot 6H_2O$, purity of 98.0 %), sodium citrate dehydrate powder ($Na_3C_6H_5O_7 \cdot 2H_2O$, purity of 98.0 %), sodium molybdate dihydrate powder($Na_2MoO_4 \cdot 2H_2O$, purity of 99.7 %), potassium hydroxide powder(KOH, purity of 90.0 %) were purchased from Sigma-Aldrich. All the above-stated chemicals were utilized without any further purification. All the electrolyte and bath solutions were prepared with the in-house deionized water with resistivity 18.2 MΩcm. The titanium (Ti, purity of 99.7%) foil of 0.125 mm thickness and nitrogen gas were also purchased from Sigma-Aldrich.

The mixture of the concentrated hydrofluoric acid (HF) and the concentrated nitric acid (HNO_3) that were purchased from Sigma-Aldrich as well as the distilled water in the proportion of 3:1:6, respectively, was applied as an etching agent for the Ti substrates. 1 M of KOH solution was prepared for the electrochemical characterization by mixing 62.34 g of KOH powder with 1 dm^3 of distilled water in a volumetric flask. Nitrogen gas (N_2, purity of 99.999%) was bubbled through the KOH solution during the electrochemical characterization experiments to remove the dissolved oxygen in the solution. For pH adjustment, ammonia solution (NH_4OH) of 28% concentration. Further information regarding safe use of chemicals, safe performance of the experiments, and other important HSE moments are presented in **Appendix A**.

4.2. Pre-treatments of Ti substrates

Two types of pre-treatments, chemical etching and mechanical polishing, have been employed to compare their effects on the electrocatalytic performance of the NiMo alloys under the study and identify the best type of pre-treatment. Titanium foil (99.7%) was cut into 24 rectangular strips of 5 cm x 1 cm, i.e., 12 samples for each pre-treatment method. 12 rectangular strips samples were divided into four categories to conduct the chemical etching pre-treatment at four different time intervals, namely 1 second, 2 seconds, 3 seconds, and 4 seconds with three repeated trials for each etching time interval. Each condition was repeated in triplicate. This has been done with the aim to provide better reliability of data. The other 12 samples have been utilized for the mechanical polishing treatment. The number of polished samples is justified by producing the total equal number of samples to the etched ones.

4.2.1. Chemical etching of Ti substrates

All the twelve test specimens were subject to chemical etching in the mixture solution of the concentrated hydrofluoric acid, concentrated nitric acid and distilled water. Every rectangular strip was etched separately. For the first three Ti substrates the acid etching treatment was performed by dipping the samples into the acid mixture solution for 1 second and afterwards dipped into the beaker with the distilled water to stop the reaction and remove the residuals of the acid mixture from the samples' surface.

For each triplicate of Ti substrates, the etching time was increased by 1 second, therefore for 2, 3 and 4 seconds.

4.2.2. Mechanical polishing of Ti substrates

In the case of the mechanical polishing of the Ti substrates, the surfaces of the substrates were carefully prepared by mechanical polishing using grinding papers with two different meshes, i.e., 1200 and 4000. The hand polishing was applied due to inability to polish thin foils by polishing machine without damaging of the remaining parts of the samples. Initially, all the samples were hand-polished using 1200 mesh grinding paper until the required area of 1 cm^2 appeared in light grey colour. Then, all the sample were exposed to the same procedure using 4000 mesh grinding to improve the quality of polishing. Since, the samples were mechanically deformed during the polishing procedure, a cold pressing was applied to flatten the substrates for the further repeated polishing procedure in order to polish all the unpolished areas left after the first polishing round. The Ti rectangular strips s were placed in the press in between two aluminium rectangular blocks to fix the samples and avoid the unwanted mechanical scratching from the surface of the pressing rods. The pressing procedure was done at the pressure weight of 1 ton. After the pressing the polishing procedure was repeated as described above.

After both types of pre-treatments were completed, the substrates were covered by Loctite epoxy from both sides, leaving uncovered area of 1 cm^2 at the bottom of the substrates from one side, and approximately 2 cm^2 at the top of the substrates from both sides. This was done for normalizing and holding a fixed working area of each substrate. The top region of the substrates was left uncovered for electrical contact with the experimental setup.

4.3. Synthesis of NiMo alloy on Ti substrate

The NiMo alloys were electrodeposited on Ti substrate applying a galvanostatic technique at room temperature of approximately 25°C. The bath solution containing the electrodeposition electrolyte that consists of 79 g of $NiSO_4 \cdot 6H_2O$, 88 g of $Na_3C_6H_5O_7 \cdot 2H_2O$, and 44 g of Na_2MoO_4 dissolved in 1 dm^3 of deionized water, based on the method presented by Fan et al.[19]. Ammonia solution was used as a basic agent to adjust pH of the electrodeposition bath solution at 10.5. The pH adjustment was controlled by pH-meter.

In the following step, a two-electrode electrolytic cell was constructed as shown in **Figure 4.1**. The working electrode wire and the working sense wire were connected in the short circuit and connected to the upper uncovered part of a Ti substrate by metal clamps, making the cathode of the electrolytic cell. The deposition occurred on this cathode. The counter electrode lead and the reference electrode wire were connected in the short circuit and attached to the porous Ni-foam plate by metal clamps, making the anode of the cell. The connected electrodes were immersed in the electrodeposition bath solution "face-to-face" close to each other. The electrochemical measurements were done with a Parstat 2273 potentiostat utilizing the the "Electrochemistry `PowerSuite' " software. The electrodeposition of NiMo alloy at Ti substrates was performed at a constant current density of 20 mA cm^{-2} with deposition time kept at 15 minutes (900 s) that was chosen as optimal conditions for the electrodeposition from series of preliminary electrodeposition experiments. After the electrodeposition, the obtained NiMo alloys at the differently processed Ti substrates were rinsed several times with deionized water and then dried at room temperature in air.

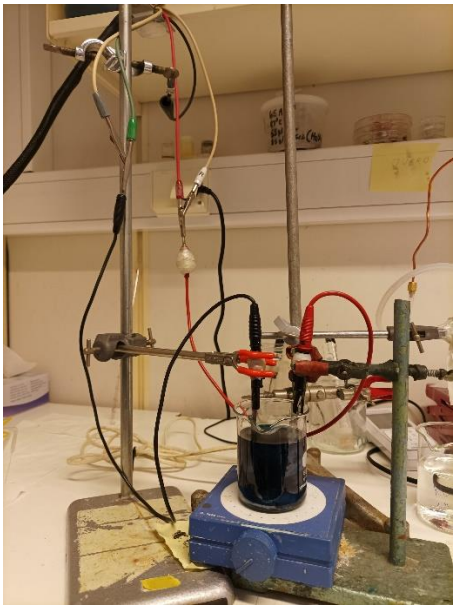

Figure 4.1: Electrolytic, two-electrode cell for electrodeposition of Ni and Mo ions on Ti substrates

4.4. Electrochemical characterization of the synthesized NiMo alloy

Electrochemical characterization of the synthesized NiMo electrode samples were carried out by LSV and EIS techniques in 1 M KOH at pH 14 using the three-electrode system. This setup shown in Figure 4.2 demonstrates the similar cathode setup as with the two-electrode system, with one exception that only the counter electrode lead was connected to a carbon graphite plate becoming new counter electrode and the reference electrode wire was connected to the Hg/HgO (1M NaOH) reference electrode. The reference electrode was placed as close as possible to the cathode to avoid Ohmic losses. N_2 gas was bubbled through the potassium hydroxide solution during 1 hour before the characterization procedure and during the characterization procedure itself. It was done to remove the excess of dissolved oxygen, hence, to avoid the reduction of the oxygen at the working electrode before the reduction of water to hydrogen gas.

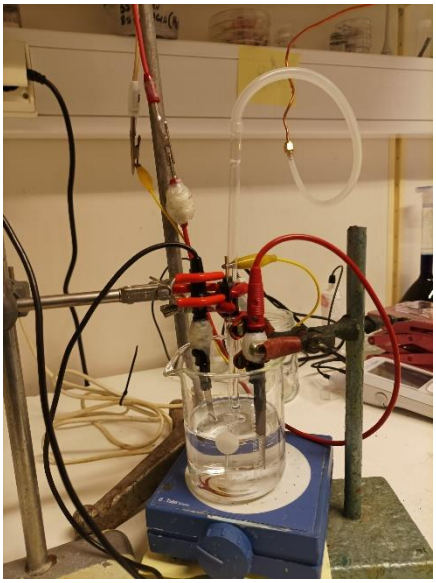

Figure 4.2: Electrolytic cell for LSV and EIS measurements of NiMo samples

The polarization curves were performed in the potential range from -0.9 V vs Hg/HgO of initial voltage to -1.35 V vs Hg/HgO of final voltage at a scan rate of 5 mV s^{-1} in 1 M KOH solution at the room temperature of approximately 25 °C. Several scans were done for each sample until an the current-voltage curves stabilized. After all the measurements are completed, all the measured potentials in this thesis were converted to reversible hydrogen electrode (RHE) using Equation (25):

$$E_{RHE} = E_{measured\ vs\ Hg/HgO} + E_{Hg/HgO\ vs\ SCE} + E^{\circ}{}_{SCE} + 0.0591pH \quad (25)$$

where the $E_{measured\ vs\ Hg/HgO}$ is the measured potential against Hg/HgO electrode in V, recorded by Parstat 2273 potentiostat, $E_{Hg/HgO\ vs\ SCE}$ is the potential of Hg/HgO(1M NaOH) reference electrode measured against saturated calomel electrode (SCE) that is equal to -0.108 V, $E^{\circ}{}_{SCE}$ is standard electrode potential of SCE that is equal to 0.241 V, and pH is the pH value of electrolyte used for the investigation. After the conversion, the data was averaged for each time etching group and for all polished samples. The LSV curves were used to extract kinetic parameters such as Tafel slopes and exchange current densities as described in **Appendix C**.

The electrochemical impedance spectroscopy measurements were performed after obtaining the LSV curves. The EIS experiments were done in three modes: at -1 mA cm^{-2}, at -10 mA cm^{-2}, and at -1 V. The EIS data were collected at the frequency range of 100 kHz – 0.1 Hz with a 10 mV rms amplitude and 10 points/decades. DC potential parameter for two current density modes was directly read from the corresponding LSV curve at – 1mA cm^{-2} and – 10 mA cm^{-2} for each sample. The recorded EIS data were fitted in CPE-R_p model with the ZView software and averaged for each time etching group and for all

polished samples. The ZView was also used to obtain charge-transfer resistance values from the fitted models with subsequent averaging of these values.

4.5. Morphological, compositional and structural characterization of NiMo

The surface morphology and the microstructure of NiMo alloy were characterized by scanning electron microscopy (SEM, The Quanta FEG 200, USA), equipped with EDS. The NiMo samples were prepared for SEM imaging by fixing the specimens on a sample holder with carbon tape. The Quanta FEG 200 in high vacuum condition and the SEM images were captured by accelerated electrons at 20 kV or 30 kV energy, depending on what voltage could give the best resolution for a particular image. EDS was applied to the samples in the SEM chamber at 20 kV for collecting numerical data about the composition of the samples.

The X-ray diffraction (XRD) was conducted using a Rigaku diffractometer (RTokyo, Japan) with a 40 kV electric potential for accelerating X-rays towards anode and working current of 15 mA. Goniometer radius was 150 mm and two slits were chosen as D.S. slit of 0.625° and 2IHS slit. Scanning speed was 5°/min with 2θ step of 0.02°. The measurements were done in range of 10° to 90° for 2θ. All extracted data were analyzed using DIFFRAC.EVA and Crystallographic Open Database (COD). In case of both XRD and SEM with EDS, only a sample that appeared visually the most coated was chosen for the investigation from each of five pretreatment groups(1s, 2 s, 3 s, 4 s etched and polished).

5. Results

In this section, the experimentally obtained results are presented. First, the results of electrodeposition of NiMo alloy film on Ti substrate as synthesis method are demonstrated to have a closer view on this process. Afterwards, the results generated by XRD and SEM with EDS before and after electrocatalytic characterization are described. The last part of the results is the one that have been extracted from LSV and EIS. All this results form basis for the following discussion structural and morphological information about the synthesized NiMo electrocatalyst.

5.1. Synthesis of NiMo alloy

The averaged curves produced by chronopotentiometry for NiMo alloy samples (in triplicate for four etched groups and in 12 samples for the polished group) are exhibited in **Figure 5.1**.

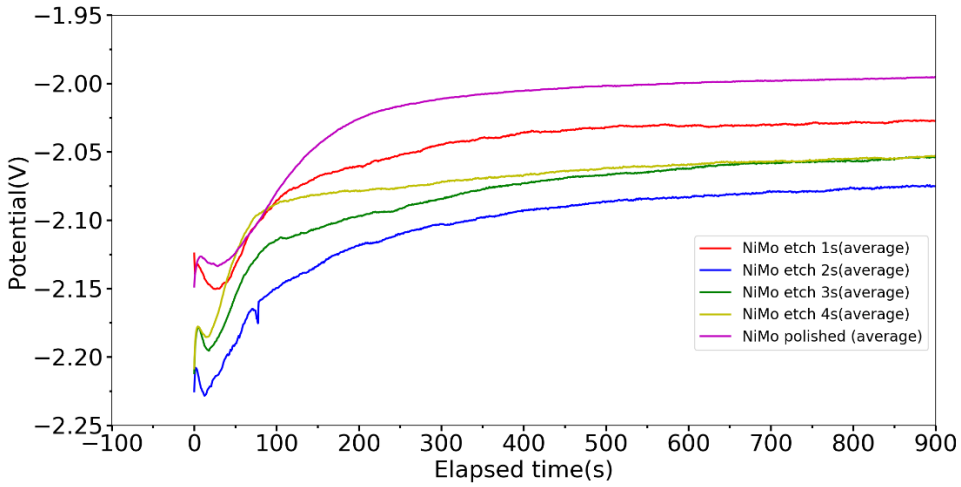

Figure 5.1: Chronopotentiometry for NiMo samples averaged for each pre-treatment group at -20 mA cm^{-2} and 15 min

This figure presents the variation in the potential at the working electrodes, Ti substrate, with deposition time. The figure clearly demonstrates that all the samples have two regions, namely the transition region (from 0 to approximately 150 s) and the stability region (from approximately 150 to 900 s). The transition region indicates an actual nucleation of the material on the surface of Ti substrates. The stability region corresponds to the time region where the considerable amount of the NiMo bimetallic alloy has been deposited to maintain a relatively stable potential over the rest of the deposition time.

Five (four etched and one polished) groups of samples have shown the stability regions at different potential values. At the same time, the stabilization potentials for each average curve are quite different with exception of two average group samples, those with Ti substrates etched at 3 s and at 4 s, that converge to the same value of potential

(approximately -2.06 V) after 600 s. **Figure 5.1** clearly shows that the polishing deposition is happening at lower potentials. This means that the deposition current requires lower voltage, and therefore is achieved easier, thus making the conclusion that the substrate is more conducting. Therefore, these results should be considered in pairs with the ones of the electrochemical performance.

5.2. Physicochemical characterization

5.2.1. SEM and EDS characterization

To establish a baseline for the morphological investigations, the untreated Ti foil substrate as well as the Ti substates exposed to mechanical polishing and etching have been investigated by SEM as presented in **Figure 5.2**. The untreated Ti foil clearly exhibits the rough and non-homogeneous surface with the considerable number of scratches and cracks with the approximate size of 1 – 6 μm. Moreover, due to the nature of the titanium chemistry, Ti substrate is expected to have an oxide layer on its surface. The surface morphology of the polished Ti substrate presented in Figure 5.2b) looks similar to the untreated one with the scratches and cracks to have noticeable width of approximately 1 – 3.5 μm.

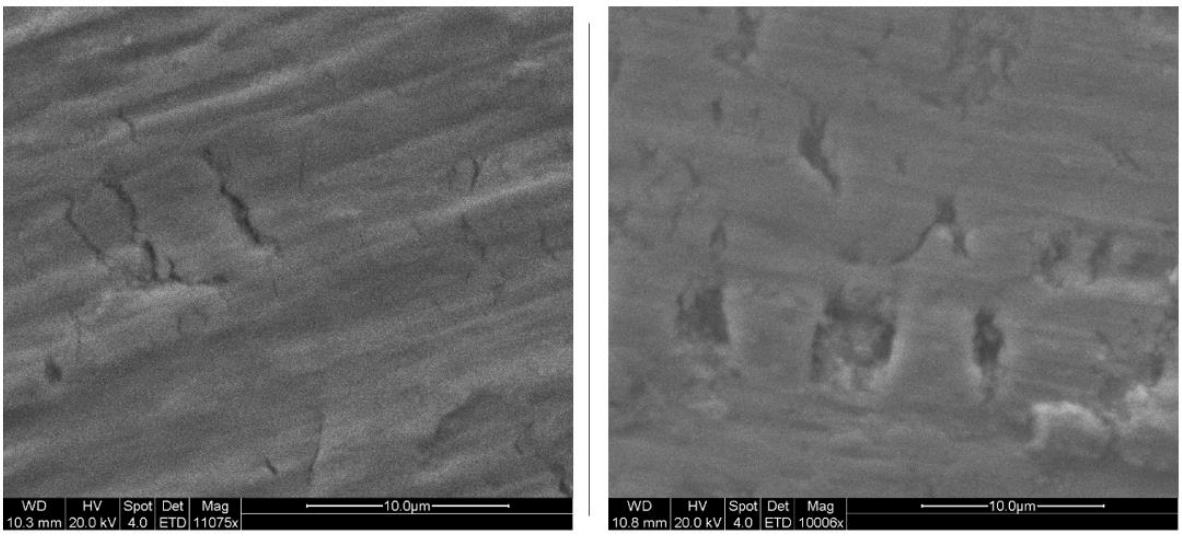

a) untreated Ti substrate

b) polished Ti substrate

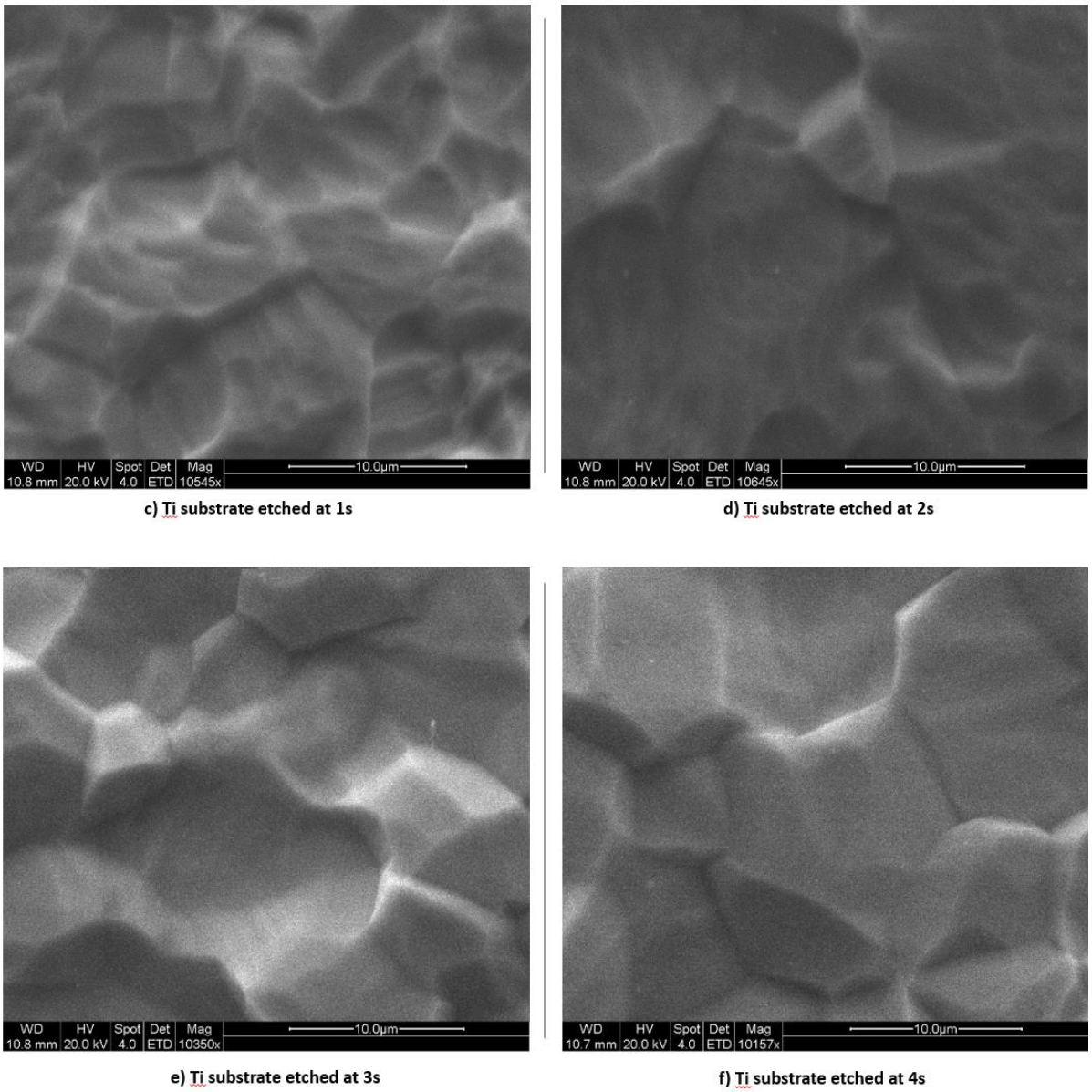

Figure 5.2: SEM images of untreated, polished and etched Ti substrates

SEM images of the etched Ti substrates are shown in **Figure 5.2c-f**. The etching time affects the surface morphology as well. The substrates exposed to longer etching time (3-4s) appear to be smoother with larger average grain-like protrusions (in the range of 5 – 15 µm) than those that have been etched at shorter time spans (with 1 – 10 µm size of grans).

To investigate the morphology of the produced samples, NiMo alloys synthesized on etched and polished substrates have been investigated by SEM as shown in **Figure 5.3**.

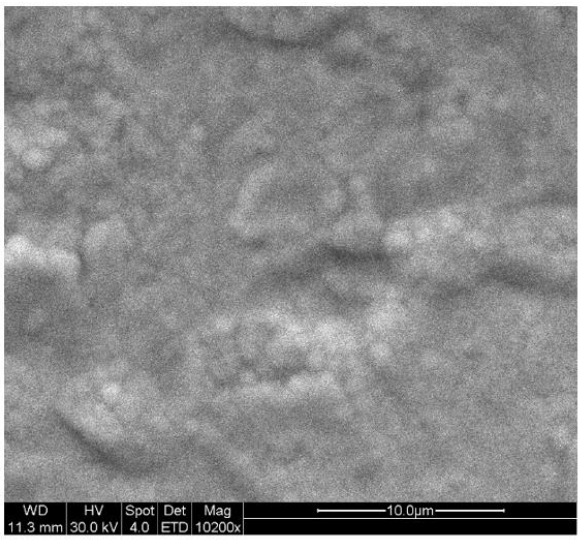

a) Ti substrate etched at 1s

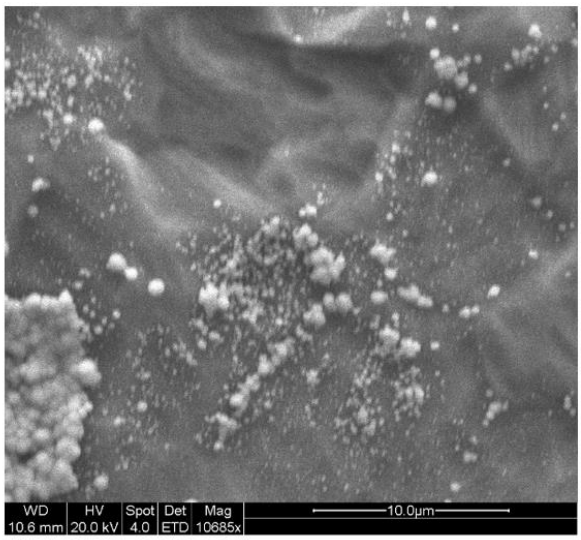

b) Ti substrate etched at 2s

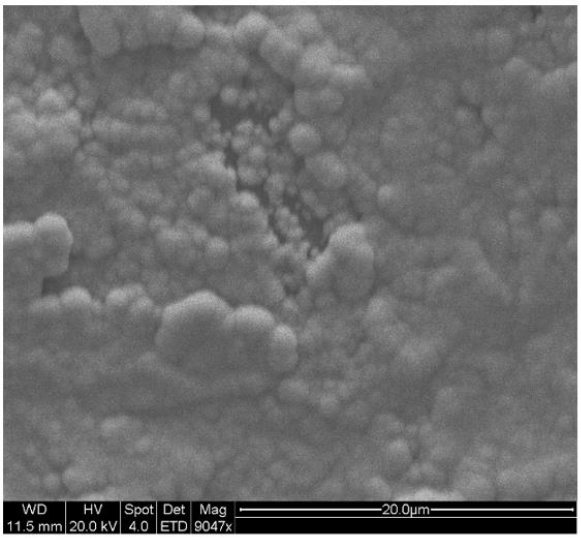

c) Ti substrate etched at 3s

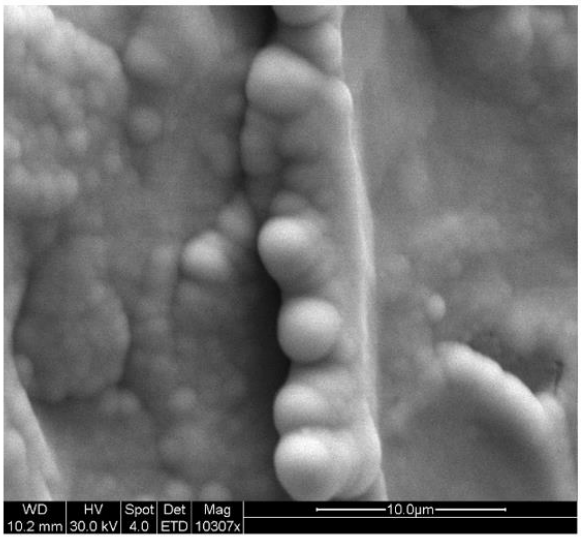

d) Ti substrate etched at 4s

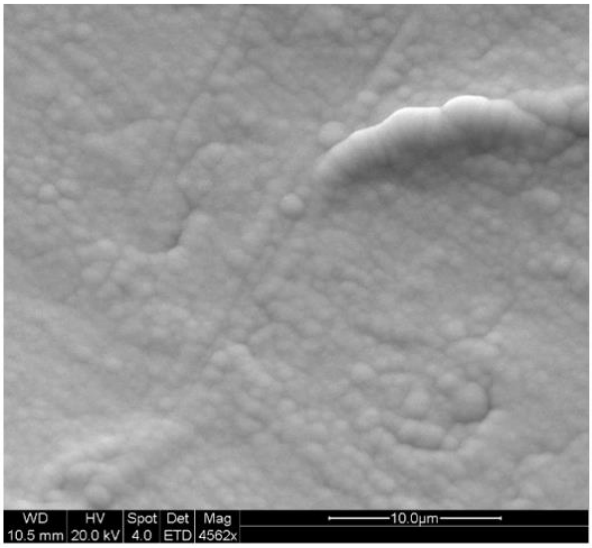

e) Polished Ti substrate

Figure 5.3: SEM image of electrodeposited NiMo on etched and polished Ti substrates

SEM images of the electrodeposited NiMo alloy coatings on the etched Ti substrates are presented in **Figure 5.3a-d)**. The sample etched at 1 s has a structure characterized by the spherical particles that are agglomerated together as various protrusions of 1 – 2 μm size. The Ti substrate samples etched at 3 s and 4 s demonstrate the similar morphology but with larger agglomerated particles with the average size 1.5 – 3 μm and 3 – 4.5 μm, respectively. A significantly different morphology is obtained for the sample with the substrate etched at 2 s. Its surface appears to be partially coated by the clusters of particles of approximate size of 0.1 – 1 μm. The uncoated regions have the grain-like formations similar to the uncoated etched Ti substrate.

The morphology of the electrodeposited NiMo alloy on the polished Ti substrate is seen in **Figure 5.3e)**. Its surface contains a layer of the densely packed agglomerated particles with an average size of 0.5 – 2.5 μm, and has the most? smooth and homogeneous surface without many significant protrusions of the samples.

5.2.2. EDS characterization

The chemical analysis of NiMo alloys electrodeposited on the etched and polished Ti substrates has been conducted by EDS applying area analysis. The EDS spectrum analysis of the untreated Ti substrate shown in Figure 5.4a) reveals only the presence of Ti and N in the amounts of 77.7 at% and 22.3 at%, respectively. EDS analysis of Ti substrates etched for 1-4 s as exhibited in **Figure 5.4 c-f)** also shows only presence of N and Ti in amounts of 23.7 at% and 76.3 at%; 22.2 at% and 77.8 at%; 21.9 at% and 78.1 at%; 6.5 at% and 93.5 at% for 1 s, 2 s, 3 s, 4 s of etching time, respectively. Moreover, EDS of the polished Ti substrate in **Figure 5.4b)** indicates the presence of some amount of carbon (13.6 at%) in addition to N (17.3 at%) and Ti (69.1at%).

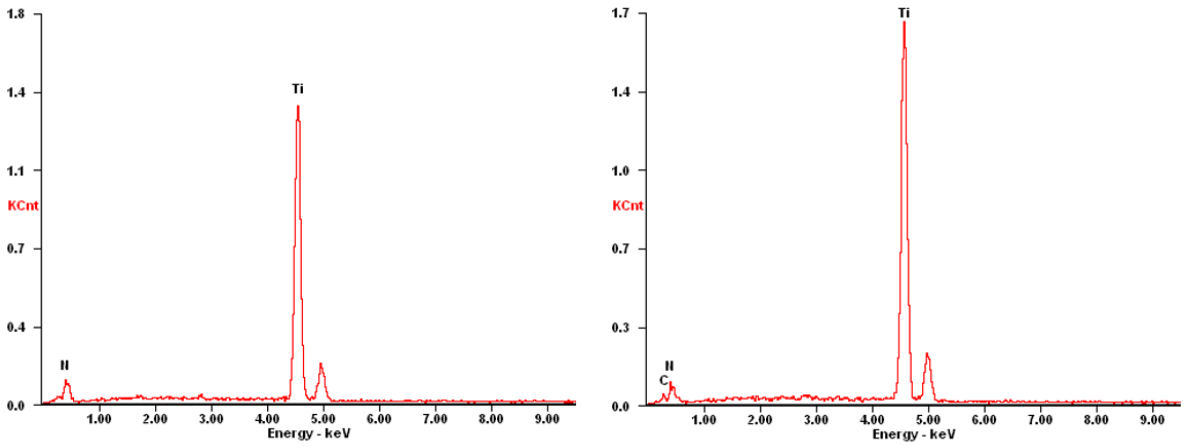

a) untreated Ti substrate

b) polished Ti substrate

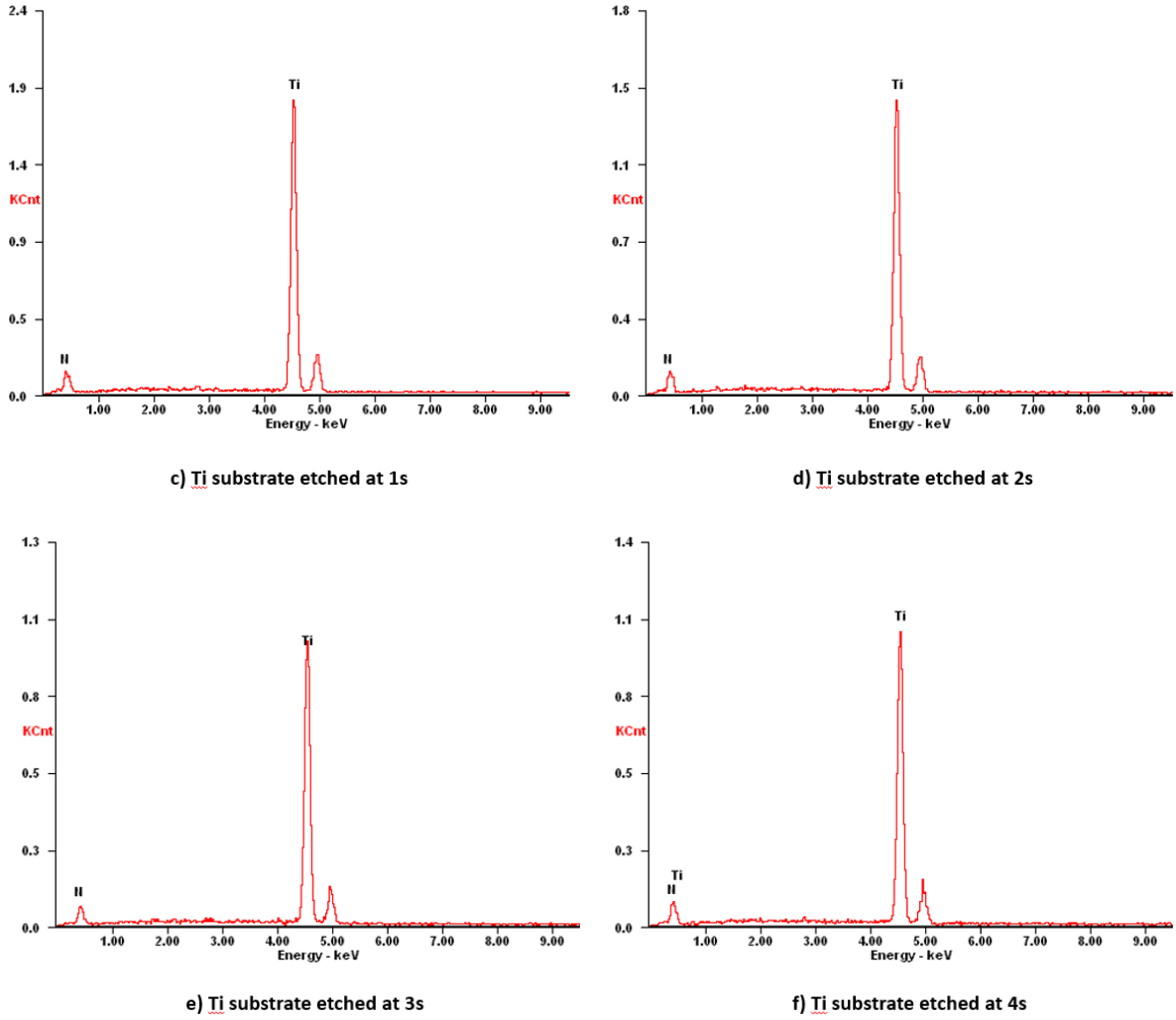

Figure 5.4: EDS for untreated, polished and etched Ti substrates

In **Figure 5.5a-d)**, EDS spectrums demonstrate that the NiMo samples with substrates etched for 1-4 s have Ni content in the amount of 74.2 at%, 8.3 at%, 70.9 at%, and 61.2% for samples with the etched substates for 1 s, 2 s, 3 s, and 4 s, respectively. The pretreatment method as well as the etching time has strongly affected/ influenced the molybdenum content in these deposits. From Figure 5.5, the etching time increase from 1 s to 4 s indicated the rise in the molybdenum content in the deposits from 11.3 at% to 16.3 at% (with exception of 2s etching time that has demonstrated exceptionally low Mo content of 0.5 at%). It leads to the following atomic ratios of Ni:Mo in each case: 6.6:1, 16.6:1, 4.6:1, and 3.8:1 for 1, 2, 3 and 4 s etched substrate, respectively. The other elements detected are O (11.8 at% for 1 s etched substrate sample, 10.7 at% for 3 s etched substrate sample, and 22.5 at % for 4 s etched substrate sample) and Ti (2.7at% for 1 s etched substrate sample, 90.3 at% for 2 s etched substrate sample, and 2.9 at % for 3 s etched substrate sample) and S (0.9 at% for the sample with 2 s etched substrate)

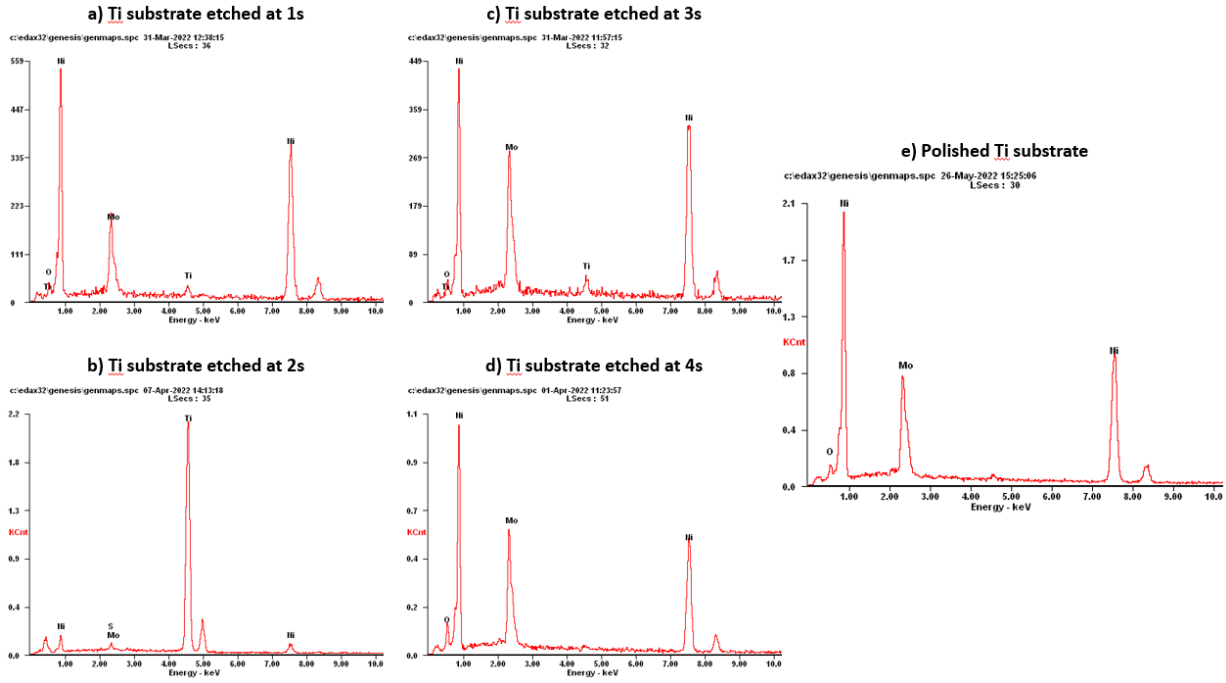

Figure 5.5: EDS for electrodeposited NiMo alloys on etched and polished Ti substrates

Figure 5.5e) exhibits the composition of the NiMo sample electrodeposited on the polished Ni substrate in the ratio of Ni (63.9 at%), Mo (16.3 at %), and O (19.8 at %) that indicates 3.9:1 of Ni:Mo atomic ratio.

5.2.3. XRD characterization

X-ray powder diffraction (XRD) technique has been employed to determine the crystalline phases exhibited in the electrodeposited NiMo coatings as well as their crystallite size on the etched and polished Ti substrates. **Figure 5.6** exhibits the peaks for all the NiMo samples that have almost the same position as for Ti peaks, but of considerably different intensities. This can be clearly seen by comparing the obtained peaks at 35°, 38°, 63° and 70° that are close to the Ti peaks from **Figure B.1** in **Appendix B**.

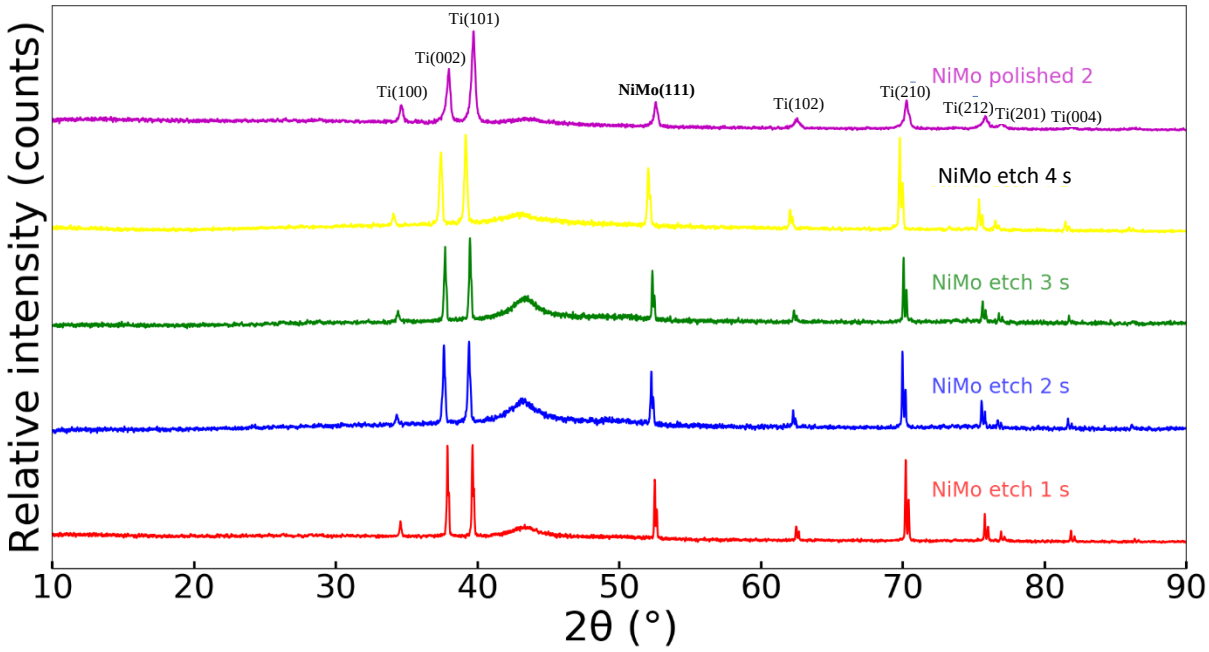

Figure 5.6: XRD for electrodeposited NiMo samples on etched and polished Ti substrates

Moreover, **Figure 5.6** demonstrates one common peak for all the electrodeposited NiMo coating samples at a position range of 42 – 44 ° that appears to be broad and stands out from other observed peaks.This broad characteristic diffraction peak is most likely to be a peak for face-centered cubic NiMo of crystalline plane (111)[87,89,113]. However, other peaks corresponded to Ni, Mo or their alloy compounds have not been observed.

5.3. Electrocatalytic characterization

5.3.1. LSV characterization

Figure 5.7 presents the averaged LSV curves for the NiMo coating samples electrodeposited on the etched and polished substrates. The figure clearly indicates that the NiMo sample deposited on the polished Ti substrate shows the superior electrochemical performance demonstrating the highest current density value of approximately -77 mA cm^{-2} at -0.35 V vs RHE among all the samples produced by two pretreatment methods. It fits well with with SEM morphology as well as low deposition curves.

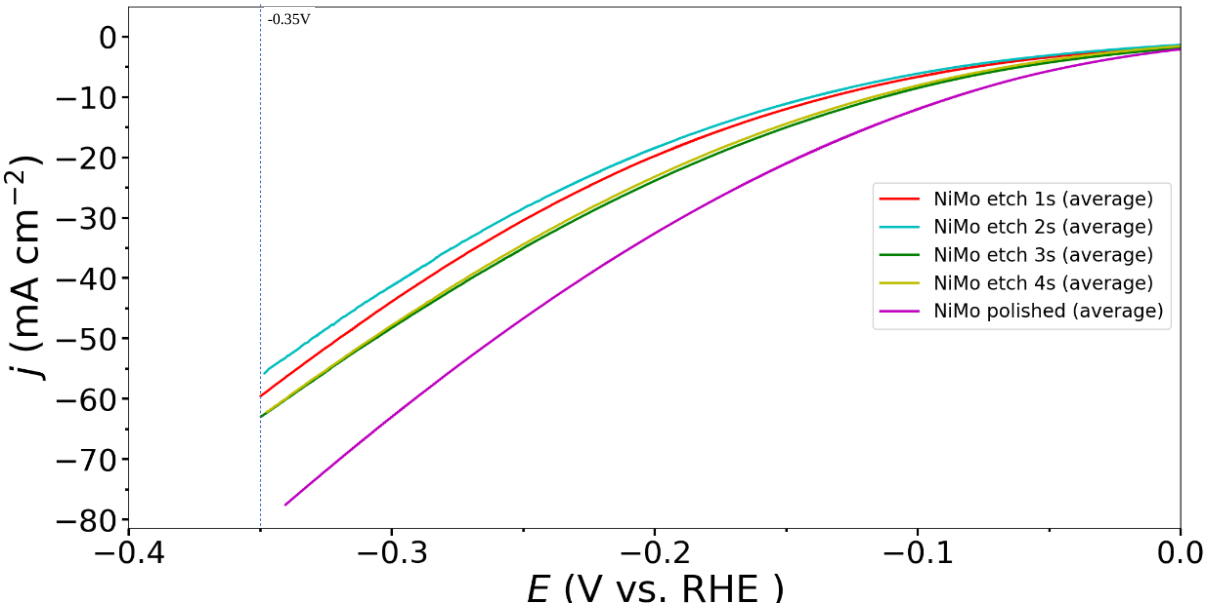

Figure 5.7: Averaged LSV curves for electrodeposited NiMo samples on etched and polished Ti substrates

The NiMo samples electrodeposited on the etched Ti substrate at 3-4 seconds have exhibited the same current density value of approximately -64 mA cm^{-2} at -0.35 V vs RHE that is the next best result obtained in this investigation. It should be noted that the samples with 3 s and 4 s etched substrates converge to the same value of the current density at the end value of potential and exhibit similar deposition curves.

Table 5.1 and **Figure 5.8** present the extracted kinetic parameters and Tafel slope plots for the averaged electrodeposited NiMo samples the on etched and polished Ti substrates, respectively. The extraction of the parameters can be found in **Appendix C**. The extracted parameters and Tafel slopes plots support the above-mentioned observations that the averaged polished substrate sample has the lowest Tafel slope and the highest current density. According to obtained Tafel slopes, a reaction mechanism for HER for each group of samples is the same: Volmer-Heyrovsky mechanism with Volmer step as RDS.

Sample type and number	**Tafel slope**, b [mV dec^{-1}]	**Exchange current density**, j_0[mA cm^{-2}]
Etched for 1 s	123.6	-1.82
Etched for 2 s	141.6	-1.66
Etched for 3s	108.7	-1.91
Etched for 4 s	96.0	-1.95
Polished	80.7	-2.45

Table 5.1: Extracted Tafel slopes and exchange current densities for averaged electrodeposited NiMo samples on both etched and polished Ti substrates

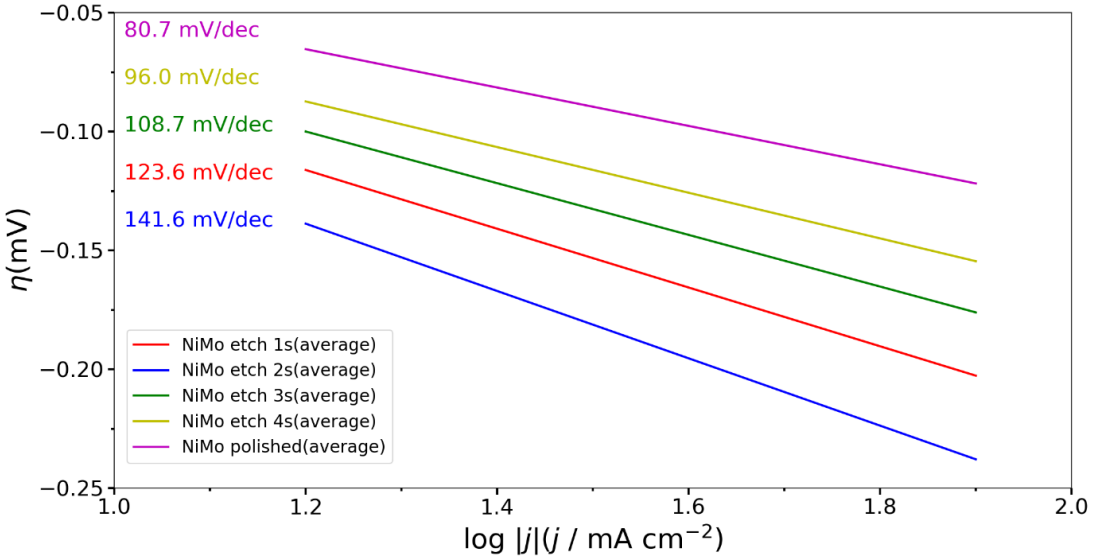

Figure 5.8: Tafel slope plots for averaged electrodeposited NiMo samples on etched and polished Ti substrates

5.3.2. EIS characterization

The results of EIS characterization as Nyquist plots are presented in **Figure 5.9**.

a)

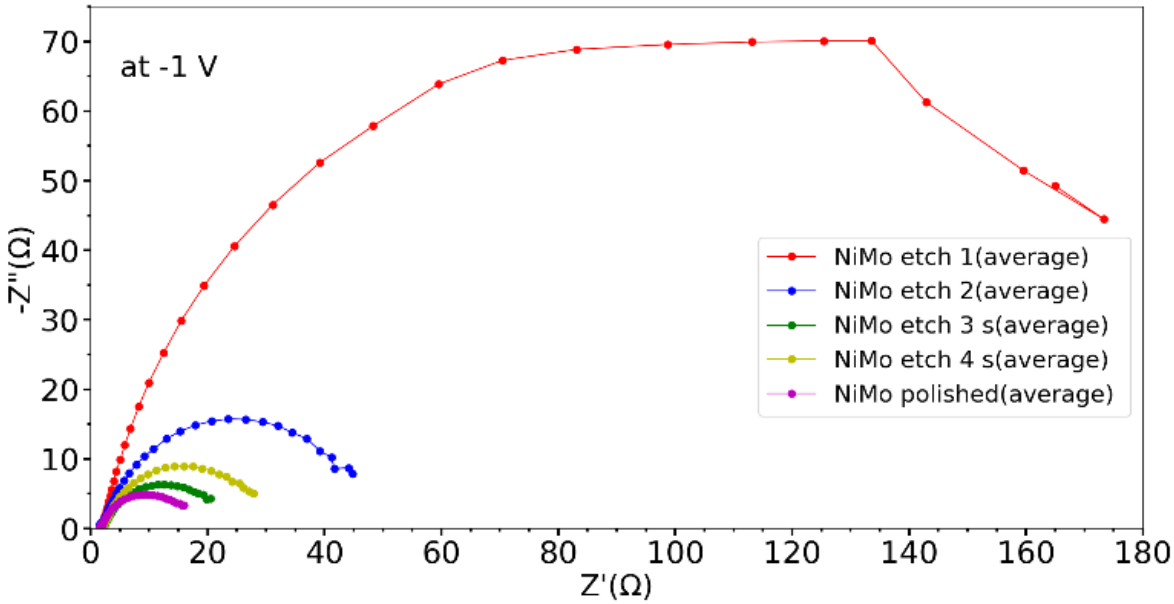

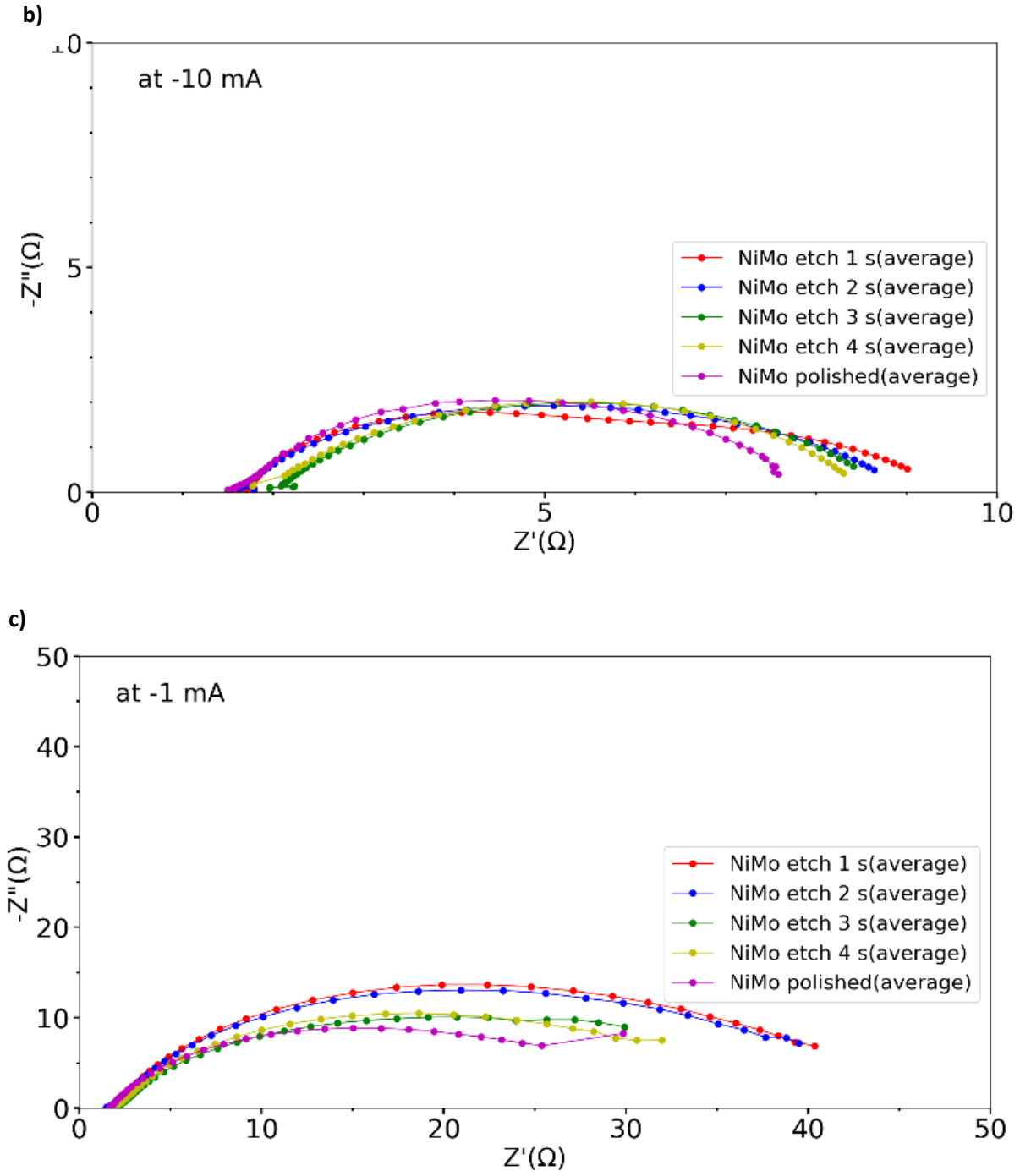

Figure 5.9: Averaged EIS for the electrodeposited NiMo samples on etched and polished Ti substrates at -1 V vs RHE (a), at -10 mA cm-2(b), and at -1 mA cm-2(c)

The EIS curves are expected to increase in size (values of both imaginary and real Z become larger) with decreasing electrocatalytic activity (increase in value of Tafel slopes, decrease in values of exchange current densities, and bending of LSV curves to the left as observed in **Table 5.1** and **Figures 5.7** and **5.8**) at a current density for which measurements were taken. This alternatively can be seen in **Table 5.2**, **Table 5.3** and

Table 5.4, where the charge-transfer resistances decrease with the increase in the electrocatalytic activity of the NiMo samples electrodeposited on etched and polished Ti substrates.

Sample type and number	Charge-transfer resistance, R_{ct}(Ω)
Etched for 1s	44.27
Etched for 2s	43.21
Etched for 3s	35.49
Etched for 4s	34.43
Polished	37.60

Table 5.2: Charge-transfer resistance for the averaged electrodeposited NiMo samples on both etched and polished Ti substrates at -1 mA cm-2

Sample type and number	Charge-transfer resistance, R_{ct}(Ω)
Etched for 1s	7.79
Etched for 2s	7.42
Etched for 3s	6.81
Etched for 4s	6.61
Polished	6.66

Table 5.3: Charge-transfer resistance for the averaged electrodeposited NiMo samples on both etched and polished Ti substrates at -10 mA

Sample type and number	Charge-transfer resistance, R_{ct}(Ω)
Etched for 1s	196.37
Etched for 2s	51.36
Etched for 3s	22.23
Etched for 4s	29.61
Polished	17.97

Table 5.4: Charge-transfer resistance for the averaged electrodeposited NiMo samples on both etched and polished Ti substrates at -1V

6. Discussion

6.1. Surface morphology

Topographical investigations by top-view scanning electron microscopy (SEM) of the synthesized samples of NiMo alloy on the etched and polished Ti substrates at room temperature of about 20 °C provide information regarding the morphology of NiMo coatings after the electrodeposition process. The top-view SEM images in **Figure 5.3** demonstrate that the NiMo samples consist of particles that are completely different in size. The NiMo coatings electrodeposited on the etched Ti substrates possess a relatively rough, non-homogeneous surface where the considerable number of agglomerated particles with the approximate size in the range of 0.1 – 4.5 μm are observed as depicted on the SEM images. Such changes in morphology of NiMo/etched Ti substrate are similar to those of the pure etched Ti substrates (i.e., without electrodeposited NiMo coatings) that have demonstrated growing grains at the increasing etching time.

On the contrary, the pure polished Ti foil substrate (i.e., without electrodeposited NiMo coatings) appears to demonstrate the smoother and more homogeneous surface without many significant protrusions compared to the etched ones, but with noticeable cracks. As a consequence, the NiMo coating on the polished Ti substrate appeared to be smoother with finer agglomerated particles. The above presented results on the NiMo morphology on the etched and polished Ti substrates are in line with various reports of NiMo coatings obtained via electrodeposition[21,129,139].

The only one sample that stand out in this investigation is the NiMo electrodeposited on the 2 s etched Ti foil. **Figure 5.3b)** clearly demonstrates that its surface only partially covered by NiMo coating. One of the possible reasons for it is that some of the NiMo coating has been lost after the synthesis procedure. It might indicate that NiMo particles were not bonded strongly enough to the surface the Ti substrate.

X-ray diffraction (XRD) has been employed to identify the crystal structure and the type of presented phases, while the chemical elemental composition of the NiMo coatings is determined by energy-dispersive X-ray spectroscopy (EDS).

Figure 5.6 displays the XRD patterns of NiMo coatings obtained under the different pretreatment methods. X-ray diffraction (XRD) patterns for all the layers deposited at both etched and polished Ti substrates have displayed one common peak positioned at 2θ angle of 42 – 44 ° that according to the literature [125,137,140] corresponds to the (111) crystalline plane of broad characteristic diffraction peak for the face-centered cubic

structure of NiMo alloy [141,142]. However, other peaks related to Ni, Mo or their alloy compounds have not been observed as it was stated earlier.

The NiMo samples with lower Mo content have exhibited the sharpened and less broadened peaks of NiMo(111) on the obtained XRD patterns. This can be partially explained by a change in atomic positions of Ni and Mo at different at% that leads to a change in the peak's intensity. With the increased Mo content in the deposited NiMo layers the peaks are getting much flatter, wider and smaller in height as exhibited in NiMo samples electrodeposited on the polished Ti foil as revealed by EDS in **Figure 5.5**. The broad peak definitely indicates that the NiMo phase is present but doesn't exclude other phases or phases with amorphous structures. As a support for this claim, the varied obtained atomic ratios of Ni:Mo samples point out on possible presence of different NiMo phases in each case. As result, XRD analysis based on EVA alone cannot provide precise identification of phases, more detailed analysis for phase identification based on larger set of collected data with higher precision is needed.

The EDS analysis also confirmed that every group of samples had both Ni and Mo content. The obtained atomic ratio of Ni and Mo for the NiMo samples with the polished Ti substrate and with 4 s etched Ti substrate approximates to 4:1. Moreover, an increasing of molybdenum content with increase in etching time were observed. A maximum for molybdenum content was reached in the NiMo samples with the polished Ti substrate and with 4 s etched Ti substrate. This observation can be explained by the assumption that the longest etching time and polishing favor the formation of Mo reach phase. However, due to the absence of sample groups in a wider etching time range, this explanation needs a support by additional experimental data.

Also, the high Mo content (16.6 at%) obtained for NiMo sample on the polished Ti substrates, and the lowest Mo content of 0.5 at% for 2 s etched Ti substate are consistent with Chassaing et al. [67,143]. In addition, a formation of distinctly refined and densely agglomerated particles for the NiMo sample with polished Ti substrate and large spherical particles for the NiMo sample with 4 s etched Ti substrate are consistent with the results reported by Nee et al. [137], who have indicated that in the NiMo deposits the size of grains is directly associated with their composition.

The emergence of O element in almost all investigated samples is probably attributed to the oxidation of the NiMo alloy's surface in air after completion of the synthesis process[144]. Other elements such as S and N were detected in the NiMo sample with 2 etched and in the most of etched Ti substrates. That can be explained by contamination from environment or by the fact that EDS is not so appropriate in detection of the light

elements in correct amounts or could identify light elements wrongly by overlapping it with other light elements such as oxygen.

The main sources of errors and uncertainties in above-discussed analysis are likelihood of shedding of NiMo coatings and the fact that only one sample from a group served as representative for whole group.

6.2. Electrocatalytic performance

Electrochemical impedance spectroscopy (EIS) has been carried out to further assess the HER kinetics on various electrodes and to measure the charge-transfer resistances (Rct) of the NiMo alloys at fixed end potential of -0.35 V vs RHE (**Figure 5.7**). EIS analysis of the NiMo alloys electrodeposited on the polished and etched Ti substrates shows that the variance in their performance is also attributable to the differences in the charge transfer resistance (Rct) as an indicator of the ease of charge transfer during electrocatalytic process.

Over the given potential range for the NiMo/Ti foil electrode, all the impedance spectroscopy curves can be fitted by applying different capacitance model that results in specific Nyquist plots. As depicted in **Figure 5.9**, the shapes of Nyquist plots of all the analysed samples are similar at -1 and -10mA current densities as well as at potential of -1V, but their sizes are considerably different. As the radius of the semicircle is associated with the charge-transfer resistance at the coating interface, the NiMo alloys electrodeposited on the polished as well as 3s- and 4s-etched Ti electrodes demonstrate lower values of Rct than other Ti substrates. It confirms that these electrodes require lower energy input for the effective HER which is also? reflected by LSV curves from **Figure 5.7**. The deviation from the perfect semicircle for 1 second-etched substrate, as depicted in **Figure 5.9a),** is related to the surface inhomogeneities of the NiMo coatings[7]. This observation is partially supported by SEM image of this sample in **Figure5.3a)**

The best catalytic activity among all the studied electrodes for the HER has been analysed from **Tables 5.2-5.4** and the Nyquist plots. The lowest values of the charge transfer resistance (Rct) appears to be at -10 mA. They exhibit that at this current density, the NiMo alloy has been more effective that results in more rapid electron transfer under HER process thus leading to superior performance.

The NiMo/4s-etched Ti substrate exhibits quite low Rct value of 6.61 Ω at -10 mA which slightly lower than 6.66 Ω for the polished NiMo alloy sample and a little bit lower than for NiMo/3s etched Ti substrate, supporting more efficient reaction kinetics of the two best samples. At the current density of -1 mA NiMo the 4s etched Ti substrate again displays

the lowest Rct value among all the samples at 34.43 Ω, followed by the samples etched for 3 s and the polished one. At -1V the polished sample with 17.97 Ω appears to be the best.

The current density is strongly determined by the electrode's intrinsic surface area. Derived from Tafel plots, the exchange current densities, j_0, for the HER on the investigated NiMo sample electrodes are presented in **Table 5.1**. The NiMo alloy on the polished Ti foil substrates exhibit the largest j_0 (2.45 $mAcm^{-2}$) among all the NiMo alloy samples. Its superior electrocatalytic activity compared to the other transition group metals as reported by I.A. Raj and K.I. Vasu[86] (who ranked the electrocatalytic effects in order: Ni-Mo > Ni-Zn > Ni-Co > Ni-W > Ni-Fe > Ni-Cr > Ni plated steel) is likely attributed to the high surface area of its topology that allows a lot of highly available reactive sites, and to the enhanced HER kinetics due to the synergistic effect between Ni and Mo atoms[45]. This is supported by **Figure 5.3e)** where the surface consisting of homogeneous layer of fine agglomerated particles is observed for this sample. Also, this result suggests that NiMo alloys on the polished Ti foil substrates has the highest activity among all the five analysed NiMo samples for the HER. Important to note that from the obtained data, all the sample groups have the same reaction mechanisms and RDS. Despite the similar reaction mechanisms, the sample groups have apparently different electrocatalytic activity. This fact can be explained by different values of the charge transfer resistances observed among the five investigated group of samples (4 etched and 1 polished) and, hence, by the difference in easiness of the charged species' transfer.

The key factors behind the increase in the NiMo alloys' electrochemical activity for HER is the increase of the active surface area and the rise in Mo content. The research works performed by Nee et al. [137], Arul Raj and Venkatesan [134] and Divisek et al. [138], have demonstrated the similar behaviour of NiMo alloys prepared by different methods, and thus support the above statement.

The investigation has confirmed that the NiMo alloy electrodeposited on the polished Ti substrates (containing 16.6 at% Mo) has the lowest Tafel slope for Tafel region (80.7 mV/dec) as well as the highest current density (2.45 mA cm^{-2}) at – 0.35 V vs RHE. From EDS analysis the obtained Ni:Mo atomic ratio for the polished Ti substrate approximates 4:1. The presence of the primary Ni4Mo phase in the total composition of NiMo alloys has been observed by many different groups of researchers[33,86,87,113,114,119]. Therefore, the NiMo samples electrodeposited on the polished Ti substrates demonstrate the best electrocatalytic activity among all other groups of samples.

7. Conclusion

The best sample group in terms of the overall electrocatalytic performance appears to be the NiMo samples with polished Ti substrate group that has following characteristics: the lowest Tafel slope (80.7 mV dec^{-1}), highest exchange current density (-2.45 mA cm^{-2}), Volmer-Heyrovsky mechanism with Volmer step as Rate Determining Step (RDS) for HER, the composition of Ni(63.9 at%), Mo (16.3 at%), and O (19.8 at%), the atomic ratio of Ni:Mo as 3.9:1, and fine agglomerated particles that form homogeneous coverage on the Ti substrate. Hence, mechanical polishing has proved to be the best pretreatment method, and it is likely due to the specific morphology of the polished Ti substrates associated with the removed oxide layer, better surface conductivity, scratches, and cracks. As consequence, this might provide better surface chemistry between NiMo deposited coating and Ti substrate than the one between NiMo deposited coating and etched Ti substrates. Data from chronopotentiometry also showed that the NiMo on polished substrate sample group has the lowest potential, making the NiMo material easier to deposit and, as result, supporting the conclusion about the superior electrocatalytic performance of the NiMo with polished substrates. Moreover, all the groups of the NiMo samples have shown an intensity peak positioned at 42 – 44° in XRD pattern that corresponds to face-centered cubic NiMo(111) and the rest of the diffraction peaks is completely matched with the diffraction pattern of hexagonal Ti. Despite the fact that such observation was confirmed by several groups of researchers, the conformation of the observed phases requires a more detailed and quantitative phase analysis.

The most effective HER kinetics was observed in the NiMo deposited on 4 s etched Ti substrate group by EIS characterization at -10 mA cm^{-2}. This group has the lowest value of R_{ct}, 6.61 Ω which appears to be not only the lowest value for this characterization current, but the lowest value among all three-characterization current/potentials in this investigation.

At the same time, the electrocatalytic activity seems to be strongly increasing with an increase in the active surface area and the rise in Mo content. This is confirmed by the simultaneous decreasing of nickel content and increasing of molybdenum content with increasing etching time and obtaining of the small-sized agglomerated particles in the polished substrate sample group. This, in turn, provides direct evidence that the electrocatalytic performance increases with the increase of etching time and by application of polishing. At the same time, the possible and most probable explanations for uncertainty in the results are the observed shedding of the NiMo thin layer and the fact that only one sample from each group was chosen as the model sample for the whole group.

From these results, it can be concluded that this work has achieved its aim of improving the electrocatalytic activity of NiMo electrodeposited on Ti foil substrates for HER in alkaline media, by applying chemical etching and mechanical polishing as two different substrate pretreatment methods.

8. Further work

In the last decades the numerous research have been dedicated to designing an innovative and highly efficient NiMo alloy with superior activity characteristics for effective hydrogen production. The most natural continuation of the work presented in this thesis is to further investigate NiMo electrocatalytic parameters with focus on complementary indicators like stability and efficiency. To evaluate the feasibility of NiMo alloy electrocatalyst for practical industrial applications the stability test like chronoamperometry must be performed. The information on the stability measurements must be available for the materials that demonstrate favourable properties that could be considered as the candidates for an industrial use. Analysing efficiency parameters like turnover frequency and Faradaic efficiency could further extend this work. Use of X-ray photoelectron spectroscopy can provide more information about oxidation states of Ni and Mo and hence give more info about NiMo composition. Theoretical tool such as Density Functional Theory calculations can also be applied to get deeper insight into HER mechanism for NiMo.

As only one substrate has been used in this research work the application of various substrates with different porosities and conductivities such as foil, foam, carbon cloth, to name a few, would make this research even more interesting. Other pretreatment methods such as ultrasonic cleaning and heat annealing can be tried. The type of the substrate is very important as it may influence both the initial growth conditions and the final charge transfer in the catalyst system as a whole. To further enhance this investigation conducting experiments by varying most popular parameters like current densities, pH value, electrodeposition time will make the experimental part even more compelling. Diverse synthesis techniques especially those that require higher synthesis temperatures could further enhance this investigation project. To make the investigation even more sophisticated it is worth to take a challenge by trying to improve NiMo alloys' electrocatalytic performance via design of the dimensional architectures (0 – 3D), porous structuring, facet engineering, phase engineering, interface engineering, component regulation[27,88,108].

References

[1] M.H.Rashid. Electric Renewable Energy Systems. Academic Press, 2016.

[2] International Energy Agency. Global Hydrogen Review 2021.

[3] N.P. Brandon and Z. Kurban. Clean energy and the hydrogen economy. Philosophical transactions of the Royal Society of London. Series A: Mathematical, physical, and engineering sciences, 375(2098):20160400{20160400, 2017.

[4] McKone, J. R., Marinescu, S. C., Brunschwig, B. S., Winkler, J. R. & Gray, H. B. Earth-abundant hydrogen evolution electrocatalysts. Chem. Sci. 5, 865–878 (2014).

[5] Safizadeh, F., Ghali, E. & Houlachi, G. Electrocatalysis developments for hydrogen evolution reaction in alkaline solutions – a review. Int. J. Hydrog. Energy 40, 256–274 (2015).

[6] International Energy Agency. Net Zero by 2050 A Roadmap for the Global Energy Sector.

[7] Suraj Gupta,Nainesh Patel,Antonio Miotello,D.C. Kothari Cobalt-Boride: An efficient and robust electrocatalyst for Hydrogen Evolution Reaction J. Power Sources 285 (2015) 169 – 177.

[8] A.R. Zeradjanin, J.P. Grote, G. Polymeros, K.J.J. Mayrhofer, A critical review on hydrogen evolution electrocatalysis: Re-exploring the volcano-relationship, Electroanalysis 28 (2016) 2256 – 2269, https://doi.org/10.1002/elan.201600270.

[9] P. Quaino, F. Juarez, E. Santos, W. Schmickler, Volcano plots in hydrogen electrocatalysis e uses and abuses, Beilstein J. Nanotechnol. 5 (2014) 846e854, https://doi.org/10.3762/bjnano.5.96.

[10] J. Norskov, T. Bligaard, A. Logadottir, J.R. Kitchin, J.G. Chen, S. Pandelov, et al., Trends in the exchange current for hydrogen evolution, J. Electrochem. Soc. 152 (2005) J23eJ26, https://doi.org/10.1149/1.1856988.

[11] X. Han, F. Cheng, T. Zhang, J. Yang, Y. Hu, and J. Chen. Hydrogenated Uniform Pt Clusters Supported on Porous CaMnO3 as a Bifunctional Electrocatalyst for Enhanced Oxygen Reduction and Evolution. Advanced Materials, 26(13):2047{2051, 2014.

[12] Z. Fan, Z.and Luo, X. Huang, B. Li, Y. Chen, J. Wang, Y. Hu, and H. Zhang. Synthesis of 4H/fcc Noble Multimetallic Nanoribbons for Electrocatalytic Hydrogen Evolution Reaction. Journal of the American Chemical Society, 138(4):1414-1419, 2016.

[13] X. Cheng, Y. Li, L. Zheng, Y. Yan, Y. Zhang, G. Chen, S. Sun, and J. Zhang. Highly active, stable oxidized platinum clusters as electrocatalysts for the hydrogen evolution reaction. Energy Environ. Sci., 10:2450-2458, 2017.

[14] Carmo, M., Fritz, D. L., Mergel, J. & Stolten, D. A comprehensive review on PEM water electrolysis. Int. J. Hydrog. Energy 38, 4901–4934 (2013).

[15] Zou, X. & Zhang, Y. Noble metal-free hydrogen evolution catalysts for water splitting. Chem. Soc. Rev. 44, 5148–5180 (2015).

[16] Zheng, Y., Jiao, Y., Jaroniec, M. & Qiao, S. Z. Advancing the electrochemistry of the hydrogen-evolution reaction through combining experiment and theory. Angew. Chem. Int. Ed. 54, 52–65 (2015).

[17] W.-F. Chen et al., "Hydrogen-Evolution Catalysts Based on Non-Noble Metal Nickel-Molybdenum Nitride Nanosheets," Angew. Chem. Int. Ed, vol. 51, no. 25, pp. 6131-6135, 2012, doi: 10.1002/anie.201200699.

[18] W. F. Chen, K. Sasaki, C. Ma, A. I. Frenkel, N. Marinkovic, J. T. Muckerman, Y. Zhu, R. R. Adzic, Angew. Chem. Hydrogen-evolution catalysts based on non-noble metal nickel-molybdenum nitride nanosheets. Int. Ed. 2012, 51, 6131-6135; Angew. Chem. 2012, 124, 6235-6239.

[19] E. J. Popczun, J. R. McKone, C. G. Read, A. J. Biacchi, A. M. Wiltrout, N. S. Lewis, R. E. Schaak, J. Nanostructured nickel phosphide as an electrocatalyst for the hydrogen evolution reaction. J Am Chem Soc. 2013 Jun 26;135(25):9267-70. doi: 10.1021/ja403440e. Epub 2013 Jun 13.

[20] H. Vrubel, X. Hu, Angew. Molybdenum Boride and Carbide Catalyze Hydrogen Evolution in both Acidic and Basic Solutions. Chem. Int. Ed. 2012, 51, 12703–12706.

[21] Navarro-Flores, E.; Chong, Z.; Omanovic, S. Characterization of Ni, NiMo, NiW and NiFe electroactive coatings as electrocatalysts for hydrogen evolution in an acidic medium. J. Mol. Catal. A Chem. 2005, 226, 179–197.

[22] D. V. Esposito, S. T. Hunt, A. L. Stottlemyer, K. D. Dobson, B. E. McCandless, R. W. Birkmire, J. G. Chen, Low-cost hydrogen-evolution catalysts based on monolayer platinum on tungsten monocarbide substrates. Angew. Chem. 2010, 122, 10055 – 10058; Angew. Chem. Int. Ed. 2010, 49, 9859 – 9862.

[23] T. F. Jaramillo, K. P. Jorgensen, J. Bonde, J. H. Nielsen, S. Horch, I. Chorkendorff, Identification of active edge sites for electrochemical H2 evolution from MoS2 nanocatalysts. Science 2007, 317, 100 – 102.

[24] P. D. Tran, A. L. Goff, J. Heidkamp, B. Jousselme, N. Guillet, S. Palacin, H. Dau, M. Fontecave, V. Artero, Bio-inspired Noble Metal-Free Nanomaterials Approaching Platinum Performances for H2 Evolution and Uptake. Angew. Chem. 2011, 123, 1407-1410; Angew. Chem. Int. Ed. 2011, 50, 1371 – 1374; b) M. L. Helm, M. P. Stewart, M. Bullock, M. R. DuBois, D. L. DuBois, Science 2011, 333, 863- 866.

[25] Zhao, G.; Rui, K.; Dou, X. S.; Sun, W. Heterostructures for Electrochemical Hydrogen Evolution Reaction: A Review. Adv. Funct. Mater. 2018, 28, No. 1803291.

[26] Sapountzi, F. M.; Gracia, J. M.; Weststrate, C. J. (K.-J.).; Fredriksson, H. O. A.; Niemantsverdriet, J. W. (H.). Electrocatalysts for the generation of hydrogen, oxygen and synthesis gas. Prog. Energy Combust. Sci. 2017, 58, 1−35.

[27] Chen, Z.; Duan, X.; Wei, W.; Wang, S.; Ni, B.-J. Recent advances in transition metal-based electrocatalysts for alkaline hydrogen evolution. J. Mater. Chem. A 2019, 7, 14971.

[28] I. l. B. Pehlivan, M. A. Arvizu, Z. Qiu, G. A. Niklasson, and T. Edvinsson, "Impedance Spectroscopy Modeling of Nickel–Molybdenum Alloys on Porous and Flat Substrates for Applications in Water Splitting," J. Phys. Chem. C, vol. 123, no. 39, pp. 23890-23897, 2019, doi: 10.1021/acs.jpcc.9b02714.

[29] Mert Manazoğla' - Gikee Hapes' - Gükhan Orhan' Effect of electrolysis parameters of Ni-Mo alloy on the electrocatalytic activity for hydrogen evaluation and their stability in alkali medium

[30] M.P.M. Kaninski, S.M. Miulovic, G.S. Tasic, A.D. Maksic, and V.M. Nikolic, A Study on the Co-W Activated Ni Electrodes for the Hydrogen Production from Alkaline Water Electrolysis-Energy Saving, Int. J. Hydrog. Energy, 2011, 36, p 5227–5235

[31] R. Solmaz and G. Kardas, Electrochemical Deposition and Characterization of NiFe Coatings as Electrocatalytic Materials for Alkaline Water Electrolysis, Electrochim Acta, 2009, 54, p 3726–3734

[32] M. Manazoğlu, G. Hapçı, and G. Orhan, "Electrochemical Deposition and Characterization of Ni-Mo Alloys as Cathode for Alkaline Water Electrolysis," Journal of materials engineering and performance, vol. 25, no. 1, pp. 130-137, 2015, doi: 10.1007/s11665-015-1849-7.

[33] Y. Wang et al., "A 3D Nanoporous Ni–Mo Electrocatalyst with Negligible Overpotential for Alkaline Hydrogen Evolution," ChemElectroChem, vol. 1, no. 7, pp. 1138-1144, 2014, doi: 10.1002/celc.201402089.

[34] E.J. Popczun, J.R. McKone, C.G. Read, A.J. Biacchi, A.M. Wiltrout, N.S. Lewis, et al., Nanostructured nickel phosphide as an electrocatalyst for the hydrogen evolution reaction, J. Am. Chem. Soc. 135 (2013) 9267e9270, https://doi.org/10.1021/ja403440e.

[35] M. Ledendecker, S. Krick Calder_on, C. Papp, H.-P. Steinrück, M. Antonietti, M. Shalom, The synthesis of nanostructured Ni 5 P 4 films and their use as a non-noble bifunctional electrocatalyst for full water splitting, Angew. Chem. 127 (2015) 12538e12542, https://doi.org/10.1002/ange.201502438.

[36] W. Zhu, X. Yue, W. Zhang, S. Yu, Y. Zhang, J. Wang, et al., Nickel sulfide microsphere film on Ni foam as an efficient bifunctional electrocatalyst for overall water splitting, Chem. Commun. 52 (2016) 1486e1489, https://doi.org/10.1039/C5CC08064A.

[37] I. Paseka, Hydrogen evolution reaction on amorphous Ni-P and Ni-S electrodes and the internal stress in a layer of these electrodes, Electrochim. Acta 47 (2001) 921e931, https://doi.org/10.1016/S0013-4686(01)00814-3.

[38] M. Schalenbach, F. D. Speck, M. Ledendecker, O. Kasian, D. Goehl, A. M. Mingers, B. Breitbach, H. Springer, S. Cherevko, and K.J.J. Mayrhofer. Nickel-molybdenum alloy catalysts for the hydrogen evolution reaction: Activity and stability revised. Electrochimica acta, 259:1154-1161, 2018.

[39] Z. Li, C. Yu, Y. Wen, Y. Gao, X. Xing, Z. Wei, H. Sun, Y.-W. Zhang, W. Song, Mesoporous hollow Cu-Ni alloy nanocage from core-shell Cu@ Ni nanocube for efficient hydrogen evolution reaction, ACS Catal. 9 (2019) 5084–5095.

[40] Q. Zhang, P. Li, D. Zhou, Z. Chang, Y. Kuang, and X. Sun. Superaerophobic Ultrathin Ni-Mo Alloy Nanosheet Array from In Situ Topotactic Reduction for Hydrogen Evolution Reaction. Small (Weinheim an der Bergstrasse, Germany), 13(41):1701648-n/a, 2017.

[41] G.B. Darband, M. Aliofkhazraei, A.S. Rouhaghdam, M. Kiani, Three-dimensional Ni-Co alloy hierarchical nanostructure as efficient non-noble-metal electrocatalyst for hydrogen evolution reaction, Appl. Surf. Sci. 465 (2019) 846–862.

[42] B. Zhang, F. Yang, X. Liu, N. Wu, S. Che, and Y. Li, "Phosphorus doped nickel-molybdenum aerogel for efficient overall water splitting," Applied catalysis. B, Environmental, vol. 298, p. 120494, 2021, doi: 10.1016/j.apcatb.2021.120494.

[43] McCrory, C. C. L.; Jung, S.; Ferrer, I. M.; Chatman, S. M.; Peters, J. C.; Jaramillo, T. F. Benchmarking Hydrogen Evolving Reaction and Oxygen Evolving Reaction

Electrocatalysts for Solar Water Splitting Devices. J. Am. Chem. Soc. 2015, 137, 4347−4357.

[44] McKone, J. R.; Warren, E. L.; Bierman, M. J.; Boettcher, S. W.; Brunschwig, B. S.; Lewis, N. S.; Gray, H. B. Evaluation of Pt, Ni, and Ni−Mo Electrocatalysts for Hydrogen Evolution on Crystalline Si Electrodes. Energy Environ. Sci. 2011, 4, 3573−3583.

[45] Zhang, L.; Xiong, K.; Nie, Y.; Wang, X.; Liao, J.; Wei, Z. Sputtering Nickel−Molybdenum Nanorods as an Excellent Hydrogen Evolution Reaction Catalyst. J. Power Sources 2015, 297, 413−418.

[46] J.M. Jaksic, M.V. Vojnovic, N.V. Krstajic, Kinetic analysis of hydrogen evolution at Ni e Mo alloy electrodes, Electrochem. Acta 45 (2000) 4151e4158.

[47] J.R. McKone, B.F. Sadtler, C.A. Werlang, N.S. Lewis, H.B. Gray, Ni-Mo nanopowders for efficient electrochemical hydrogen evolution, ACS Catal. 3 (2013) 166e169, https://doi.org/10.1021/cs300691m.

[48] M. Pourbaix, Atlas of Electrochemical Equilibria in Aqueous Solutions, second ed., NACE International, Cecelcor, Houston, 1974.

[49] [37] S. Cherevko, S. Geiger, O. Kasian, N. Kulyk, J.P. Grote, A. Savan, et al., Oxygen and hydrogen evolution reactions on Ru, RuO2, Ir, and IrO2 thin film electrodes in acidic and alkaline electrolytes: a comparative study on activity and stability, Catal. Today 262 (2016) 170e180, https://doi.org/10.1016/j.cattod.2015.08.014.

[50] [41] S.O. Klemm, A.A. Topalov, C.A. Laska, K.J.J. Mayrhofer, Coupling of a high throughput microelectrochemical cell with online multielemental trace analysis by ICP-MS, Electrochem. Commun. 13 (2011) 1533e1535, https://doi.org/10.1016/j.elecom.2011.10.017.

[51] Keith B Oldham. Electrochemical science and technology : fundamentals and applications. Wiley, Chichester, 2012.

[52] G. Jerkiewicz. Standard and Reversible Hydrogen Electrodes: Theory,Design, Operation, and Applications. ACS Catalysis, 10(15):8409-8417, 2020.

[53] C. Wei, R.R. Rao, J. Peng, B. Huang, I. E. L. Stephens, M. Risch, Z. J. Xu, and Y. Shao-Horn. Recommended Practices and Benchmark Activity for Hydrogen and Oxygen Electrocatalysis in Water Splitting and Fuel Cells. Advanced Materials, 31(31):1806296, 2019.

[54] Allen J Bard. Electrochemical methods: fundamentals and applications. Wiley, New York, 2nd ed. edition, 2001.

[55] Isao Abe. Alkaline Water Electrolysis. ENERGY CARRIERS AND CONVERSION SYSTEMS – Vol. I

[56] M.T.M. Koper Thermodynamic theory of multi-electron transfer reactions: implications for electrocatalysis

J. Electroanal. Chem., 660 (2) (2011), pp. 254-260

[57] N.M. Marković, P.N. Ross Surface science studies of model fuel cell electrocatalysts Surf. Sci. Rep., 45 (4) (2002), pp. 117-229

[58] B.E. Conway, B.V. Tilak Interfacial processes involving electrocatalytic evolution and oxidation of H2, and the role of chemisorbed H Electrochim. Acta, 47 (22) (2002), pp. 3571-3594

[59] J. Wang, et al. Recent progress in cobalt-based heterogeneous catalysts for electrochemical water splitting

Adv. Mater., 28 (2) (2016), pp. 215-230

[60] X. Zou, Y. Zhang Noble metal-free hydrogen evolution catalysts for water splitting Chem. Soc. Rev., 44 (15) (2015), pp. 5148-5180

[61] J.O.M. Bockris, E.C. Potter The mechanism of hydrogen evolution at nickel cathodes in aqueous solutions J. Chem. Phys., 20 (4) (1952), pp. 614-628

[62] Martin Ďurovič, Jaromír Hnát, Karel Bouzek, Electrocatalysts for the hydrogen evolution reaction in alkaline and neutral media. A comparative review, Journal of Power Sources, Volume 493, 2021, 229708, ISSN 0378-7753, https://doi.org/10.1016/j.jpowsour.2021.229708.

[63] F.M. Sapountzi, et al. Electrocatalysts for the generation of hydrogen, oxygen and synthesis gas Prog. Energy Combust. Sci., 58 (2017), pp. 1-35

[64] J.M. Jakšić, M.V. Vojnović, N.V. Krstajić Kinetic analysis of hydrogen evolution at Ni–Mo alloy electrodes Electrochim. Acta, 45 (25) (2000), pp. 4151-4158

[65] M.F. Kibria, M.S. Mridha, A.H. Khan Electrochemical studies of a nickel electrode for the hydrogen evolution reaction Int. J. Hydrogen Energy, 20 (6) (1995), pp. 435-440

[66] B.E. Conway, L. Bai Determination of adsorption of OPD H species in the cathodic hydrogen evolution reaction at Pt in relation to electrocatalysis J. Electroanal. Chem. Interfacial Electrochem., 198 (1) (1986), pp. 149-175

[67] E. Chassaing, N. Portail, A.-f. Levy, and G. Wang. Characterisation of electrodeposited nanocrystalline Ni-Mo alloys. Journal of applied electrochemistry, 34(11):1085-1091, 2004.

[68] H. Wendt, et al. Electrocatalysis and electrocatalysts for low temperature fuel cells: fundamentals, state of the art, research and development Quim. Nova, 28 (6) (2005), pp. 1066-1075

[69] M.T.M. Koper Thermodynamic theory of multi-electron transfer reactions: implications for electrocatalysis

J. Electroanal. Chem., 660 (2) (2011), pp. 254-260

[70] B. Ruqia and S. I. Choi, ChemSusChem, 2018, 11, 2643–2653.

[71] J. X. Feng, J. Q. Wu, Y. X. Tong and G. R. Li, J. Am. Chem. Soc., 2018, 140, 610–617.

[72] M. G. Walter, E. L. Warren, J. R. McKone, S. W. Boettcher, Q. Mi, E. A. Santori, and N. S. Lewis. Solar Water Splitting Cells. Chemical reviews, 110(11):6446-6473, 2010.

[73] S. Anantharaj, et al. Recent trends and perspectives in electrochemical water splitting with an emphasis on sulfide, selenide, and phosphide catalysts of Fe, Co, and Ni: a review

ACS Catal., 6 (12) (2016), pp. 8069-8097

[74] N. Mahmood, et al. Electrocatalysts for hydrogen evolution in alkaline electrolytes: mechanisms, challenges, and prospective solutions Advanced Science, 5 (2) (2018), p. 23

[75] P.C.K. Vesborg, B. Seger, I. Chorkendorff Recent development in hydrogen evolution reaction catalysts and their practical implementation J. Phys. Chem. Lett., 6 (6) (2015), pp. 951-957

[76] S. Anantharaj, et al. Precision and correctness in the evaluation of electrocatalytic water splitting: revisiting activity parameters with a critical assessment. Energy Environ. Sci., 11 (4) (2018), pp. 744-771

[77] S. Anantharaj, S. Kundu Do the evaluation parameters reflect intrinsic activity of electrocatalysts in electrochemical water splitting? ACS Energy Letters, 4 (6) (2019), pp. 1260-1264

[78] A. Eftekhari Electrocatalysts for hydrogen evolution reaction

Int. J. Hydrogen Energy, 42 (16) (2017), pp. 11053-11077

[79] F. Safizadeh, E. Ghali, G. Houlachi Electrocatalysis developments for hydrogen evolution reaction in alkaline solutions – a Review Int. J. Hydrogen Energy, 40 (1) (2015), pp. 256-274

[80] L. Zhang, et al. Facile route of nitrogen doping in nickel cobalt phosphide for highly efficient hydrogen evolution in both acid and alkaline electrolytes. Appl. Surf. Sci., 512 (2020), Article 145715

[81] D.M.F. Santos, et al. Platinum–rare earth electrodes for hydrogen evolution in alkaline water electrolysis. Int. J. Hydrogen Energy, 38 (8) (2013), pp. 3137-3145

[82] C.I. Müller, et al. Electrochemical investigations on amorphous Fe-base alloys for alkaline water electrolysis

Int. J. Hydrogen Energy, 39 (17) (2014), pp. 8926-8937

[83] J. Erlebacher, M. Aziz, A. Karma, N. Dimitrov, K. Sieradzki, Evolution of nanoporosity in dealloying, Nature 410 (2001) 450e453, https://doi.org/10.1038/35068529.

[84] T. Shinagawa, A.T. Garcia-Esparza, and K. Takanabe. Insight on Tafel slopes from a microkinetic analysis of aqueous electrocatalysis for energy conversion. Scientific reports, 5(1):13801-13801, 2015.

[85] Z.-F. Huang, J. Wang, Y. C. Peng, C.-Y. Jung, A. Fisher and X. Wang, Adv. Energy Mater., 2017, 7, 1700544.

[86] I.A. Raj and K.I. Vasu. Transition metal-based hydrogen electrodes in alkaline solution - electrocatalysis on nickel based binary alloy coatings. Journal of applied electrochemistry, 20(1):32-38, 1990.

[87] J. Zhang, T. Wang, P. Liu, Z. Liao, S. Liu, X. Zhuang, M. Chen, E. Zschech, and X. Feng. Efficient hydrogen production on MoNi4 electrocatalysts with fast water dissociation kinetics. Nature communications, 8(1):15437-15437, 2017.

[88] Strmcnik, D.; Lopes, P. P.; Genorio, B.; Stamenkovic, V. R.; Markovic, N. M. Design principles for hydrogen evolution reaction catalyst materials. Nano Energy 2016, 29, 29−36.

[89] J. Halim, R. Abdel-Karim, S. El-Raghy, M. Nabil, and A. Waheed, "Electrodeposition and Characterization of Nanocrystalline Ni-Mo Catalysts for Hydrogen Production," Journal of nanomaterials, vol. 2012, pp. 1-9, 2012, doi: 10.1155/2012/845673.

[90] M. Fang, W. Gao, G. Dong, Z. Xia, S. Yip, Y. Qin, Y. Qu, and J. C. Ho. Hierarchical NiMo-based 3D electrocatalysts for highly-efficient hydrogen evolution in alkaline conditions. Nano energy, 27:247-254, 2016.

[91] N. Alonso-Vante, C.A.S. Rold_an, R. de Guadalupe, G. Huerta, G. R. Sanchez, and A.M. Robledo. Fundamentals of Electrocatalyst Materials and Interfacial Characterization. Wiley, USA, 2019.

[92] R. Zhang, X. Wang, S. Yu, T. Wen, X. Zhu, F. Yang, X. Sun, X. Wang, and W. Hu. Ternary NiCo2Px Nanowires as ph-Universal Electrocatalysts for Highly Efficient Hydrogen Evolution Reaction. Advanced Materials, 29(9):1605502, 2017.

[93] C. Huang, et al. Ultrathin NiCo2Px nanosheets strongly coupled with CNTs as efficient and robust electrocatalysts for overall water splitting. J. Mater. Chem., 6 (17) (2018), pp. 7420-7427

[94] T. Tian, et al. Surface anion-rich NiS2 hollow microspheres derived from metal–organic frameworks as a robust electrocatalyst for the hydrogen evolution reaction J. Mater. Chem., 5 (39) (2017), pp. 20985-20992

[95] K. Wang, et al. Efficient and stable Ni–Co–Fe–P nanosheet arrays on Ni foam for alkaline and neutral hydrogen evolution. International Journal of Hydrogen Energy 45 (4) (2020), pp. 2504-2512

[96] Hong Xu, Ning Li, Qinghua Zhuo, Lirong Lu, Weizeng Chen Phase, microstructure and service character of as-deposited and short-time heat-treated Ni-Mo alloys with mixed state. Published: May 21, 2021

[97] Wojewoda-Budka J., Wierzbicka-Miernik A., Litynska-Dobrzynska L., Szczerba M.J., Mordarski G., Mosiałek M., et al., Microstructure characteristics and phase transformations of the Ni-P and Ni-P-Re electroless deposited coatings after heat treatment[J], Electrochimica Acta, 2016, 209: 183–191

[98] Li N., Gao C.H., Yang S.Z. Crystallization Kinetics of Electrodeposited Amorphous/Nanocrystalline Ni81.32Mo18.68 Alloy Coating[J], Acta Physico-Chimica Sinica, 2009, 25(4): 735–740

[99] McCrory, C. C. L.; Jung, S.; Ferrer, I. M.; Chatman, S. M.; Peters, J. C.; Jaramillo, T. F. Benchmarking Hydrogen Evolving Reaction and Oxygen Evolving Reaction Electrocatalysts for Solar Water Splitting Devices. J. Am. Chem. Soc. 2015, 137, 4347−4357.

[100] McKone, J. R.; Warren, E. L.; Bierman, M. J.; Boettcher, S. W.; Brunschwig, B. S.; Lewis, N. S.; Gray, H. B. Evaluation of Pt, Ni, and Ni−Mo Electrocatalysts for Hydrogen Evolution on Crystalline Si Electrodes. Energy Environ. Sci. 2011, 4, 3573−3583.

[101] Zhang, L.; Xiong, K.; Nie, Y.; Wang, X.; Liao, J.; Wei, Z. Sputtering Nickel−Molybdenum Nanorods as an Excellent Hydrogen Evolution Reaction Catalyst. J. Power Sources 2015, 297, 413−418.

[102] L. Zhang, K. Xiong, Y. Nie, X. Wang, J. Liao, and Z. Wei, "Sputtering nickel-molybdenum nanorods as an excellent hydrogen evolution reaction catalyst," Journal of power sources, vol. 297, pp. 413-418, 2015, doi: 10.1016/j.jpowsour.2015.08.004.

[103] Chen Liang-Yu; Xu Tianxiang; Lu Sheng; Wang Ze-Xin; Chen Shujin; Zhang Lai-Chang. Improved hardness and wear resistance of plasma sprayed nanostructured NiCrBSi coating via short-time heat treatment[J], Surface and Coatings Technology, 2018, 350: 436–444

[104] Guo Wei; Wang Haiyan; Jia Qiang; Peng Peng; Zhu Ying. Transient Liquid Phase Bonding of Nickel-Base Single Crystal Alloy with a Novel Ni-Cr-Co-Mo-W-Ta-Re-B Amorphous Interlayer[J], High Temperature Materials and Processes, 2017, 36(7): 677–682

[105] Semenenko K. I.; Kashirin M. A.; Stognei O. V.; Al-Maliki A. D. Thermal stability, structure and phase composition of Nix(NbO)100−xcomposites[J], Journal of Surface Investigation. X-ray, Synchrotron and Neutron Techniques, 2016, 10(5): 1087–1091

[106] Wasekar N.P.; Verulkar S.; Vamsi M.V.N.; Sundararajan G., Influence of molybdenum on the mechanical properties, electrochemical corrosion and wear behavior of electrodeposited Ni-Mo alloy, Surface and Coatings Technology, 2019, 370: 298–310

[107] Luo Hong, Leitch Michael, Behnamian Yashar, Ma Yongsheng, Zeng Hongbo, Luo Jing-Li. Development of electroless Ni–P/nano-WC composite coatings and investigation on its properties[J], Surface & Coatings Technology, 2015, 277: 99–106

[108] Safizadeh, F.; Ghali, E.; Houlachi, G. Electrocatalysis developments for hydrogen evolution reaction in alkaline solutions − a review. Int. J. Hydrogen Energy 2015, 40, 256−74.

[109] Grätzel, M. Photoelectrochemical Cells. Nature 2001, 414, 338−344.

[110] Navarro, R. M.; Alvarez−Galván, M. C.; Villoria de la Mano, J. A.; Al−Zahrani, S. M.; Fierro, J. L. G. A Framework for Visible−Light Water Splitting. Energy Environ. Sci. 2010, 3, 1865−1882.

[111] Walter, M. G.; Warren, E. L.; McKone, J. R.; Boettcher, S. W.; Mi, Q.; Santori, E. A.; Lewis, N. S. Solar Water Splitting Cells. Chem. Rev. 2010, 110, 6446−6473.

[112] Vilekar, S. A.; Fishtik, I.; Dattaz, R. Kinetics of the Hydrogen Electrode Reaction. J. Electrochem. Soc. 2010, 157, B1040−B1050.

[113] J. A. Bau, S. M. Kozlov, L. M. Azofra, S. Ould-Chikh, A.-H. Emwas, H. Idriss, L. Cavallo, and K. Takanabe. Role of Oxidized Mo Species on the Active Surface of NiMo Electrocatalysts for Hydrogen Evolution under Alkaline Conditions. ACS catalysis, 10(21):12858-12866, 2020

[114] Y. Jin, X. Yue, C. Shu, S. Huang, and P. K. Shen, "Three-dimensional porous MoNi4 networks constructed by nanosheets as bifunctional electrocatalysts for overall water splittingElectronic supplementary information (ESI) available. See DOI: 10.1039/c6ta10802d," vol. 5, no. 6, pp. 258-2513, 2017, doi: 10.1039/c6ta10802d.

[115] B. Cai, A. Eychmuller, Promoting electrocatalysis upon aerogels, Adv. Mater. 31(2019), 1804881.

[116] N.C. Bigall, A.K. Herrmann, M. Vogel, M. Rose, P. Simon, W. Carrillo-Cabrera, D. Dorfs, S. Kaskel, N. Gaponik, A. Eychmuller, Hydrogels and aerogels from noble metal nanoparticles, Angew. Chem. Int. Ed. Engl. 48 (2009) 9731–9734.

[117] B. Cai, D. Wen, W. Liu, A.-K. Herrmann, A. Benad, A. Eychmüller, Function-led design of aerogels: self-assembly of alloyed PdNi hollow nanospheres for efficient electrocatalysis, Angew. Chem. Int. Ed. Eng. 54 (2015) 13101–13105.

[118] X. Tang, L. Xiao, C. Yang, J. Lu, and L. Zhuang, "Noble fabrication of Ni–Mo cathode for alkaline water electrolysis and alkaline polymer electrolyte water electrolysis," International journal of hydrogen energy, vol. 39, no. 7, pp. 3055-3060, 2014, doi: 10.1016/j.ijhydene.2013.12.053.

[119] T. Wang, Y. Guo, Z. Zhou, X. Chang, J. Zheng, and X. Li, "Ni–Mo Nanocatalysts on N-Doped Graphite Nanotubes for Highly Efficient Electrochemical Hydrogen Evolution in Acid," ACS Nano, vol. 10, no. 11, pp. 10397-10403, 2016, doi: 10.1021/acsnano.6b06259.

[120] Edita Vernickaite˙ 1 , Oksana Bersirova 2 , Henrikas Cesiulis 1 and Natalia Tsyntsaru 1,3,* Design of Highly Active Electrodes for Hydrogen Evolution Reaction Based on Mo-Rich Alloys Electrodeposited from Ammonium Acetate Bath

[121] Subbaraman, R. et al. Trends in activity for the water electrolyser reactions on 3d M (Ni, Co, Fe, Mn) hydr (oxy) oxide catalysts. Nat. Mater. 11, 550–557 (2012).

[122] Hinnemann, B. et al. Biomimetic hydrogen evolution: MoS2 nanoparticles as catalyst for hydrogen evolution. J. Am. Chem. Soc. 127, 5308–5309 (2005).

[123] Tran, P. D. et al. Coordination polymer structure and revisited hydrogen evolution catalytic mechanism for amorphous molybdenum sulfide. Nat. Mater. 15, 640–646 (2016).

[124] Ng, J. W. D. et al. Gold-supported cerium-doped NiOx catalysts for water oxidation. Nat. Energy 1, 16053–16060 (2016).

[125] Jakši´c, J.M.; Vojnovi´c, M.V.; Krstaji´c, N.V. Kinetic analysis of hydrogen evolution at Ni–Mo alloy electrodes. Electrochim. Acta 2000, 45, 4151–4158.

[126] Xu, C.; Zhou, J.; Zeng, M.; Fu, X.; Liu, X.; Li, J. Electrodeposition mechanism and characterization of Ni–Mo alloy and its electrocatalytic performance for hydrogen evolution. Int. J. Hydrogen Energy 2016, 41, 13341–13349.

[127] Mech, K.; Zabinski, P.; Mucha, M.; Kowalik, R. Electrodeposition of catalytically active Ni–Mo alloys/elektroosadzanie aktywnych katalitycznie stopów Ni–Mo. Arch. Metall. Mater. 2013, 58, 227–229.

[128] Jeremiasse, A.W.; Bergsma, J.; Kleijn, J.M.; Saakes, M.; Buisman, C.J.N.; Cohen Stuart, M.; Hamelers, H.V.M. Performance of metal alloys as hydrogen evolution reaction catalysts in a microbial electrolysis cell. Int. J. Hydrogen Energy 2011, 36, 10482–10489.

[129] M. Wang, Z. Wang, X. Yu, Z. Guo, Hierarchically 3D porous films electrochemically constructed on gas–liquid–solid three-phase interface for energy application. Int. J. Hydrogen Energy 2015, 40, 2173–2181.

[130] J. A. Bau et al., "Role of Oxidized Mo Species on the Active Surface of Ni–Mo Electrocatalysts for Hydrogen Evolution under Alkaline Conditions," ACS Catal, vol. 10, no. 21, pp. 12858-12866, 2020, doi: 10.1021/acscatal.0c02743.

[131] Topological formation of a Mo–Ni-based hollow structure as a highly efficient electrocatalyst for the hydrogen evolution reaction in alkaline solutions. ACS Appl. Mater. Interfaces, 11 (24) (2019), pp. 21998-22004

[132] J. R. McKone, B. F. Sadtler, C. A. Werlang, N. S. Lewis, and H. B. Gray, "Ni–Mo Nanopowders for Efficient Electrochemical Hydrogen Evolution," ACS Catal, vol. 3, no. 2, pp. 166-169, 2013, doi: 10.1021/cs300691m.

[133] K. Hu, S. Jeong, M. Wakisaka, J.-i. Fujita, and Y. Ito, "Bottom-up Synthesis of Porous NiMo Alloy for Hydrogen Evolution Reaction," Metals (Basel), vol. 8, no. 2, p. 83, 2018, doi: 10.3390/met8020083.

[134] Raj, I.A.; Venkatesan, V.K. Characterization of nickel-molybdenum and nickel-molybdenum-iron alloy coatings as cathodes for alkaline water electrolysers. Int. J. Hydrogen Energy 1988, 13, 215–223.

[135] González-Buch, C.; Herraiz-Cardona, I.; Ortega, E.M.; García-Antón, J.; Pérez-Herranz, V. Development of Ni–Mo, Ni–W and Ni–Co macroporous materials for hydrogen evolution reaction. Chem. Eng. Trans. 2013, 32, 865–870.

[136] Martinez, S.; Metikoš-Hukovi´c, M.; Valek, L. Electrocatalytic properties of electrodeposited Ni–15Mo cathodes for the HER in acid solutions: Synergistic electronic effect. J. Mol. Catal. A Chem. 2006, 245, 114–121.

[137] C. C. Nee, W. Kim, and R. Weil, "Pulsed electrodeposition of Ni-Mo alloys," Journal of the Electrochemical Society, vol. 135, no. 5, pp. 1100–1103, 1988.

[138] J. Divisek, H. Schmitz, and J. Balej, "Ni and Mo coatings as hydrogen cathodes," Journal of Applied Electrochemistry, vol. 19, no. 4, pp. 519–530, 1989.

[139] C. Xu, J. Bo Zhou, M. Zeng, X. ling Fu, X. jiang Liu, J. ming Li, Enhancing the Performance of Ni-Mo Alkaline Hydrogen Evolution Electrocatalysts with Carbon Supports. Int. J.Hydrogen Energy 2016, 41, 13341–13349.

[140] Y. Zeng, Z. Li, M. Ma, and S. Zhou, "In situ surface Raman study of the induced codeposition mechanism of Ni-Mo alloys," Electrochemistry Communications, vol. 2, no. 1, pp. 36– 38, 2000.

[141] J. G. Highfield, E. Claude, K. Oguro, Electrocatalytic synergism in Ni/Mo cathodes for hydrogen evolution in acid medium: A new model. Electrochim. Acta 1999, 44, 2805–2814.

[142] L. Zu, J. He, X. Liu, L. Zhang, K. Zhou, Electrochemical performance of porous Ni–Cr–Mo–Cu alloys for hydrogen evolution reactions in alkali solution. Int. J. Hydrogen Energy 2019, 44, 4650–4655.

[143] M. Donten, H. Cesiulis, and Z. Stojek, "Electrodeposition of amorphous/nanocrystalline and polycrystalline Ni-Mo alloys from pyrophosphate baths," Electrochimica Acta, vol. 50, no. 6, pp. 1405–1412, 2005.

[144] G. S. Tasic, S. P. Maslovara, D. L. Zugic, A. D. Maksic, M. P. Marceta Kaninski, Characterization of analysis of hydrogen by steam reforming. Int. J. Hydrogen Energy 2011, 36, 11588–11595.

Appendix A: Health, Safety, and Environment (HSE)

Table A.1: List of the used chemicals and their hazard and precautionary statements

Chemical	Producer	Hazard statements	Precautionary statements
$NiSO_4 \cdot 6H_2O$	Sigma-Aldrich	H302 + H332: Harmful if swallowed or if inhaled. H315: Causes skin irritation. H317: May cause an allergic skin reaction**.** H334: May cause allergy or asthma symptoms or breathing difficulties if inhaled. H341: Suspected of causing genetic defects. H350: May cause cancer. H360D: May damage the unborn child. H372: Causes damage to organs (Respiratory Tract) through prolonged or repeated exposure if inhaled. H410: Very toxic to aquatic life with long lasting effects.	P273: Avoid release to the environment. P280: Wear protective gloves/ protective clothing/ eye protection/ face protection/ hearing protection. P301 + P312: IF SWALLOWED: Call a POISON CENTER/ doctor if you feel unwell. P302 + P352: IF ON SKIN: Wash with plenty of water. P304 + P340 + P312: IF INHALED: Remove person to fresh air and keep comfortable for breathing. Call a POISON CENTER/ doctor if you feel unwell. P308 + P313: IF exposed or concerned: Get medical advice/ attention.
$Na_3C_6H_5O_7 \cdot 2H_2O$	Sigma-Aldrich	None	If inhaled After inhalation: fresh air. In case of skin contact In case of skin contact: Take off immediately all contaminated clothing. Rinse skin with water/ shower. In case of eye contact After eye contact: rinse out with plenty of water. Remove contact lenses. If swallowed

			After swallowing: make victim drink water (two glasses at most). Consult doctor if feeling unwell.
$Na_2MoO_4 \cdot 2H_2O$	Sigma-Aldrich	None	Avoid breathing dust. Use only in a well-ventilated area. IF INHALED: Remove to fresh air and keep at rest in a position comfortable for breathing.
NH_4OH	Sigma-Aldrich	H314: Causes severe skin burns and eye damage. H335: May cause respiratory irritation. H410: Very toxic to aquatic life with long lasting effects.	P261: Avoid breathing dust/ fume/ gas/ mist/ vapors/ spray. P271: Use only outdoors or in a well-ventilated area. P273: Avoid release to the environment. P280: Wear protective gloves/ protective clothing/ eye protection/ face protection/ hearing protection. P303 + P361 + P353: IF ON SKIN (or hair): Take off immediately all contaminated clothing. Rinse skin with water. P305 + P351 + P338 IF IN EYES: Rinse cautiously with water for several minutes. Remove contact lenses, if present and easy to do. Continue rinsing.
KOH	Sigma-Aldrich	H290: May be corrosive to metals. H302: Harmful if swallowed. H314: Causes severe skin burns and eye damage.	P234: Keep only in original packaging. P260: Do not breathe dusts or mists. P280: Wear protective gloves/ protective clothing/ eye protection/ face protection/ hearing protection. P301 + P312: IF SWALLOWED: Call a POISON CENTER/ doctor if you feel unwell. P303 + P361 + P353: IF ON SKIN (or hair): Take off immediately all contaminated clothing. Rinse skin with water. P305 + P351 + P338: IF IN EYES: Rinse cautiously with water for several minutes.

			Remove contact lenses, if present and easy to do. Continue rinsing.
HNO_3	Sigma-Aldrich	H272: May intensify fire; oxidizer. H290: May be corrosive to metals. H314: Causes severe skin burns and eye damage. H331: Toxic if inhaled.	P210: Keep away from heat, hot surfaces, sparks, open flames and other ignition sources. No smoking. P220: Keep away from clothing and other combustible materials. P280: Wear protective gloves/ protective clothing/ eye protection/ face protection/ hearing protection. P303 + P361 + P353: IF ON SKIN (or hair): Take off immediately all contaminated clothing. Rinse skin with water. P304 + P340 + P310: IF INHALED: Remove person to fresh air and keep comfortable for breathing. Immediately call a POISON CENTER/ doctor. P305 + P351 + P338: IF IN EYES: Rinse cautiously with water for several minutes. Remove contact lenses, if present and easy to do. Continue rinsing.
HF	Sigma-Aldrich	H300 + H310 + H330: Fatal if swallowed, in contact with skin or if inhaled. H314: Causes severe skin burns and eye damage.	P260: Do not breathe dust/ fume/ gas/ mist/ vapors/ spray. P270: Do not eat, drink or smoke when using this product. P280: Wear protective gloves/ protective clothing/ eye protection/ face protection/ hearing protection. P303 + P361 + P353: IF ON SKIN (or hair): Take off immediately all contaminated clothing. Rinse skin with water. P304 + P340 + P310: IF INHALED: Remove person to fresh air and keep comfortable for breathing. Immediately call a POISON CENTER/ doctor.

			P305 + P351 + P338: IF IN EYES: Rinse cautiously with water for several minutes. Remove contact lenses, if present and easy to do. Continue rinsing.
Ti	Sigma-Aldrich	None	None
N_2	Praxair	H280: Gas under pressure	Wear eye protection
Loctite epoxy	Sigma-Aldrich	Bonds skin in seconds. Combustible liquid. Causes eye irritation. May cause respiratory irritation	Keep away from heat, sparks, open flames, hot surfaces - no smoking. Avoid breathing vapors, mist, or spray. Wash affected area thoroughly after handling. Use only outdoors or in a well-ventilated area. Wear protective gloves, eye protection, and face protection. IF INHALED: Remove victim to fresh air and keep at rest in a position comfortable for breathing. Call a POISON CENTER or physician if you feel unwell. IF IN EYES: Rinse cautiously with water for several minutes. Remove contact lenses, if present and easy to do. Continue rinsing. If eye irritation persists: Get medical attention. In case of fire: Use foam, dry chemical or carbon dioxide to extinguish.

Risk assessment:

The work has been done in safety glasses and gloves. Preparation of all solutions, including adjustment of pH by ammonia solution, have been done in good-ventilated synthesis lab. The etching procedure with use of the mixture of nitric and hydrofluoric has been performed in a fume hood, wearing a lab coat and Nitrile gloves. All solution residuals have been stored in a special vessel containing Ni and Mo ions. Work with use of N_2, the prepared solutions, and Loctite epoxy has been done in a good-ventilated lab as well. Since most of the work has been done in a location with gas vessels and gas mixers, the regular check for leakage of gases has been done.

Appendix B: X-Ray diffraction

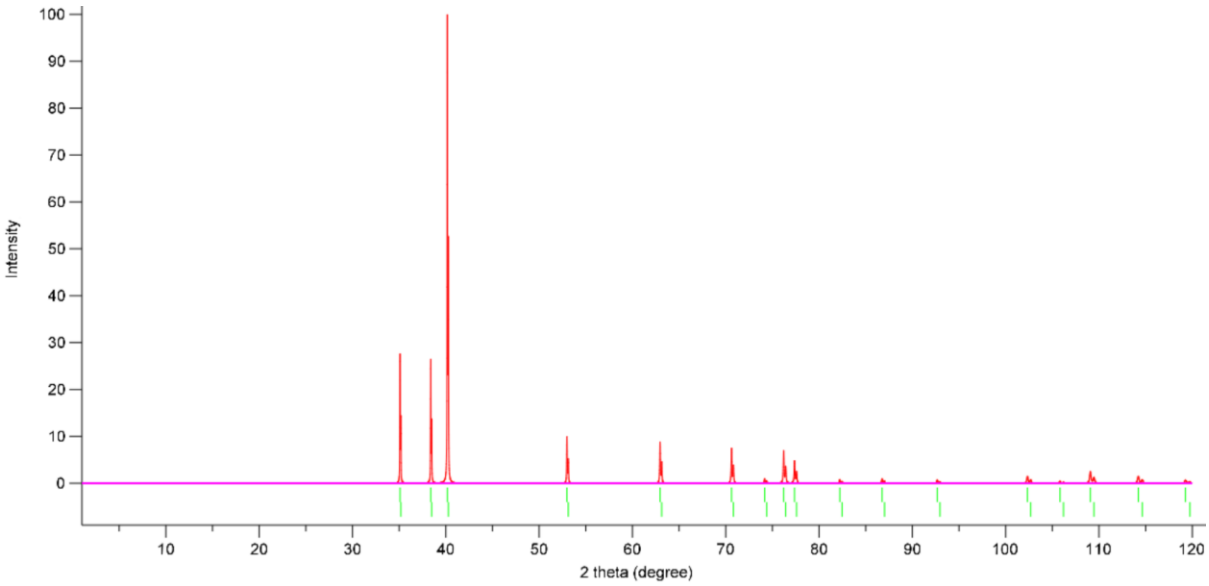

Figure B.1: XRD of the hexagonal Ti. All peaks match to COD9008517 in the Crystallographic Open Data Base (http://qiserver.ugr.es/cod)

Appendix C: Extraction of kinetic parameters

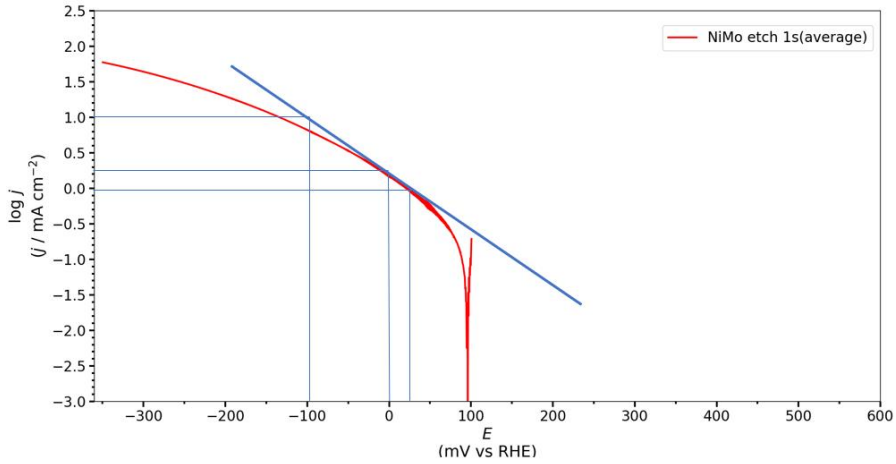

Figure C.1: The Tafel plot with Tafel slope lines for the averaged NiMo on Ti substrate etched at 1 s sample

The initial LSV curves were used to construct the Tafel plots by converting the current density' axis to a logarithmic scale from a linear scale. After the Tafel slope lines were drawn at Tafel region that extends from the onset potential (0.3 mA cm^{-2}) to at least 10 mA cm^{-2}. The next step was to determine the Tafel slopes by taking the actual slopes from the drawn lines. Since plots were done as log *j* vs *E*, then the negative reciprocal of the obtained slopes was found and reported as actual Tafel slopes. The exchange current densities were found by finding corresponding log j values for Tafel slope lines at *E* = 0 V and converting them to *j* values and adding «–» to indicate cathodic exchange current density. An example of these calculations for averaged NiMo on Ti substrate etched at 1 s sample is given below:

1) Take a slope of the Tafel slope line with values from the **Figure C.1** above:

$$\text{slope} = \frac{\log j_2 - \log j_1}{E_2 - E_1} = \frac{0-1\ \text{dec}}{26.5-(-97.1)\text{mV}} = -\frac{1}{123.6}\,dec\ mV^{-1}$$

2) Take a negative reciprocal of the found slope:

$$b = -\frac{1}{\left(-\frac{1}{123.6}dec\ mV^{-1}\right)} = 123.6\ mV\ dec^{-1}$$

3) Find interception of *E* =0 with the Tafel slope line and linearize the obtained value of *j*

At E = 0, log j = 0.26,then $j_0 = -10^{0.26} = -1.82$ mA cm^{-2}

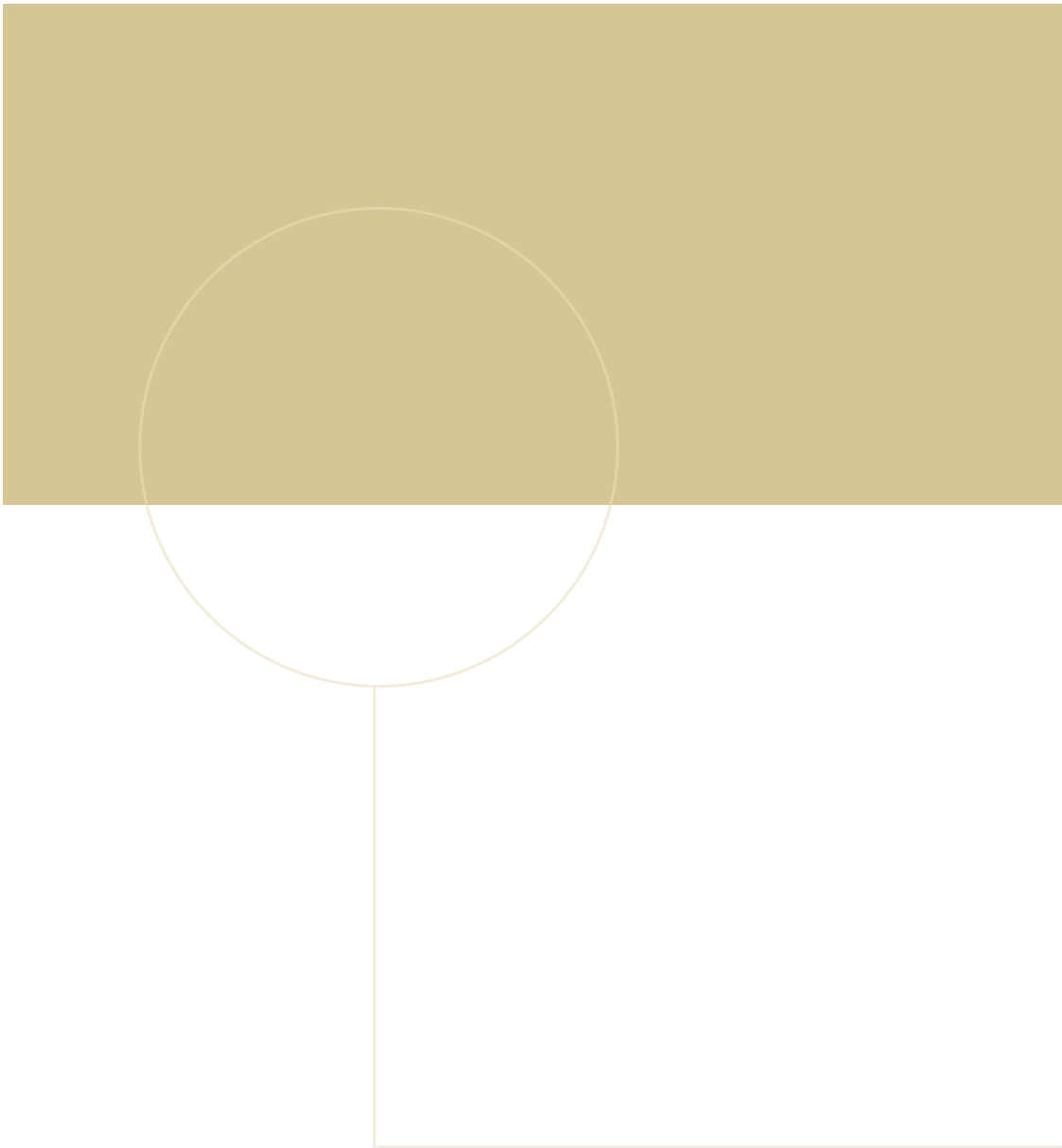

NTNU

Norwegian University of
Science and Technology